A new experimental setup for quantum computing and quantum simulation with individual ytterbium atoms in optical tweezers

Dissertation
zur Erlangung des Doktorgrades
an der Fakultät für Mathematik, Informatik und Naturwissenschaften
Fachbereich Physik
der Universität Hamburg

vorgelegt von

Tobias Petersen

Hamburg
2025

Gutachter/innen der Dissertation:	Prof. Dr. Klaus Sengstock Prof. Dr. Henning Moritz
Zusammensetzung der Prüfungskommission:	Prof. Dr. Klaus Sengstock Prof. Dr. Henning Moritz Prof. Dr. Michael Potthoff Prof. Dr. Ludwig Mathey Prof. Dr. Peter Schauß
Vorsitzende/r der Prüfungskommission:	Prof. Dr. Michael Potthoff
Datum der Disputation:	15.07.2025
Vorsitzender des Fach-Promotionsausschusses PHYSIK:	Prof. Dr. Wolfgang J. Parak
Leiter des Fachbereichs PHYSIK:	Prof. Dr. Markus Drescher
Dekan der Fakultät MIN:	Prof. Dr.-Ing. Norbert Ritter

Abstract

In this thesis, I describe a new experimental setup for trapping and imaging of single ytterbium atoms trapped in optical tweezers. The setup is aimed at future research in the field of quantum computing and simulation employing the alkaline-earth-like element ytterbium that offers advantages over commonly used alkali-atom species like rubidium that include the use of a highly coherent nuclear spin qubit for information encoding and access to a meta-stable clock state with employment in erasure conversion and mid-circuit measurement protocols. To exploit these advantages, a complex experimental setup is needed to implement the omg-architecture in neutral fermionic ^{171}Yb.

I describe the magnetic field setup capable of providing offset fields for quantum computing within the omg-architecture also capable of compensating stray magnetic fields to a sufficient degree, an external electrode setup used for compensation of background electric fields and the high-resolution imaging objectives used for trapping and imaging of single atoms.

Further, I present the detailed characterization of an optical setup featuring a pair of crossed acouto-optic deflectors operating at 532 nm used for the generation of a tweezer array with up to 144 sites. This setup facilitates the generation of tweezers with near-diffraction limited waist size of 600 nm radial and 5.3 µm axial with a homogeneity of both size and intensity of under 3 % over the whole array.

After giving an in-depth characterization of the magneto-optical trap used for loading atoms into the tweezers, I report on first experiments using this new experimental machine with single bosonic ^{174}Yb atoms paving the way for future studies. Stochastic loading of bosonic ^{174}Yb atoms into the array with an efficiency of near 60 % and imaging of the single atoms in the tweezers with a fidelity of 99.862 % and an imaging loss of 1.2 % is demonstrated. The atoms are shown to have a temperature of 31 µK through a release-and-recapture experiment and exhibit a lifetime of about 23 s when trapped in the tweezers.

After presenting the plans for a pulse generator setup including elliptical beam shaping for the driving of single qubit gates in the future, I conclude with an outlook on possible future research prospects.

Zusammenfassung

In dieser Arbeit wird ein neuer Experimentaufbau zum Fangen und Abbilden von einzelnen Ytterbium-Atomen gefangen in optischen Mikrofallen vorgestellt. Der Aufbau ist dabei für zukünftige Experimente zu Quantencomputing und Quantensimulation ausgelegt. Das Lanthanoid Ytterbium hat für diese Anwendungen Vorteile wie das Kodieren von Informationen in einem hochkohärenten Kernspin als Qubit und dem Zugang zu einem metastabilen Uhrenzustand, der in Protokollen für Fehlerkorrektur und Innerschaltkreismessungen Anwendung findet. Dies unterscheidet es von häufig genutzten Alkali-Elementen wie Rubidium. Um diese Vorteile nutzbar zu machen, wird ein komplexer Experimentaufbau beschrieben, der die sogenannte omg-Architektur für neutrale, fermionische ^{171}Yb-Atome implementiert.
Es werden die Magnetfeldspulen beschreiben, welche es erlauben die für die omg-Architektur nötigen Quantisierungsfelder zu erzeugen und Hintergrundfelder in ausreichender Genauigkeit zu kompensieren. Weiterhin wird das Layout der Optik, eine externe Elektrodenanordnung zum Ausgleichen von elektrischen Hintergrundfeldern und das hochauflösenden Mikroskopobjektiv, welches zum Fangen und Abbilden der einzelnen Atome genutzt wird, beschrieben.
Weiterhin beschreibt es die Charakterisierung eines optischen Aufbaus zum Erzeugen von Anordnungen von optischen Mikrofallen mit einer Wellenlänge von 532 nm mit Hilfe eines Paars gekreuzter akoustooptischer Deflektoren mit einer Größe von bis zu 144 Fallen. Der Aufbau ermöglicht die Erzeugung von beugungsbegrenzten optischen Mikrofallen mit einer Strahltaille von 600 nm radial und 5.3 µm axial und einer Homogenität von Intensität und Größe von unter 3 % über die gesamte Anordnung.
Nach einer detaillierten Charakterisierung der magneto-optischen Falle, welche zum Laden von einzelnen Atomen in die optischen Mikrofallen genutzt wird, wird das Laden von einzelnen bosonischen ^{174}Yb in die optischen Mikrofallen mit einer Effizienz von nahe 60 % sowie das Abbilden der einzelnen Atome mit einer Güte von 99.862 % und einem Verlust von 1.2 % der Atome pro Bild demonstriert. Die Temperatur der Atome wird mittels eines Wiedereinfangexperiments zu 31 µK bestimmt. Die Lebensdauer der Atome in den Fallen beträgt 23 s. Die gezeigten Experimente bereiten den Weg für weitere Versuche zu Quantencomputing und Quantensimulation mit neutralen Ytterbium-Atomen.
Nachdem die Pläne für einen optischen Pulsgenerator zum Treiben von Einzel-Qubit Gatteroperationen im zukünftigen Experiment beschrieben wurden, schließt die Arbeit mit einem Ausblick auf die möglichen Forschungsthemen für das Experiment ab.

Contents

1 Introduction

In 1975 it became clear by theoretical considerations by R. P. Poplavskii that it would be computational infeasible for classical computers to simulate quantum systems [1] because of superposition.
To solve this problem, computers needed to be upgraded by employing the principles of quantum mechanics and in 1980 Paul Benioff described the first quantum mechanical model of a computer [2] as a quantum Turing machine and further developed this idea in 1982 [3].
This idea of using quantum mechanics in computational science was further fueled by the introduction of the gate-based, universal quantum computing by Deutsch in 1985 [4].
These theoretical considerations became even more relevant when it was shown that not only the simulation of quantum systems was infeasible with classical computers but that also classical computational problems could gain an exponential speedup when solved by quantum algorithms. The first of these was the Deutsch–Jozsa algorithm proposed in 1992 [5] that showed that there are deterministic quantum algorithms which are exponentially faster than any deterministic classical algorithm.
This was soon resolved by the proposal of Shor's algorithm [6] for the factorization of prime numbers and Grover's algorithm [7] for unstructured search.
As these problems are very relevant to computational science, considerable effort was placed to find suitable physical systems to construct a quantum computer that would be able to show this quantum supremacy. To assess the feasibility of any given quantum machine to serve as a quantum computer, David P. DiVincenzo proposed the following five criteria in 1996 [8]:

- A scalable physical system with well-characterized qubits
- The ability to initialize the state of the qubits to a known state
- Long relevant coherence times
- A universal set of quantum gates
- A qubit-specific measurement capability

Possible candidates for the implementation of quantum computing include superconductors [9, 10, 11, 12, 13, 14, 15, 16], trapped ions [17, 18, 19], linear optical quantum computing [20, 21, 22], vacancy-centers in diamond [23, 24, 25] and neutral atoms [26].
One of the most promising platforms today fulfilling all of the five criteria is neutral atoms trapped in optical tweezers as they are an already well established quantum technology with an extensive toolbox for manipulation of quantum states [27].
Neutral atoms were proposed for quantum computing in the early 2000s [28], first with gate operations based on ultra-cold collisions of atoms [29, 30]. Soon after followed the proposal of gate operations based on Rydberg atoms, first the interaction gate [31] and later the blockade gate [32]. These theoretical developments closely followed the experimental advances in the

field of ultra-cold atoms. The proposed platform needed the ability to trap and manipulate single atoms in optical potentials, the most promising being the trapping of single atoms in diffraction limited laser spots called optical tweezers by the dipole force.
The first atom in an optical tweezer was realized in the year 2001 [33] and the first array of optical tweezers generated with micro lenses in the year 2002 [34].
The first observation of the Rydberg blockade was done in the year 2008 [35] and was closely followed by the first realization of two qubit entangling gates in 2010 [36, 37] in the form of the CNOT-gate. These groundbreaking experiments still only worked with two single traps and considerable experimental effort was placed into the ability of the experiments to be able to generated larger arrays of atoms.
This effort was fueled by the implementation of spatial light modulators for the generation of arbitrarily spaced tweezer arrays. Although first used as early as 2004 [38], it was not until 10 years later that spatial light modulator generated arrays were able to trap single atoms [39] in arrays with up to 100 sites.
A basic limitation of these systems is the fact that they rely on light assisted collisions to isolate single atoms [40, 41], leading to a fill fraction of all sites close to 50 %. Although this process can be engineered in a favorable way leading to near-deterministic loading [42], the generation of large scale defect-free arrays was not possible without the ability to move single atoms first realized in 2007 with a tilt-mirror [43] and the implementation of large scale atom sorting using acousto-optic deflectors in two dimensions [44, 45] and three dimensions [46]. These devices were first used in trapped ion experiments as early as 1999 [47] and later also introduced to the neutral atom platform [48].
Another essential ingredient was the realization of ground-state cooling of atoms in optical tweezers [49, 50], paving the way to high-fidelity gate operations.[1]
These first experiments worked with alkali atom species like rubidium and it was not until later that experiments started to trap the alkaline-earth metal atoms strontium [52, 53] and ytterbium [54]. Although experimentally more challenging, these atoms offer the prospect of higher achievable gate fidelity and offer a richer set of properties to be exploited in quantum applications [55]. [2]
Here, the fermionic isotope ^{171}Yb is an outstanding candidate as a basis for quantum computing when trapped in optical tweezers, as it well fulfills DiVincenzo's criteria when trapped in optical tweezers.
This isotope has a nuclear spin of 1/2 and thus offers a well defined two-level system sometimes even called *natures qubit*. As such, it fulfills DiVincenzo's first criterion of being a well characterized qubit and when trapped in optical tweezers offers high scalability as this platform is already able to trap several thousand atoms [57]. The scalabilty is further increased by the the fact that it is possible to find favorable parameters for enhanced loading allowing for high fill-fractions of the tweezer arrays [58]. One challenge in neutral atom quantum computing

[1] A good overview of the early developments can be found in [51].
[2] For a review of quantum computing with neutral atoms see for example [55] and for quantum simulation [56].

remains the leakage from the qubit subspace while performing entangling gates using the Rydberg blockade. This challenge can be mitigated in Ytterbium using erasure conversion schemes enabled by the unique level structure [59].
As the controllability of neutral atoms is already well established, this platform is also able to fulfill the second criterion and initialize the atoms in the array to a well known state [58, 60].
The coherence times of the qubits encoded in the nuclear spin of ^{171}Yb where shown to be on the order of seconds [58, 60], as the nuclear spin in the ground as well as the clock state is well decoupled from the environment and the connection between the two is a narrow intercombination line also used in state-of-the-art atomic clocks [61]. The coherence time of these states is orders of magnitude larger than the duration of typical gates, fulfilling DiVincenzo's third criterion. The availability of the unique combination of two nuclear spin qubits connected by an ultra-narrow clock transition has lead to the proposal of the so called omg-architecture for quantum computing with ^{171}Yb atoms [62].
DiVincenzo's fourth criterion has also been fulfilled for ^{171}Yb, as single and two qubit gates with high-fidelity have been experimentally demonstrated [58, 60, 63, 64].
The unique level structure of ytterbium also enables efficient measurements, which have been demonstrated by many groups [65, 66, 67, 68]. This also fulfills DiVincenzo's fifth criterion.
All this makes neutral fermionic ^{171}Yb trapped in optical tweezers a promising candidate for universal quantum computing and the platform has already been able to run first algorithms [69].
This thesis describes a novel experimental setup build in the group of Klaus Sengstock at the university of Hamburg. The setup is aimed at employing the unique omg-architecture of ^{171}Yb to perform experiments on quantum computing and simulation. It describes the optical and mechanical assemblies of the setup, shows first experiments on trapping and imaging of single ^{174}Yb atoms in optical tweezers generated with the aid of a pair of acousto-optic deflectors operated at the wavelength of 532 nm, characterizes the performance of the machine and gives an outlook on future research prospect of the experiment set up during this thesis.

Thesis outline

This thesis is structured as follows:

- Chapter 2 gives an overview of the tweezer platform in general and highlights the most important properties of Ytterbium and its advantages for Quantum Computing and briefly summarizes the relevant properties of Rydberg atoms.

- Chapter 3 describes the experimental setup built during the time of this thesis with the aim of performing quantum computing experiments employing the omg-scheme with ^{171}Yb. It describes the core of the machine including the optics layout, the control systems for magnetic and electric fields and the high-resolution microscope objectives used for trapping and imaging of single ytterbium atoms.

- Chapter 4 illustrates the setup and characterization of the optical setups used for generation of tweezer arrays and for imaging of the atoms. It presents the setups used for high-fidelity imaging of single atoms using fluorescence imaging and for generation of tweezer arrays with the aid of a pair of acousto-optic deflectors at the wavelength of 532 nm. Further it describes an analysis setup used for detailed characterization of the optical tweezers and gives an overview of the general optical shape of a tweezer generated with a microscope objective and closes with the analysis of the performance of the machine in generating tweezer arrays with a pair of acousto-optic deflectors.

- Chapter 5 This chapter illustrates the setup and characterization of the 3D-MOT performance. After describing the laser system and electronic control system used for generation of the light for the magneto-optical trap and showing the optical layout of the beams, it gives a detailed characterization of the loading and compression of the 3D-MOT used for efficient loading of atoms into the optical tweezers.

- Chapter 6 shows the performance of the experiment on imaging and trapping single ^{174}Yb atoms in 532 nm tweezers generated with an acousto-optic deflector as well as the experiments conducted to characterize the traps using single atoms. After giving a detailed explanation on the image processing required for identification of a single atom with high-fidelity, it characterizes the imaging performance of the machine. With the capability to convert experimental images into an occupation matrix with high fidelity, it shows first experiments on performing optimized parity projection, determining the temperature of the atoms in the trap, analyzes the lifetime of the atoms in the tweezers and shows the results of a trap modulation experiment to determine the trap frequencies.

- Chapter 7 describes the optical setups planned for addressing the transitions required to implement qubit-operations. It presents the planned setups for both π-polarization and σ-polarization to drive Raman transitions in the hyperfine manifold of the $^3P_0$ clock state, which in future will serve as the computational qubit in the omg-architecture. The beams will enable the driving of high-fidelity singe qubit gate operations in the future.

- Chapter 8 summarizes this thesis and gives an outlook on future research topics. The most promising first experiments include the experimental implementation of machine learning optimized CNOT-gates and the simulation of spin liquid states.

2 A tweezer platform for Yb atoms

This chapter describes the basic principles needed for the rest of this thesis. It gives an overview of the tweezer platform and describes its working principle, highlights the most important properties of Ytterbium and its advantages for Quantum Computing and briefly summarizes the relevant properties of Rydberg atoms.

2.1 An introduction to the tweezer platform

Recent technical developments have made the tweezer platform one of the most promising candidates for Quantum Computing and Quantum Simulation. A sketch can be found in figure 2.1.
As for every state of the art cold atom experiment, it relies on trapping neutral atoms in optical potentials through the dipole force inside a vacuum chamber. Like the previously developed Quantum Gas Microscope, this platform is able to image single atoms and gain full access to quantum mechanical correlation functions. It is also able to manipulate atoms one by one, being able to move and excite single atoms in an array.

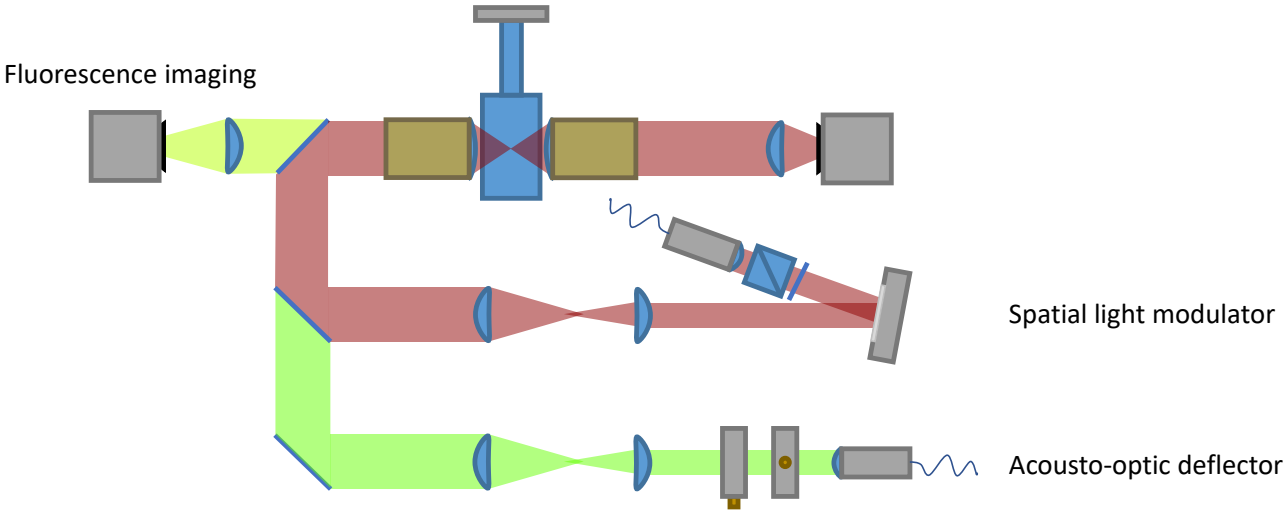

Figure 2.1: Schematic overview of the tweezer platform. Atoms are trapped in tight optical potentials called optical tweezers generated by either a spatial light modulator for static arrays or acousto-optic deflectors for movable tweezers. The tight focus of sub-wavelength size is generated using an imaging system with high numerical aperture like an aspheric lens or a microscope objective. The occupation of the array is read out using the fluorescence collected from the atoms.

Like the Quantum Gas Microscope, this platform relies on imaging atoms through collecting their florescence with a high-resolution imaging objective but also harnesses its optical powers to generate diffraction-limited dipole traps, so called optical tweezers. Their development as an experimental technique has relied on two main devices, spatial light modulators and acousto-optic deflectors.

These devices enable the generation of a few thousand of optical tweezers, a great enhancement compared to the first experiments with single atoms in optical tweezer, which were only able to generate few traps.
Spatial light modulators achieve this by imprinting a phase pattern on the laser beam, generating an arbitrary image of spots that is not confined to a regular arrangement in comparison to previously used optical lattices. Their disadvantage is their slow speed compared to the atomic time scales in the experiment. This is why they are commonly used to generate static arrays.
Acousto-optic deflectors do not offer the possibility to generate arrangements other than rectangular lattices[3], but offer the advantage of high switching speed. They thus can be used to move atoms or individually address them giving control on the single particle level.
Recent developments [70] have started to also integrate digital mirror devices because of their high switching speed and developed techniques for even greater control at the single particle level.

2.2 Atomic properties of Ytterbium

Ytterbium as an alkaline-earth like atomic species from the lanthanoid series features numerous of complex properties, for a summary see for example [**?**, 71]. The following chapter will focus on the optical properties and describe the possibilities for exciting and trapping Ytterbium atoms and highlight the advantages for quantum computing and simulation applications.

2.2.1 Relevant transitions

Ytterbium as a divalent, alkaline-earth-like atom features a significantly richer level structure than commonly used alkali atomic species. A level scheme with the most important transitions can be seen in figure 2.2. This richness in possible transitions opens the way to study more complex physical phenomena but at the cost of increased complexity of the experimental setup needed.
The most relevant transitions for the experiment described in this thesis starting with the shortest wavelength are:

301 nm

This transition connects the $^3P_0$ clock state to the $^3S_1$ Rydberg series as well as the $^3D_1$,$^3D_2$ and $^1D_2$ Rydberg series [64]. It will be used to generate entanglement and ultimately drive 2-Qubit gates in the meta-stable clock qubit manifold. The Rydberg manifold can be reached from the meta-stable clock state in a single-photon excitation opening the possibility for higher Rabi frequencies than commonly used two-photon excitation schemes [72].

[3] That is when used under a 90° angle. Other arrangements also offer the possibility for different geometries, but are still limited to coupled lines.

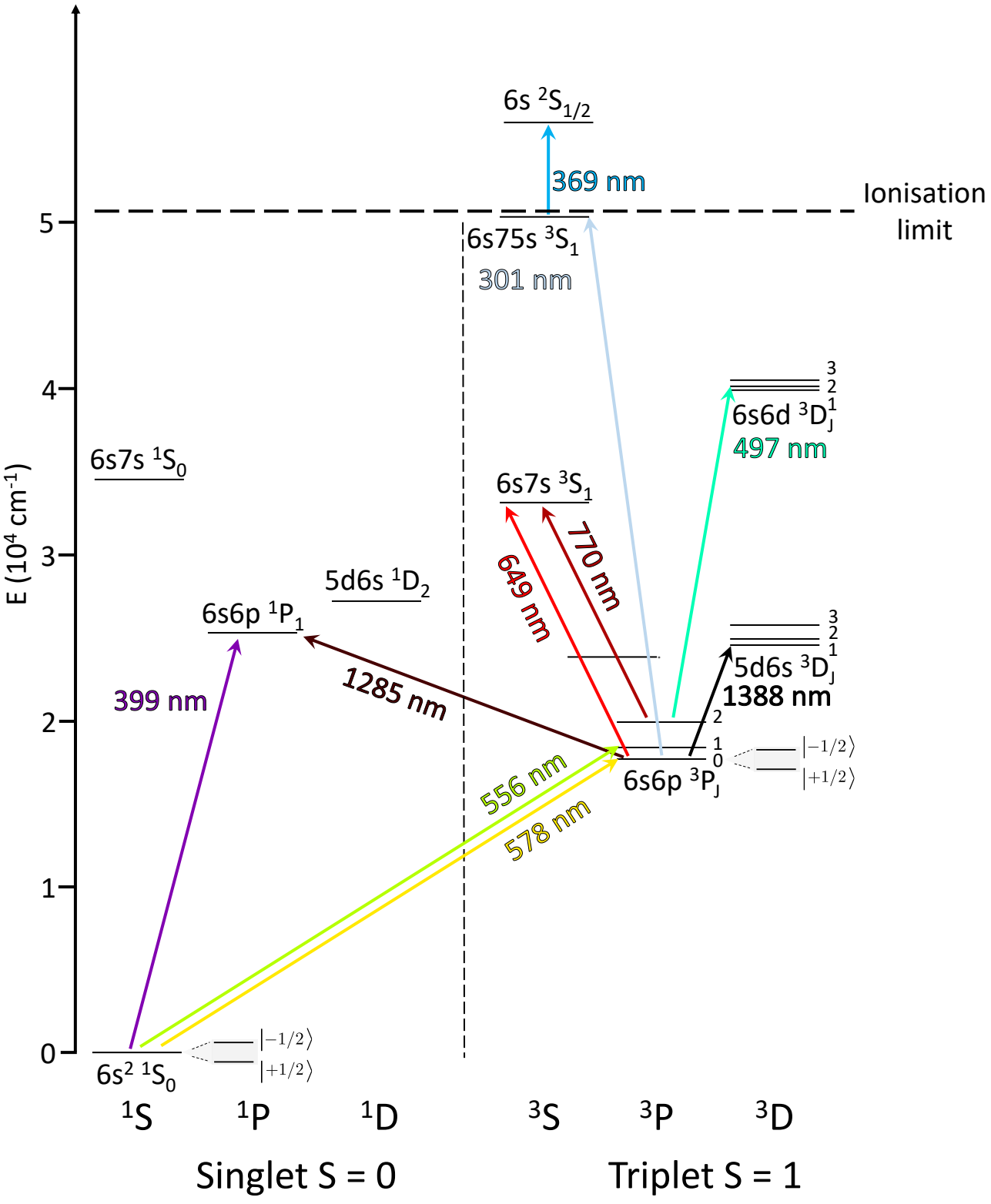

Figure 2.2: Level scheme of Ytterbium with the most relevant transitions. The ionization threshold is 50443.2 cm^{-1}.

369 nm

This transition is the primary transition in Yb^+ ions. When Rydberg atoms of neutral ytterbium are excited with this wavelength, it is possible to excite the remaining core to an auto-ionizing state thus removing any Rydberg atoms [73, 74]. With this it is possible to detect any Rydberg atoms through loss from the traps. It can also be used to optically detect Yb^+ ions for example for erasure conversion [59] and to apply local light shifts to atoms for local control over Rydberg excitations [73, 60].

399 nm

This broad transition from the $^1S_0$ ground state to the $^1P_1$excited state with a linewidth of 29 MHz is used as the first cooling transition as it lends itself for various setups as Zeeman slowers and 2D as well as 3D magneto-optical traps [75, 76]. It might also be used to image single atoms trapped in optical tweezers [54, 58].

497 nm

This transition connects the $^3P_2$ meta-stable state to the $(4f^{14}6s6d)^3D_2$ state. It will be used to repump the $^3P_2$ meta-stable state without leakage into the $^3P_0$ manifold used as the qubit subspace [68].

556 nm

The intercombination line from the $^1S_0$ ground state to the $^3P_1$ excited state with a line width of 182 kHz can be used for various cooling stages starting with a narrow line 3D magneto-optical trap [77, 76], gray molasses cooling [66], Raman sideband cooling [58] and EIT cooling [78]. It can also be used to drive single qubit gates in the groundstate manifold of fermionic isotopes [58].

578 nm

The intercombination line from the $^1S_0$ ground state to the $^3P_0$ excited state is one of the ultra-narrow clock transitions in ytterbium. Besides being used as the frequency standard in state of the art atomic clocks [79, 80], it offers the possibility to connect the ground state with the meta-stable qubit manifold [62].

649 nm

The transition from the $^3P_0$ clock state to the $^3S_1$ excited state can either be used to repump atoms from the clock state when tuned on resonance, but most importantly it can be used to drive Raman transitions in the hyperfine manifold of fermionic Ytterbium isotopes that can be engineered as single Qubit gates [62].

770 nm

The transition from the $^3P_2$ meta-stable state to the $^3S_1$ is used to repump atoms trapped in the meta-stable state, getting rid of unwanted population loss as atoms trapped in the $^3P_2$ are lost from the experiments especially because this state is anti-trapped in commonly used trapping wavelength that fulfill a magic condition for the clock transition.

1285 nm

A intercombination transition from the $^3P_0$ state to the $^1P_1$ state, it might also be used as a repumping wavelength [81].

1388 nm

The transition from the $^3P_0$ clock state to the $^3D_1$ excited state can be used in the same way as the transition to $^3S_1$ to repump the $^3P_0$ clock state population or drive Raman transitions [66]. Additionally it can be used to quench the clock transition for laser cooling [82, 83]. As this wavelength lies in the telecommunication window, it is also suited for the implementation of quantum networks [84, 85, 78].

1539 nm

This transition connects the $^3P_1$ state to the $^3D_1$. It can be used to populate the meta-stable $^3P_0$ clock state through optical pumping when combined with 556 nm light [68].

2.2.2 Trapping potentials

Besides exciting the atoms with resonant light, any modern neutral atom experiment needs to trap their atoms in some kind of light potential. Recently, new possible trapping wavelength were explored for Ytterbium besides the trapping wavelength commonly used in lattice experiments. The most prominent wavelength for a tweezer experiment with Ytterbium atoms are:

460 nm

This wavelength fulfills the magic trapping condition for the $^1S_0$ to $^3P_0$ clock transition [86]. It offers higher polarizability and smaller spot size leading to deep trapping potentials.

483 nm and 487 nm

These two wavelength are magic for the $^1S_0$ to $^3P_1$ transition in fermionic ^{171}Yb (483 nm for $^3P_1$,$m_F = \pm 3/2$ [65] and 487 nm for $^3P_1$,$m_F = \pm 1/2$[68]) and can be used for trapping and imaging of this isotope. As the combined energy of two trap photons and one imaging photon at 556 nm lies above the ionization threshold, this combination suffers from loss through this channel.

532 nm

This wavelength fulfills the magic trapping condition for the $^1S_0$ to $^3P_1$,$m_F = 0$ transition in bosonic ^{174}Yb and is thus favorable for trapping and imaging of this isotope. As the atoms have a high polarizability at this wavelength, it might also be used to sort atoms or apply light shifts locally in the fermionic isotopes. When used for imaging of bosonic Ytterbium, this combination suffers from ionizing as well.

759 nm

This is the commonly used wavelength for magic trapping of the $^3P_0$ clock state. It can be tuned to fulfill a triple magic condition for the $^3P_1$,$m_F = \pm 1/2$ in ^{171}Yb as well using a magic polarization angle to tune the vector and tensor light shift in the correct way.[4] Besides that, this wavelength is below the ionization threshold for three photon ionization processes, closing this loss channel. Thus, this wavelength offers the possibility for high fidelity imaging and clock excitation for fermionic ^{171}Yb. The disadvantage of this wavelength is the comparably low polarizability and large spot size when focused to an optical tweezer leading to shallower trapping potentials.

2.2.3 Advantages for Quantum Computing and Simulation

Ytterbium offers severe advantages over commonly used alkali atom species and also the alkaline-earth metal atom Strontium making it the most promising candidate for Quantum Computing with neutral atoms in tweezer arrays.

Nuclear spin Qubit

One of the most striking advantages is the qubit encoding in the spin states of fermionic ^{171}Yb. This atomic species has a nuclear spin of 1/2, making it the perfect 'natural' qubit. This renders it superior to fermionic Strontium with a nuclear spin of 9/2, where technical tricks need to be played to isolate two spin states from the hyperfine manifold [87]. As both the $^1S_0$ ground state and the $^3P_0$ meta-stable state have a total angular momentum of J=0, both Qubit manifolds are also less sensitive to decoherence as the nuclear spin is almost decoupled from the electronic degree of freedom [88].

Clock transition

The access to a doubly forbidden clock transition opens the possibility to have two Qubit manifolds in one atomic species and thus the possibility to have data and ancilla Qubits with different driving wavelength in one atomic species when using fermionic ^{171}Yb. Also,the meta-stable Qubit manifold lies energetically high enough to allow for transition to the Rydberg state with

[4] This trick can also be used for triple magic trapping of bosonic ^{174}Yb [86].

one photon in the UV range leading to higher possible Rabi frequencies compared to two photon transitions used in alkali atoms [72].
As for bosonic ^{174}Yb, a Qubit encoded in the ground and meta-stable state benefits from the coherence properties of this transition.

Optical Rydberg state trapping

When excited to a Rydberg state, the second valence electron in Ytterbium is still optically active and the remaining core can still be trapped optically as it has an optical polarizability which can counteract and even surpass the repulsive Ponderomotive force acting on the Rydberg atom and can thus be optically trapped [89]. This might offer the prospect of increased gate-fidelity in the future. It might also be possible to achieve triple magic trapping of ground, clock and Rydberg atoms, mitigating the effects of motional decoherence [90].

Near-deterministic loading

The line width of the $^1S_0$ to $^3P_1$ transition of 184 kHz offers a favorable regime to engineer the molecular dynamics in the optical tweezers when parity projection is performed. By carefull selection of the detuning, magnetic field strength and trap depth, a blue-shielding effect can be employed to excited two atoms to a molecular potential with binding energy small enough to only let one atom escape from the trap. As such, it is possible to achieve a loading probability larger than 50 % and easing the overhead on sorting to achieve fully loaded tweezer arrays [58].

Optical detection and manipulation of Rydberg states

As with optical trapping of the Rydberg atoms, the optically active core of the Rydberg state allows for optical manipulation. This opens the possibility to ionize the atom through excitation of the core electron leading to auto-ionization of this state and loss from the trap [72, 73]. The optically active core can also be used to apply light shifts to the Rydberg state to suppress the excitation of the atoms. Applying the light shift to the Rydberg state instead of the ground or clock state has been shown to lead to a lower scattering error. [73] This feature might be used for local control over the Rydberg excitation in an array, as the corresponding wavelength in Ytterbium of 369 nm is technically less challenging to implement than control via local Rydberg excitation at 301 nm.[5]

[5] Besides the fact that manufacturing objectives with large numerical aperture for UV wavelength is challenging because of the limited amount of available glasses with high transparency, as of the time of writing this thesis devices for local control are either unavailable like spatial light modulators (starting at 365 nm) or suffer from reduced specifications like acouto-optic deflectors (the scanning angle being a factor of 10 smaller for 301 nm than 369 nm) for the wavelength of 301 nm.

Error detection schemata

As the computational subspace within the atom can be chosen to be the meta-stable Qubit manifold, it is possible to consciously monitor leakage from the computational subspace into the ground state and monitor this population without disturbing the the computational subspace [59, 68]. The same holds for detection of unwanted Rydberg state population, when these atoms are optically ionized and the ion population is monitored. In this way a lot of errors can be converted to erasures paving the way to more resource friendly quantum computing.

Mid-circuit operations

As the ground and meta-stable Qubit sub-spaces are well separated energetically and coherent transfer between the two can be achieved using the clock transition, it is possible to selectively transfer and read-out population between the two sub-spaces and perform mid-circuit measurements in the ground-state manifold without disturbing the data stored in the meta-stable state [65, 66].

2.2.4 OMG-architecture

All the advantages discussed in section 2.2.3 lead to the construction of the so called omg-architecture, a qubit encoding first proposed for alkali-earth ions [91] and later adopted for neutral Ytterbium atoms [62, 92]. The proposed scheme is shown in figure 2.3 and consist of a meta-stable and a ground state qubit connected by an optical qubit. The interested reader will find more information in reference [62, 92].

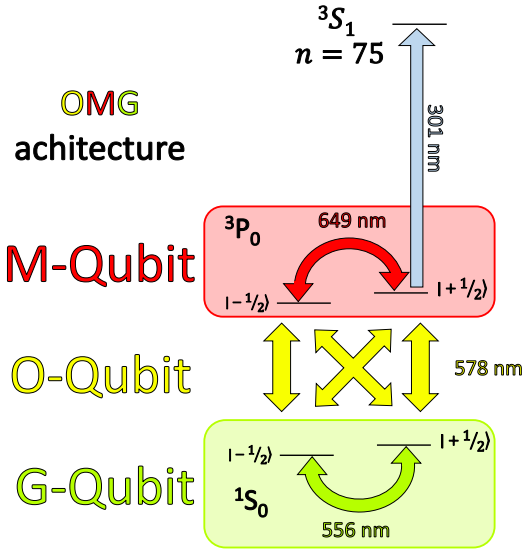

Figure 2.3: Overview of the omg-architecture in ^{171}Yb. A ground state qubit encoded in the nuclear spin of the $^1S_0$ ground state is connected to a meta-stable qubit encoded in the nuclear spin of the $^3P_0$ clock state via an optical qubit driven by the clock transition. Single qubit gates can be driven by Raman transitions in both qubit manifolds and two qubit gates can be implemented in the meta-stable qubit manifold via single photon Rydberg excitation.

2.3 Overview of Rydberg atoms

As a key ingredient for experiments on the tweezer platform, this section will briefly discuss the most important properties of Rydberg atoms for this thesis as they are used to generate interaction in tweezer arrays. For a more detailed description see for example [93].
The Rydberg atom is an atom in a highly excited electronic state with large quantum number n. Its striking properties result from this high excitation and they scale strongly with the principle quantum number. The easiest states to describe are the states in Hydrogen and heavier atoms like Ytterbium will need a more sophisticated description due to interaction between the Rydberg electron and the remaining core. This formalism is the quantum defect theory, which will put all interaction effects into a quantum defect δ and introduces a correction to the scaling with the principle quantum number as $n^* = n - \delta(n,1)$. This quantum defect will vary depending on the exact state used.

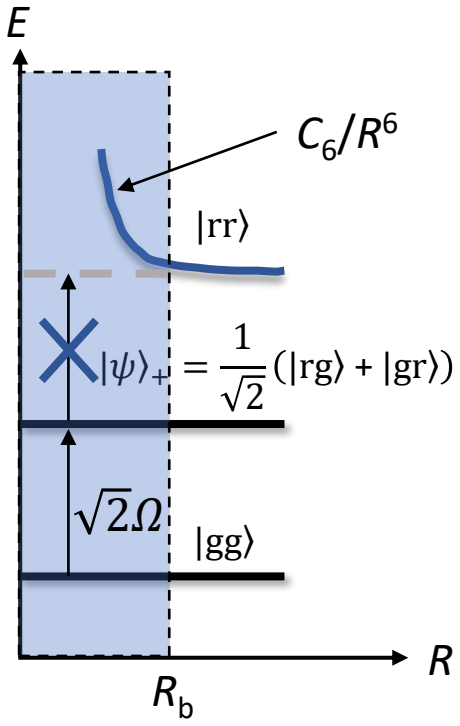

Figure 2.4: Schematic overview of the Rydberg blockade regime. For two atoms spaced closer together than the blockade radius R_b, excitation to the doubly excited state $|rr\rangle$is shifted out of resonance by the van-der-Waals interaction. The pair of atoms is excited to the entangled state $|\psi\rangle_+$ with a Rabi frequency enhanced by a factor of $\sqrt{2}$.

To now generate interaction in tweezer arrays, the most important feature between Rydberg atoms is the strong van der Waals interaction between two atoms in the Rydberg state

$$V_{\text{van der Waals}} = \frac{C_6}{r^6} \sim n^{*11} \tag{2.1}$$

which can be used to generate entanglement between two atoms or more atoms separated by as far as a few µm. This is due to the so called Rydberg blockade shown schematically in figure

2.4 where the strong scaling of the van der Waals interaction will lead to an energy shift of the doubly excited state where both atoms are in the Rydberg state. For a distance smaller than the so called Blockade radius, the atoms will be excited to the entangled state where both atoms share a Rydberg excitation. This can be used to either generate entanglement for the simulation of quantum many body states or drive two qubit gates.
For gate operations, the other important property is the the life time of the Rydberg state, dictating the parameters for gate times and needed Rabi frequencies to implement high-fidelity gate operations. The life time scales as

$$\tau \sim n^{*3} \tag{2.2}$$

In the special case of circular Rydberg states[6], the reduction in possible decay path ways leads to a scaling of

$$\tau \sim n^{*5} \tag{2.3}$$

The other important property is the sensitivity to electric fields, the DC Stark shift of Rydberg atoms scaling as

$$V_{\mathrm{DC}} \sim n^{*7} \tag{2.4}$$

This sensitivity imposes the challenge of precisely controlling the electric field back ground inside the machine and leads to the design and implementation of an electric field control system presented in section 3.4.

[6]Circular Rydberg states being states with maximum angular quantum number $l = n$.

3 Experimental apparatus

This chapter describes the experimental setup built during the time of this thesis with the aim of performing quantum computing experiments employing the omg-scheme with ^{171}Yb. It describes the core of the machine including the optics layout, the control systems for magnetic and electric fields and the high-resolution microscope objectives used for trapping and imaging of single ytterbium atoms. The setup was designed by N. Pintul and the author in close contact with C. Becker, the designs were discussed by the whole team. Calculations which are the foundation for the magnetic field coil setup were done by N. Pintul [94], the design of the main coils was done by the author based on previous work by S. Dörscher und A. Thobe [95, 96]. The compensation coils design was done by the author with help from D. Barlösius. Both sets of coils were build by D. Barlösius, tested by the author and implemented at the experiment by N. Pintul, A. Ilin, K. Sponselee and the author. The objectives and electrodes were implemented into the experiment by N. Pintul and the author. The objectives were tested by J. Deppe under supervision of the author, see [97]. The electrode design and simulations were done by the author as well as the FEA simulations for the glass cell and the ZEMAX analysis of the objective. All work was performed under the supervision of C. Becker and K. Sengstock.

3.1 Central optics setup

To be able to address all required transitions in Ytterbium, a complex layout of optics is need.

Breadboards

To have enough space for all optical systems, the experiment features three layers of optics as shown in figure 3.1.

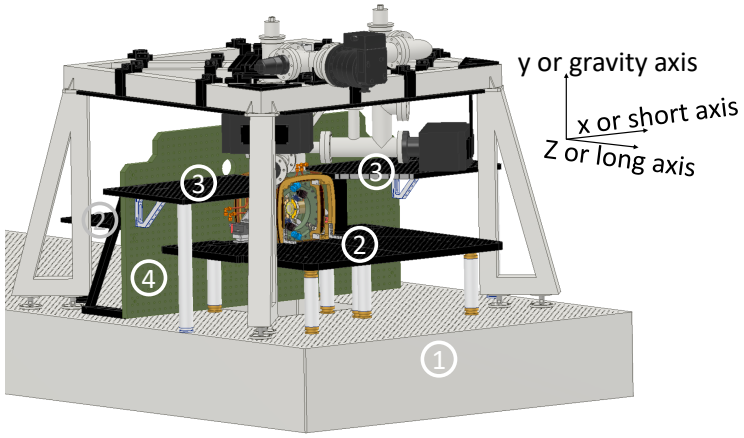

Figure 3.1: Main layers of the experiment. The optics for the numerous setups to trap and manipulate single atoms are arranged on three layers, the optical table (1) used for beams shone in through the objectives, two horizontal breadboards (2) supplying beams on the long axis (LA) and two upper horizontal breadboards (3) supplying beams on the two diagonal axis (DIA). A vertical breadboard (4) is only used as a support structure in the current setup. Coordinate axis shown with the naming convention for clarity.

The setup allows to shine in light on four main beam path, the long axis co-propagating with the main quantization field direction for light with sigma polarization, two diagonal axis perpendicular to the main quantization axis for light in pi configuration and the axis of the objectives for all light that shall be applied to the atoms as a diffraction limited spot.

Central experiment core

The central core of the experiment can be seen in figure 3.2. Placed around the glass cell is the main coil pair used to generate a homogeneous magnetic field of up to 500 G. The coils are placed so far apart to allow the high-resolution objectives to be placed on the small faces of the glass cell. Fixed to the objective holders are four segment-electrodes used to generate electric fields. The electrodes also feature one high-power UV-LED each for the reduction of surface charges on the glass. There are further four UV-LEDs placed on clip-on holders on the main coils. The outer part of the core consists of the compensation coil cage. See the upcoming chapters for more details on each of the subsystems.

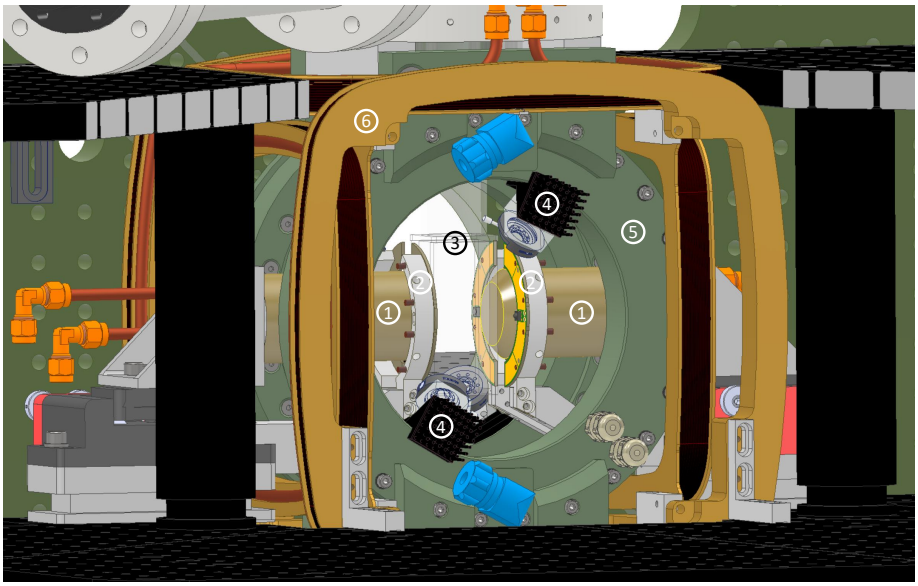

Figure 3.2: The main experiment core with (1) two high-resolution objectives, (2) four four-segment electrodes, (3) the glass cell, (4) high-power UV-LEDs, (5) the main coils and (6) the compensation coil cage.

Beam layout

To overlap all required laser beams, a complex stack of custom dichroic mirrors is employed on each of the axis. Figure 3.3 shows the layout on the horizontal breadboards for all light in sigma configuration.

On the front horizontal breadboard, the first dichroic mirror picks off the 301 nm light used for Rydberg excitation to be supplied to a beam stabilization system. The next dichroic mirror is a long-pass overlapping all visible wavelength with 1388 nm and 1285 nm used for repumping atoms form the $^3P_0$ meta-stable state. The next dichroic mirror separates 578 nm light used for

excitation to the $^3P_0$ meta-stable state from the 556 nm light used for magneto-optical trapping and Raman sideband cooling as well as 399 nm light used for imaging of the magneto-optical trap. Both wavelength might also be used for fluorescence imaging of single atoms trapped in tweezers. The two wavelength are split by the last dirchroic mirror.
The setup on the back horizontal breadboard features a longpass dichroic mirror as first element used to overlap the 301 nm light used for Rydberg excitation with all other visible wavelength. The next dichroic mirror separates 649 nm and 770 nm from all other wavelength. These two are split on another dichroic mirror, the 770 nm light being used to repump atoms trapped in the $^3P_2$ meta-stable state and the 649 nm light to drive Raman transitions in the $^3P_0$ meta-stable state together with a second beam propagating along one of the diagonal axes. On the reflected beam path, the next mirror separates the 578 nm light shone in from the front to supply it to a beam stabilization system from the 556 nm and 399 nm light.

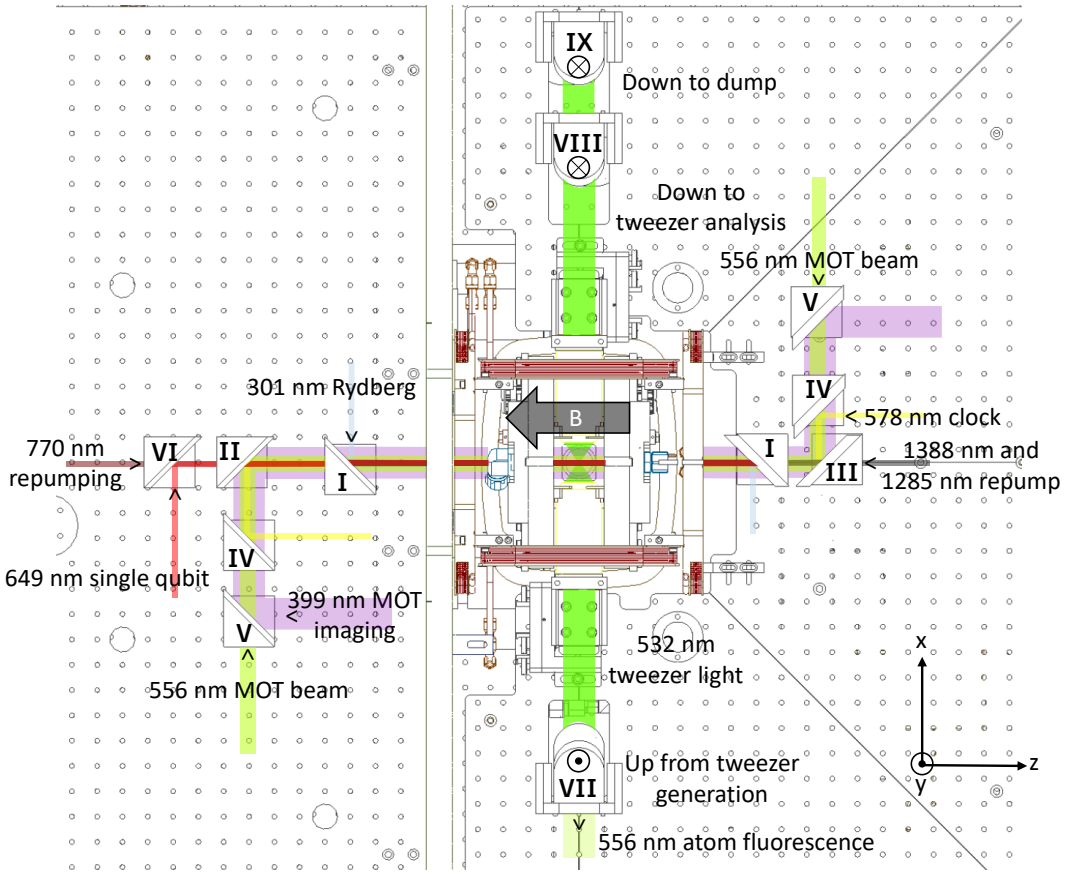

Figure 3.3: The beam layout on the horizontal breadboards around the main experiment. For more details see main text. Also indicated is the main quantization axis generated by the main coils.

The beam layout on the upper horizontal breadboards is shown in figure 3.4. The beams from the upper boards are passed between the compensation coils and the vacuum chamber and propagate with an angle of 57 ° to the horizontal plane. The beams from the upper boards form the two so called diagonal beams. The beams propagate perpendicular to the main quantization axis and supply light with pi polarization or tilted linear polarization.

The first dichroic mirror on the left board separates the two infrared wavelength 1388 nm and 1539 nm from the visible wavelengths, the first being used for repumping of the $^3P_0$ state and the second to populate this state through a two-photon process from $^3P_1$. The next dichroic mirror separates out 649 nm used to drive Raman transitions in the $^3P_0$ meta-stable state. The last mirror separates the 556 nm used for the magneto-optical trap from 399 nm light used for fluorescence imaging. The 399 nm imaging beam has a counter-propagating beam from below to balance the light force on the atoms.

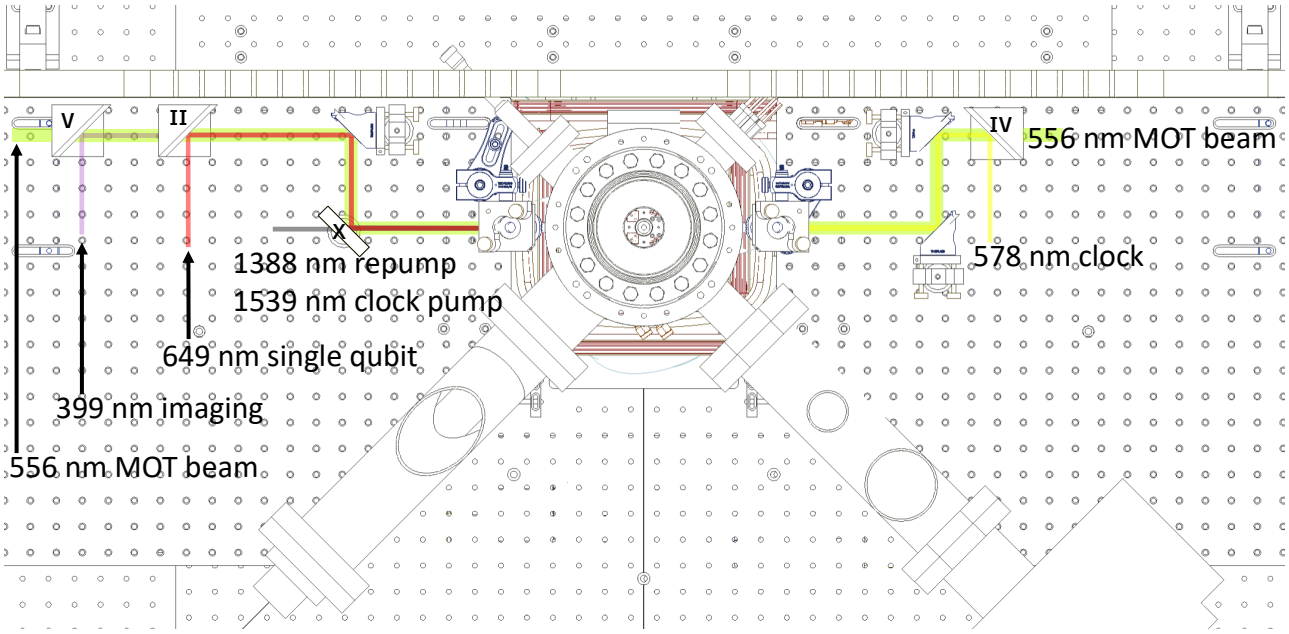

Figure 3.4: The beam layout on the upper horizontal breadboards.

A summery of all dichroic mirrors can be found in table 1.

Number	Reflecting	Transmitting	Comments
I	301 nm	399 nm, 556 nm, 578 nm, 649 nm, 770 nm, 1285 nm, 1388 nm	
II	399 nm, 556 nm, 578 nm	649 nm, 770 nm	
III	399 nm, 556 nm, 578 nm	1285 nm, 1388 nm	
IV	578 nm	399 nm, 556 nm	
V	399 nm	556 nm	
VI	649 nm	770 nm	
VII	532 nm, 759 nm	399 nm, 556 nm	12 mm thick substrate, stress compensated
VIII	4 % from 301 nm to 800 nm	Rest	Beam sampler
IX			Silver mirror
X	420 nm to 900 nm	990 nm to 1600 nm	Thorlabs DMLP950

Table 1: Summery of the properties of the optic elements in figures 3.3 and 3.4.

3.2 Science glass cell

The core of the experiment is the ultra-high vacuum glass cell in which the atoms are trapped in the tweezer array. The glass cell is made from fused silica[7] with excellent transmission from the UV to IR range and is coated with a broadband anti-reflection coating from 400 nm to 800 nm. The cell is made from a cuvette measuring 26 mm by 36 mm by 80 mm on the outside connected to a flange with a molybdenum quartz seal [8] for a total length of 180 mm. The walls of the cell are 3 mm thick, thin compared to cells used by other groups. The opening angle of the small faces allows for imaging with a numerical aperture of 0.5.

Simulation of bending under vacuum

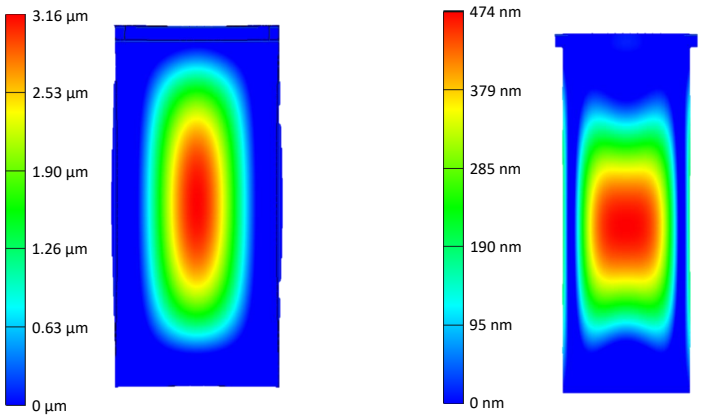

Figure 3.5: FEA simulation of the glass cell when under vacuum. (a) shows the bending of the large faces, (b) the bending of the small faces.

As the walls of the glass cell are only 3 mm thick, it is necessary to gain inside into its behavior under vacuum. The bending of the cell walls will lead to unwanted aberrations when imaging through it with the high-resolution imaging objectives leading to a loss in performance for both the fluorescence imaging of the atoms as well as the smallest achievable waist for the tweezers. Thus the magnitude of the wavefront error induced by the bending needs to smaller than 7 % rms of the wavelength used for imaging.[9] Because of the aspect ratio of the cell walls, the bending will act like a cylindrical lens and simple refocusing of the objective will not reduce the aberration effects.

[7] Heraeus SPECTROSIL 2000

[8] Seal made by Bomco. The cell was assembled by Hellma. The author notes that moly quartz seals are not available anymore and Hellma does not manufacture vacuum glass cells currently.

[9] This criterion is the equivalent of measuring the performance of an imaging system using the Strehl ratio and defining that the system performs diffraction limited down to a Streh ratio of 0.8. So a Streh ratio of 0.8 corresponds to a wavefront error of 7 % rms of λ.

A simulation of the bending can be seen in figure 3.5. It shows that the large faces of the cell bend over 3.16 µm under vacuum, large compared to all used wavelength. The small faces only show a bending of about 475 nm, on the order of the wavelength needed for the experiment.
These results were a major argument to design the machine in the way presented in this thesis, as in the early planning phase it was not clear whether one should image through the large or small faces of the glass cell.

Wavefront analysis

To further support the simulation described in the previous chapter, a wavefront analysis of the evacuated glass cell was performed using a Shack-Hartman sensor when the experiment was setup. The results can be seen in figure 3.6. The large faces of the glass cell were illuminated to their full extend of 30 mm with a 532 nm beam and show a large rms wavefront error of 24.7 % λ, the main aberrations being spherical and astigmatism.
The small faces were illuminated with beam of 20 mm of 532 nm light, illuminating the whole aperture of the glass cell. The small faces of the cell show excellent imaging performance with a rms wavefront error of below 1 % λ, perfectly fitting for high-resolution imaging.

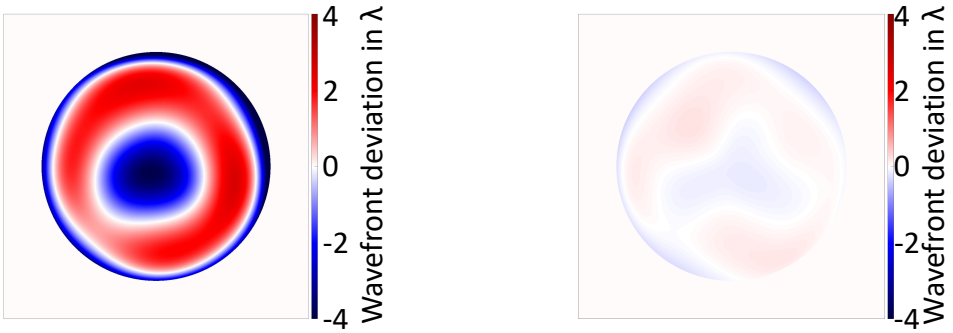

(a) **(b)**

Figure 3.6: The wavefront of a beam passing (a) through the large face and (b) through the small face of the glass cell. The beam sampled the whole available aperture on both sides. (a) has a peak-valley wave front deviation of 1.073 waves and a rms wave front error of 0.247 waves. (b) has a peak-valley wave front deviation of 0.049 waves and a rms wave front error of 0.009 waves.

Magic glass cell

In the simulations of the glass cell bending, it became clear that the large faces induce enough stress when bending inwards to bend the small faces outwards. This effect can be used to further reduce the bending of the small faces when an aspect ratio of the cell is chosen correctly. This aspect ratio will be called magic. A simulation of the bending of a magic glass cell can be seen in figure 3.7. For a cell made from fused silica with 3 mm thick walls, the magic aspect ratio

minimizing bending is achieved for cell of dimensions 31 mm x 26 mm. The residual bending over the area where the objective would image through is on the order of 60 nm, almost one magnitude smaller than the bending of the original glass cell.
A new glass cell with this magic aspect ratio and a anti-reflection coating optimized for the experiment was assembled[10] during this thesis, but is currently not used in the experiment.

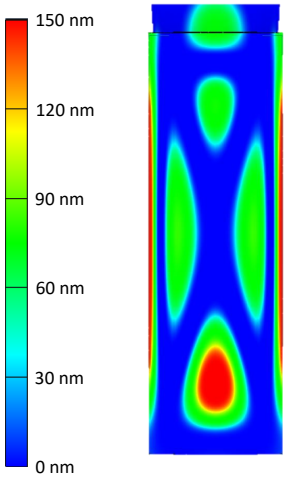

Figure 3.7: FEA simulation of a glass cell with magic aspect ratio. The bending of the small side is reduced to about 60 nm over the aperture of the objective.

3.3 Magnetic field coils

The magnetic field coil setup at the experiment is divided into two part, the main coils and the compensation coils, which are described in the following sections.

3.3.1 Main coils

A pair of so called main coils in Helmholtz configuration is used to generate the gradient field for cooling and trapping atoms in a magneto-optical trap and to generate high fields up to 500 G to serve as the quantization axis. This pair of coils is connected to a bank of IGBTs configured as an H-bridge to switch the fields from Anti-Helmholtz to Helmholtz configuration during one experiment run.
The mechanical design of the coils is optimized to generate a field as homogeneous as possible, for detail on the calculations for optimization see [94].
The field of a coil pair on axis at a current I is described by the formula

$$B(z) = \frac{\mu N I}{2}\left(\frac{r_1^2}{(r_1^2+(d/2-z)^2)^{3/2}} + \frac{r_2^2}{(r_2^2+(d/2-z)^2)^{3/2}}\right) \tag{3.1}$$

[10] The cuvette was manifactured by JapanCells from Ohara SK-1300 and attached to an old molybdenum quartz transition by Precision Glass Blowing.

where each coil has N turns and both coils are separated by the distance d. In this formula the radius of both coils does not need to be the same, allowing for slight variations due to tolerances in manufacturing.
The field in the plane between both coil pairs is empirically described by a polynomial of 4-th order in the following analysis, as the real functional form is hard to evaluate.

Mechanical design

The design of the main coils can be seen in figure 3.8

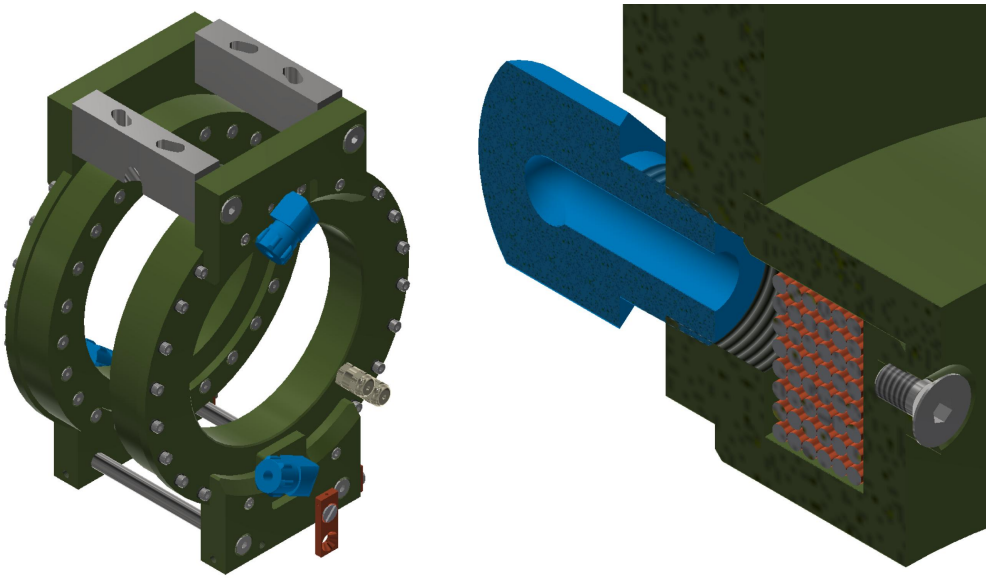

(a) (b)

Figure 3.8: The main coils used for generation of the magnetic field gradient for the magneto-optical trap and the magnetic field for the main quantization axis. (a) shows the complete coil pair, (b) is a cut through the housing showing the wire package inside the housing completely surrounded by water.

To be able to generate fields of up to 500 G, an efficient thermal management needs to be implemented for the Main Coils. The design is based on earlier ones in the group and consists of a wire package of double insulated copper wire of 2.1 mm diameter. The wire package of 8 x 6 wires is suspended in a housing of glass fiber reinforced plastic[11] with spacers and thus is almost completely surrounded by water. To make sure each loop of wire is cooled efficiently, the wire package is kept at a distance from the housing using spacers made from plastic and each layer of wire is kept at a distance from the previous one with plastic spacers as well.
The current limit of the design is given by the connections of the cables to the wire, which are not efficiently cooled.
To monitor the temperature of the coils and protect them from overheating, thermistors are installed on the cable connectors and at the water outlet as well as a bi-metal switch at the

[11] EP GC 201

water outlet to trigger an Interlock system switching off the current when the temperature of the housing exceeds 50 °C.

Measurements of fields and parameters

An example measurement of the magnetic field generated by the coil pair done with a 3D Hall sensor is given in figure 3.9.

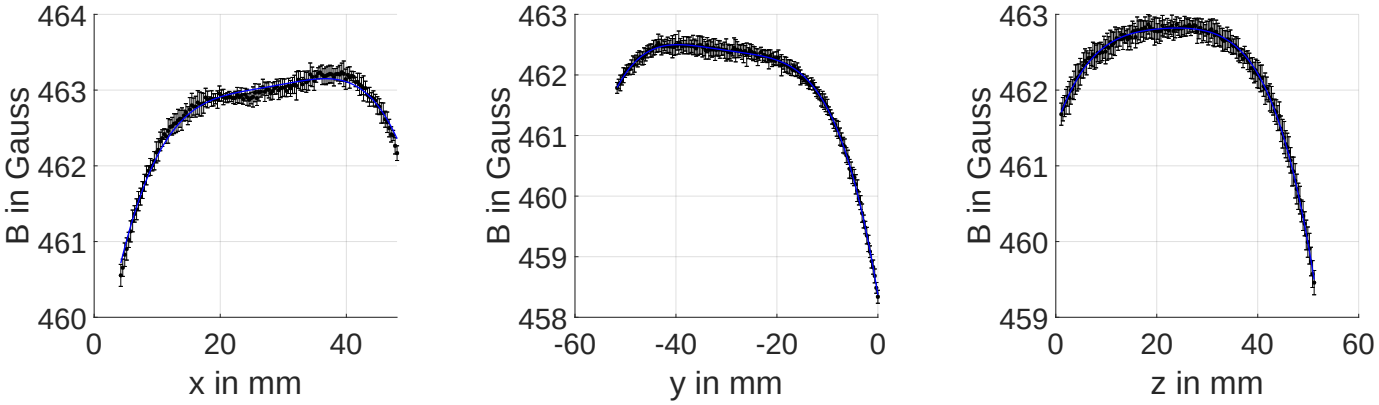

(a) Magnetic field along the long axis. **(b)** Magnetic field along the gravity axis. **(c)** Magnetic field along the short axis.

Figure 3.9: The magnetic field of the main coils in Helmholtz configuration measured at an input current of 90 A. The x direction is the coil axis, the y direction is the gravity axis and the z direction is the horizontal axis. The line plot in sub figure (a) is the field along the coil axis and is fit with equation 3.1, the other two directions (b, c) are fit with a polynomial of 4-th order. The deviations of the form of the field from a perfect Helmholtz configuration are well explained by manufacturing tolerances in the radius of the coils of about 500 µm as well as stray fields from the cables supplying the current to the coils.

The calibration of the field strength is given in figure 3.10. As visible in sub-figure (b), the deviation from a perfectly linear behavior is negligible indicating that the cooling is working and no parts of the coils are expanding thus changing the field.
The main properties of the coils are summarized in 2.

$I_{\text{max,constant}}$	90 A
B_{AHH}	0.703(4) G/(cm A)
B_{HH}	5.142(2) G/A
$B_{\text{HH}}^{\text{Inhomogeneity}}$	$\begin{pmatrix} 33(100) \\ 27(100) \\ 0.1(100) \end{pmatrix}$ µG/A
$B_{\text{HH}}^{\text{Residual Gradient}}$	$\begin{pmatrix} 2.2(2) \\ 0.8(1) \\ 0.01(20) \end{pmatrix}$ mG/(cm A)

Table 2: The parameters of the main coils. The inhomogeneity is given over a 200 µm area in the middle of the field. The measurements were conducted with a water flow of 250 L/h.

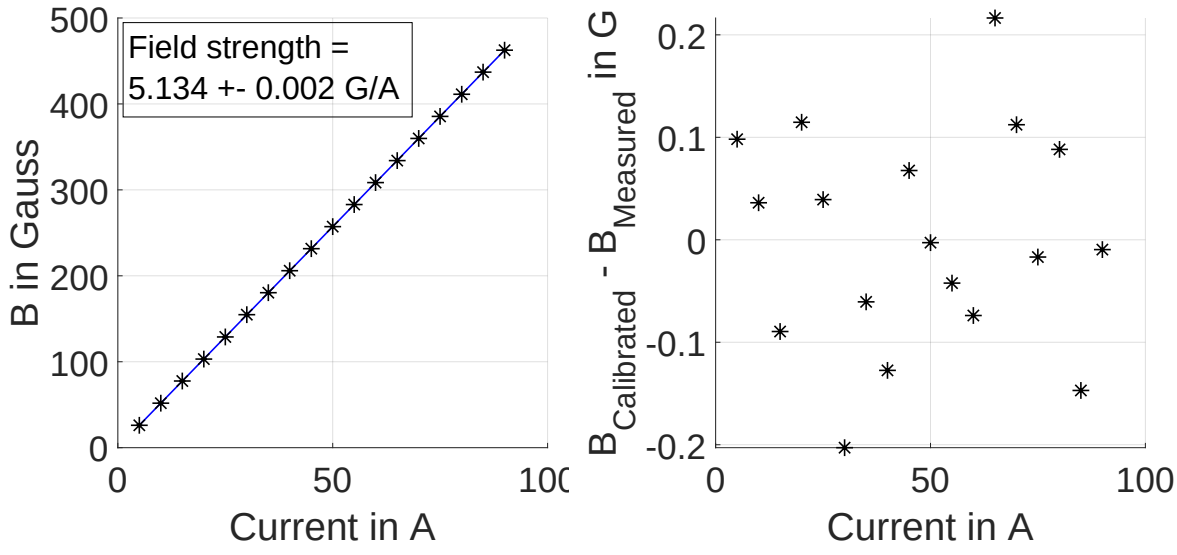

(a) **(b)**

Figure 3.10: (a) Magnetic field strength generated by the main coils in Helmholtz configuration for different currents. The behavior is linear as also indicated by the residuals in (b) showing no effect of heating over the scanned current range.

For a target magnetic field of 200 G, the inhomogeneity over an array of 200 µm side length is about 1.3 mG and the residual gradient 90 mG/cm.

3.3.2 Compensation coils

To gain precise control over the magnetic field background at the experiment, a cage made of six compensation coils is placed around the glass cell. To be also able to generate quantization fields in any direction, all coils are water cooled to allow for the generation of high fields.

Mechanical design

The mechanical design of the compensation coils can be seen in figure 3.11 (a). The compensation coil cage consists of 6 reels connected in all eight corners with connector cubes. In the experiment, the coils are mounted via the back compensation coil in z-direction to the vertical breadboard and are supported by two mounting braces fixed to the front z-direction compensation coil to the front horizontal breadboard.
Each of the reels is made from brass featuring a U-shape to wind the wires making up the coils into. Soldered to the brass reel is a copper pipe for water cooling. To enhance the heat conductance of the design the wires are glued into the reel using thermal conductive, yet electrically insulating epoxy[12]. All reels feature a round design with the radius of curvature of the edges

[12]Polytec TC 423-2, heat conductivity of 3 W/mK

optimized to allow the wire to lay flat to the reel even in the corners to avoid areas where the wire is not cooled efficiently. Both features are significant upgrades to earlier designs used in the group and allow for great flexibility in the generation of magnetic fields. The hoses are fixed to the copper pipes used for cooling using compression fittings to safely secure them.

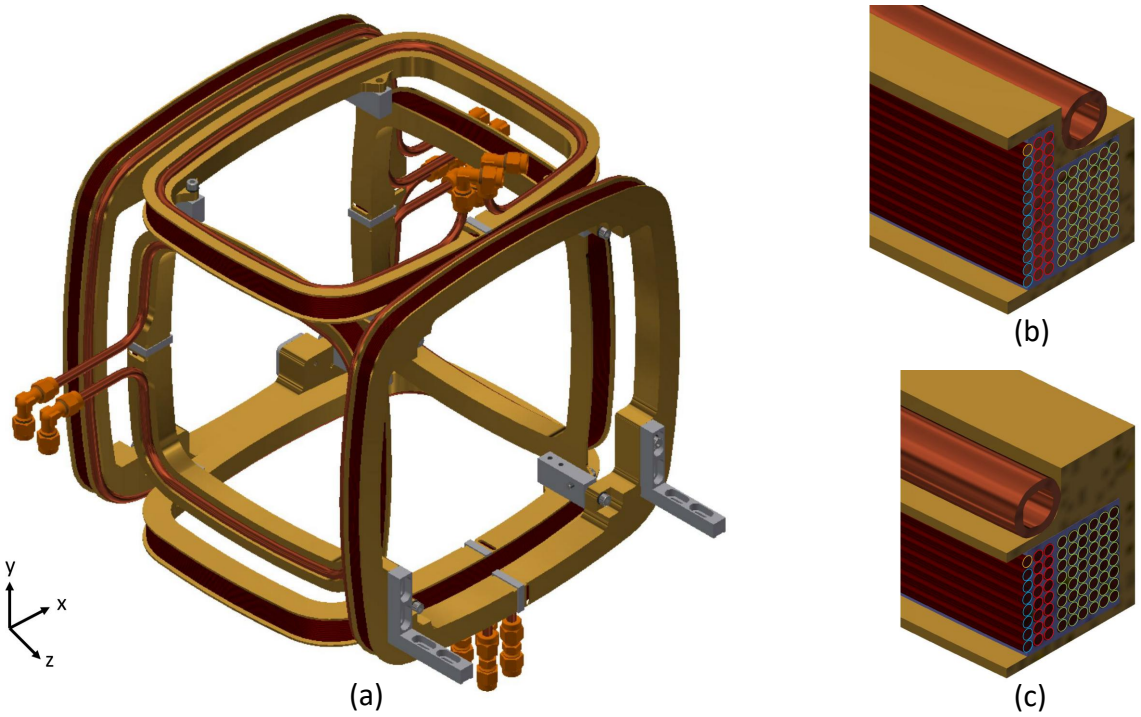

Figure 3.11: (a) The water-cooled compensation coil cage. (b) Internal layout of the compensation coils in x- and y-direction. Each reel houses three layers of wire, layer 1 (green) consisting of a 8 x 6 wire package, layer 2 (red) consisting of a 12 x 2 wire package and layer 3 consisting of a 11 x 1 wire package. A single winding (yellow) is included as a radiofrequency coil. (c) Internal layout of the compensation coils in z-direction. Compared to the other two directions, layer 2 and 3 consist of a wire package 8 x 2 and 7 x 1 respectively.

The internal structure of each reel can be seen in figure 3.11 (b,c). Each reel features three separate coils of different winding number of double-insulated copper wire[13]. This design choice has two reasons, first because of the different amount of windings all coils have a different inductance and thus time constant in which the current in them can be switched. Thus, depending on the experiments performed the right coil pair might be chosen depending on time scales. Second, the setup of three different coils on each axis allows to compensate for an offset field and a residual gradient in each direction while still being able to generate an arbitrary field in any direction. To allow for easy switching of the coil configuration or to connect two coil pairs together to generate an even higher field, the connections of all coils are wired to a patch field for easy configuration.

Also, each of the reels features a single winding of copper wire to serve as a radiofrequency antenna.

The size and distance of the coils is not optimized for a perfect Helmholtz configuration, but

[13]Elosal DR-1250

is rather optimized to use the available space in the tight layouted core of the experiment and allow for passage of laser beams on the diagonal axis of the experiment between the coils and the vacuum chamber.
To monitor the temperature of the coils during operation, a thermistor[14] is glued to each reel as well as a bi-metal switch with a opening temperature of 50 °C to be connected to a interlock system to avoid over heating of the coils during operation. As shown during testing, this system efficiently protects the coil cage against incorrect operation.

Measurements of fields and parameters

Prior to implementation of the coil cage into the experiment, the correct operation of the whole setup was evaluated in a test setup with a 3D Hall sensor to measure the magnetic field generated by all coils. An example scan from this setup can be seen in figure 3.12 showing that the coils are not in Helmholtz configuration. Table 3 summarizes the parameters for all 9 coil pairs.

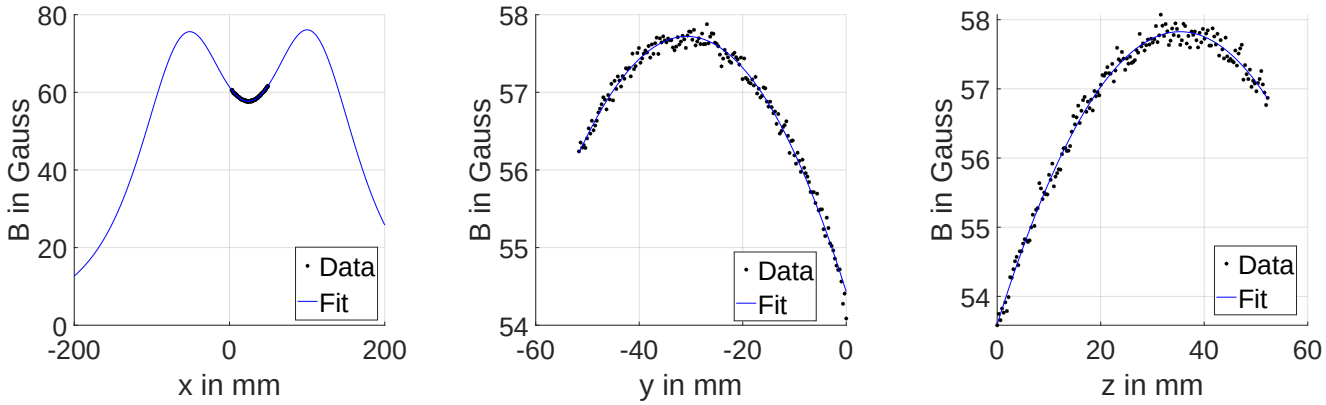

(a) **(b)** **(c)**

Figure 3.12: Example measurement of the magnetic field in Helmholtz configuration generated by the layer 1 of the x-compensation coils in (a) x, (b) y and (c) z direction. The axis correspond to the naming convention at the experiment.

[14] PT-1000

	Layer 1	Layer 2	Layer 3
$I_{\text{max,constant}}$	25.5 A	33.2 A	20 A
$I_{\text{max,cycled}}$	41.07 A	52.86 A	-
B_{AHH}	$\begin{pmatrix} 0.388(1) \\ 0.190(1) \\ 0.191(1) \end{pmatrix}$ G/(cm A)	$\begin{pmatrix} 0.179(1) \\ 0.089(1) \\ 0.088(1) \end{pmatrix}$ G/(cm A)	$\begin{pmatrix} 0.082(3) \\ 0.039(2) \\ 0.043(4) \end{pmatrix}$ G/(cm A)
B_{HH}	2.51(1) G/A	1.26(1) G/A	0.57(1) G/A

(a) x-compensation coils

	Layer 1	Layer 2	Layer 3
$I_{\text{max,constant}}$	25 A	33 A	20 A
$I_{\text{max,cycled}}$	40.62 A	52.86 A	-
B_{AHH}	$\begin{pmatrix} 0.104(1) \\ 0.258(1) \\ 0.150(2) \end{pmatrix}$ G/(cm A)	$\begin{pmatrix} 0.052(1) \\ 0.122(1) \\ 0.072(1) \end{pmatrix}$ G/(cm A)	$\begin{pmatrix} 0.023(1) \\ 0.061(2) \\ 0.035(2) \end{pmatrix}$ G/(cm A)
B_{HH}	1.86(1) G/A	0.91(1) G/A	0.43(1) G/A

(b) y-compensation coils

	Layer 1	Layer 2	Layer 3
$I_{\text{max,constant}}$	26 A	40 A	20 A
$I_{\text{max,cycled}}$	42 A	63.77 A	-
B_{AHH}	$\begin{pmatrix} 0.114(1) \\ 0.113(1) \\ 0.228(3) \end{pmatrix}$ G/(cm A)	$\begin{pmatrix} 0.038(1) \\ 0.036(1) \\ 0.072(1) \end{pmatrix}$ G/(cm A)	$\begin{pmatrix} 0.016(1) \\ 0.018(1) \\ 0.031(1) \end{pmatrix}$ G/(cm A)
B_{HH}	1.98(1) G/A	0.66(1) G/A	0.28 G/A

(c) z-compensation coils

Table 3: Parameters of the compensation coils cage for the coil pair in (a) x, (b) y and (c) z direction. The cycled current is measured for a 10 second long cycle with 40 % duty cycle. Measurements of the maximum currents were conducted with a water flow of 150 L/h. The maximum current is the point at which the bi-metal switches glued to the reels open to trigger the interlock system to shut off the coils, the reel temperature at this point is about 50 °C. For the outer layer 3 with the worst heat conductivity, the maximum current of 20 A is determined by hand as the connection for heat dispersal to the reel is to small.

3.4 Electrodes

As the experiment will employ the interaction between Rydberg atoms to generate entanglement, it is crucial to control the electric field background over the area of the array. For this the core of the experiment features four segment-electrodes placed around the objectives with four segments each. The design is inspired by [54, 98].

Mechanical design

The mechanical design of the electrodes and their holder can be seen in figure 3.13. The electrodes themselves are printed circuit boards with the electrodes being large pads of exposed copper that is gold plated to reduce oxidation. Each of the pads is electronically connected to a wire on the back through a bold screwed into the PCB that also serves as the mounting point to the holder of the electrodes. A shielded SMA wire serves as the connector to the voltage source with only the core connected to the electrode and the shielding grounded to shield the wire from pickup of unwanted stray fields. The electrode-PCB on its holder is screwed to a mounting platform fixed to the same holder the objectives are mounted on. The setup allows access to the screws holding the electrodes in place when implemented into the experiment core and as such the electrodes can be extracted from the experiment without removal of any other parts if needed.

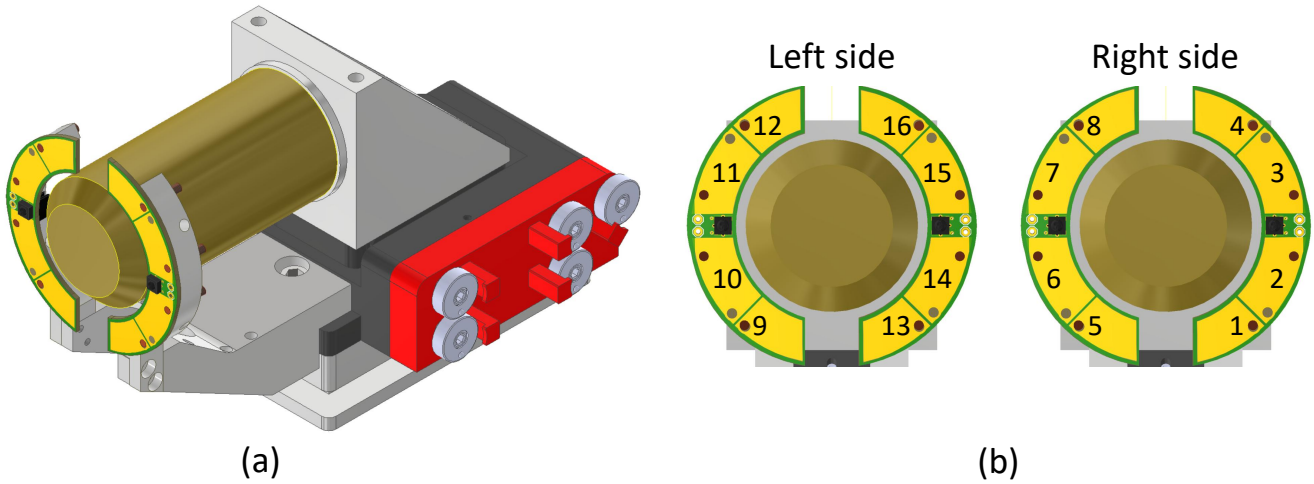

Figure 3.13: (a) The electrode setup mounted to the objective holder. The electrodes are based on PCBs and feature four segments each as well as one high power UV-LED. (b) Naming convention for the 16 electrodes.

Electric control

To generate an electric field in any direction, the voltages applied to the 16 electrodes need to be individual controlled, the formulas to apply a voltage along a certain direction can be found in table 4. This currently planed configuration follows the description in [54, 98].

As in this configuration adjacent electrodes are supplied with the same voltage, a more sophisticated approach may be able to generate more homogeneous fields in middle of the setup when all 16 electrodes are supplied with an individual voltage.

Electrode	Voltage
1	$\frac{1}{2}(-V_x+V_y+V_z)$
2	$\frac{1}{2}(-V_x+V_y+V_z)$
3	$\frac{1}{2}(V_x+V_y+V_z)$
4	$\frac{1}{2}(V_x+V_y+V_z)$
5	$\frac{1}{2}(-V_x-V_y+V_z)$
6	$\frac{1}{2}(-V_x-V_y+V_z)$
7	$\frac{1}{2}(V_x-V_y+V_z)$
8	$\frac{1}{2}(V_x-V_y+V_z)$
9	$\frac{1}{2}(-V_x+V_y-V_z)$
10	$\frac{1}{2}(-V_x+V_y-V_z)$
11	$\frac{1}{2}(V_x+V_y-V_z)$
12	$\frac{1}{2}(V_x+V_y-V_z)$
13	$\frac{1}{2}(-V_x-V_y-V_z)$
14	$\frac{1}{2}(-V_x-V_y-V_z)$
15	$\frac{1}{2}(-V_x-V_y-V_z)$
16	$\frac{1}{2}(-V_x-V_y-V_z)$

Table 4: The voltages that need to be applied to each electrode to produce a target voltage along each direction at the experiment. In this configuration, the two adjacent electrodes are supplied with the same voltage.

Simulation of electric fields

To assess the performance of the electric field setup, the field generated by the electrodes in the glass cell is simulated in Comsol. The results can bee seen in figure 3.14 and show that the electrodes generate a field strength of about 0.13 V/(cm) per 1 V applied.

UV-LEDs

The experimental setup includes a total of 9 UV-LEDs[15] operating at a wavelength of 365 nm which all have a total power of 1 W each. Four of the LEDs are placed on clip-on holders on the main coils, four are on the four electrode-PCBs and one is placed on a mount underneath the glass cell. The LEDs are placed so that the whole glass cell can be flood with UV light to get rid of surface charges on the glass cell [99, 54].

[15]Model Osram LZ1-00UV0R-0000,

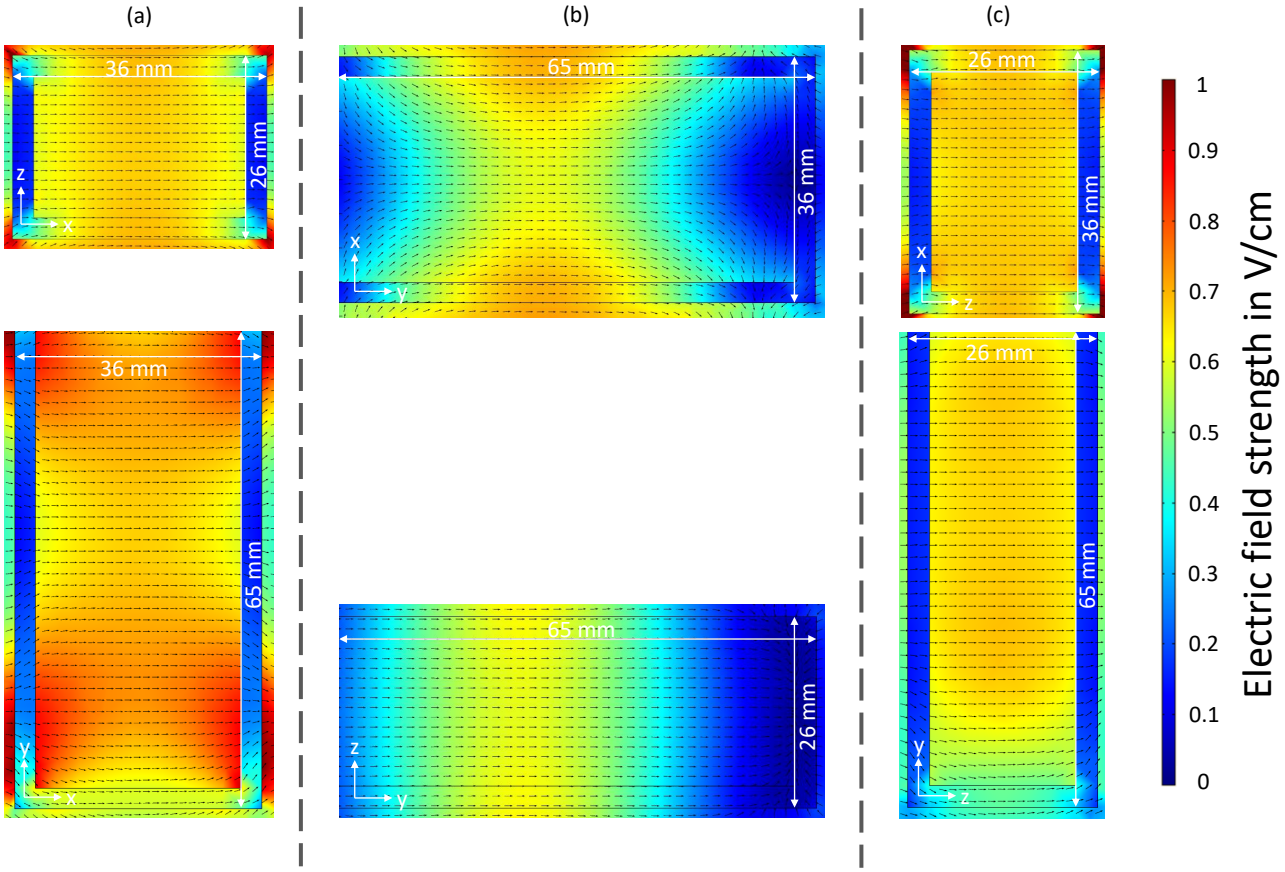

Figure 3.14: Comsol simulation of the electric fields generated by the electrodes for a input voltage of 5 V for (a) a field in x-direction, (b) a field in y-direction and (c) a field in z-direction. The field strength in the center is 0.65 V/cm.

3.5 High-resolution objectives

The central optic for generating the trapping tweezer potentials and imaging the atoms trapped in them are two high-resolution imaging objectives specifically manufactured for the requirements of the experiment.[16] One of the objectives currently used for imaging the tweezer potentials in the analysis branch features a 3 mm hole on its optical axis to allow for global beams to be shone in on the objective axis.

Overview of properties

The main properties of the objectives are summarized in 5.

Numerical aperture	0.5
Field of View	200 µm x 200 µm
Material	ULTEM
Design wavelength	399 nm, 532 nm, 556 nm, 759 nm
Focal shift	< 6 µm over the whole range
Working distance	20 mm
Focal length	28 mm
Back aperture diameter	28 mm
Housing diameter	45 mm
Corrected for	3 mm of fused silica

Table 5: The most important parameters of the high-resolution objectives.

The numerical aperture of 0.5 uses the whole available optical access of the glass cell and is a reasonable value for generating trapping potentials in the form of optical tweezers. The main restrictions on the design besides the achromatic design from 399 nm to 759 nm to include all needed wavelength is the large working distance of 20 mm to be able to integrate the objectives in the experiment. This leads to a large back aperture of 28 mm, the value to which all beam illuminating the objective need to be expanded to. In practice this means that all optics in the objective path need to be 2 inch in diameter to avoid clipping and need to be of excellent optical quality over their whole aperture.

Characterization of imaging performance

To characterize the performance of the objectives, both optics were tested using a star test target in the test setup to measure their point spread function and depth of field. An example measurement can be seen in figure 3.15, for more details on performing star tests see for example [100, 97].
The idea behind performing a star test is to illuminate the objective with a point like source and measure the quality of imaging only limited by the diffraction at the objectives aperture. The image of this point source called the point spread function is the smallest object the objective

[16] Special Optics, 57-27-27@399-759

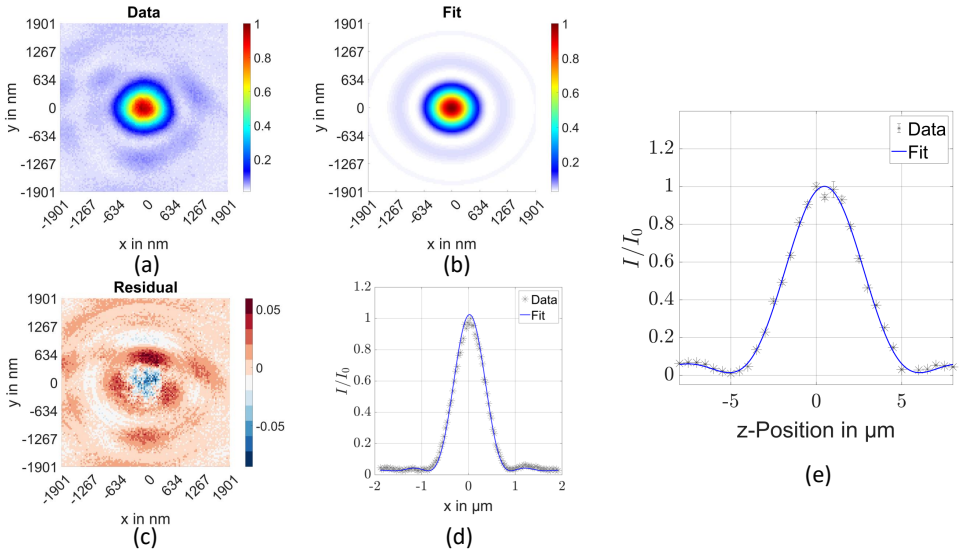

Figure 3.15: (a, b, c, d) Point spread function measured of the objective measured with a star test target for 759 nm light. (a) shows the data, (b) a fit with a two dimensional point spread function, (c) the residual of the fit and (d) a cut along the x direction through the star. The size of the point spread function shows diffraction limited performance with a NA of 0.5. (e) Measurement of the depth of field of the objective performed at 759 nm. The fit with a sinc function also reveals a NA of 0.5.

can image and shows its fundamental imaging properties unaltered by any additional wavefront errors. Thus, the output beam of the objective will be a plane wave.

The functional form of the point spread function and the depth of field can be calculated from the Fresnel diffraction integral, for a more detailed derivation see [101, 102].

The point spread function is the intensity distribution in the focal plain and has the functional form

$$I(\nu) = I_0 \left[\frac{2J_1(\nu)}{\nu}\right]^2 \tag{3.2}$$

with the peak intensity I_0, the radial optical coordinate ν and the Bessel function of the first kind and order one $J_1(x)$. Here, the radial optical coordinate is the radial coordinate re-scaled by the numerical aperture NA and of the system and the wavelength λ used for imaging $\nu = \frac{2\pi \mathrm{NA}}{\lambda} * r$.

Similarly, the intensity distribution along the optical axis of the system can be shown to follow the functional form

$$I(z) = I_0 \left[\frac{sin\left(\frac{\pi z}{2\Delta z}\right)}{\left(\frac{\pi z}{2\Delta z}\right)}\right]^2 \tag{3.3}$$

with the axial coordinate z and the depth of field $\Delta z = \frac{\lambda}{\mathrm{NA}^2}$.

As can be seen both measurements give access to the numerical aperture of the imaging system as the key parameter for its imaging performance.

Testing of both objectives at all wavelength[17] showed diffraction limited performance with a numerical aperture of 0.5 or slightly above.

[17] That is 399 nm and 556 nm used for imaging of the atoms, 578 nm used for clock excitation and 759 nm used for trapping the atoms.

Simulation of imaging performance with bend glass cell

As discussed in section 3.2, the glass cell used at the experiment is subject to bending when under vacuum because of its relatively thin walls of 3 mm thickness.
To assess the effect of this on the performance of the objective, a simulation of the imaging was done with the surface profile of the bend cell in ZEMAX, the results of which can be seen in figure 3.16. The simulated pupil functions of the objective with and without the bend cell show a rms wavefront error of well below 7 % and are thus considered diffraction limited. The wavefront error only shows minimal altering by the surface profile, indicating that diffraction limited imaging is possible with the experimental setup.

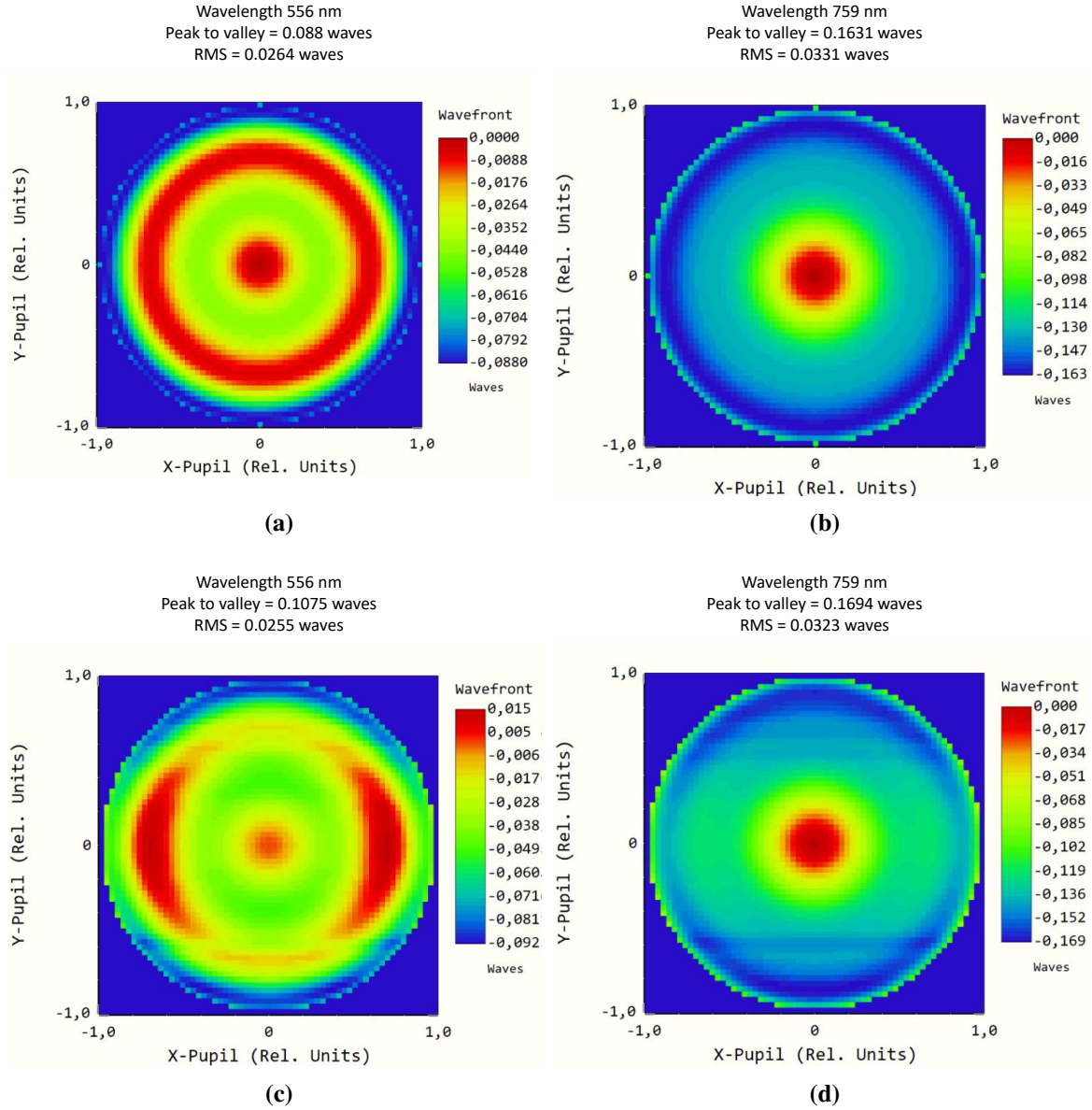

Figure 3.16: The pupil function of the objective as simulated by ZEMAX for (a, c) 556 nm light and (b, d) 759 nm light. (a, b) include a flat glass cell profile and (c, d) a bend glass cell. The wavefront peak-valley and rms error get altered only minimally by the bend cell wall, still showing diffraction limited performance with an rms wavefront error smaller than 7 %.

4 Setup for atom trapping and imaging

This chapter illustrates the setup and characterization of the optical setups used for generation of tweezer arrays and for imaging of the atoms. It presents the setups used for high-fidelity imaging of single atoms using fluorescence imaging and for generation of tweezer arrays with the aid of a pair of acousto-optic deflectors (AODs) at the wavelength of 532 nm. Further it describes an analysis setup used for detailed characterization of the optical tweezers and gives an overview of the general optical shape of a tweezer generated with a microscope objective and closes with the analysis of the performance of the machine in generating tweezer arrays AODs. The concepts for the setups were envisioned by C. Becker, N. Pintul and the author and discussed by the whole team. The performance of the setup was checked in a test setup during the master thesis of J. Rauchfuß and O. Murzewitz, see [103, 104]. Final implementation of the setup at the experiment and final characterization was done by N. Pintul and the author with help from J. Rauchfuß. The program to homogenize the array was written by J. Rauchfuß and the author. All work was performed under the supervision of C. Becker and K. Sengstock.

4.1 Single atom imaging

For fluorescence imaging of single atoms, the light scattered by the atoms is collected by the same high-resolution objective used for generating the trapping tweezer potentials. The setup can be seen in figure 4.1.

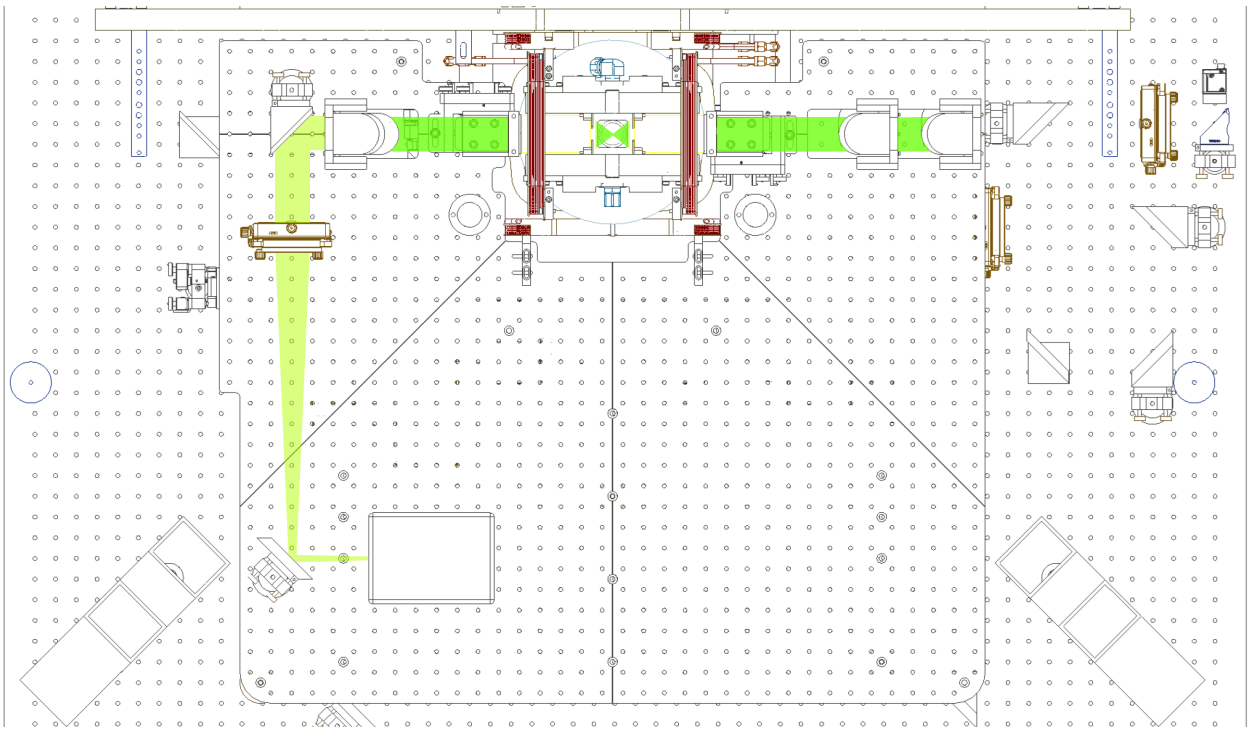

Figure 4.1: The setup for imaging of single atoms. The fluorescence light is collected by the same objective used to focus down the tweezer light. The fluorescence is separated from the tweezer light by a dichroic mirror and is focused on a scientific CMOs camera by a singlet lens of 500 mm focal length.

The light is split off from the tweezer light using a dichroic mirror and is focused onto the camera[18] by a singlet lens of 500 mm focal length. This setup leads to a magnification of 17.6 and images the the photons scattered by each individual atom onto an 7 by 7 pixel area on the camera, a good compromise between achieving a good signal to noise ratio and resolving the features of the point spread function.

4.2 Tweezer analysis setup

To achieve a near-diffraction limited performance of the tweezer generation setup, it is necessary to be able to analyze the tweezer potentials precisely. For this, the experiment employs the setup shown in figure 4.2. Part of the tweezer light that is recollimated by the second objective is picked off by an uncoated glass substrate. After being deflected from the horizontal breadboard to the optical table, the light is focused by an achromatic lens of 750 mm focal length onto a CMOS camera[19]. This imaging system has a magnification of 26.8 and focuses the tweezer light onto an area of about 16 by 16 pixel, large enough to resolve all relevant features yet small enough to cover the whole field of view of the objective. The beam is split once more after the first lens by another uncoated glass substrate and is recollimated by an 125 mm achromatic lens to a beam diameter of 4.6 mm to be analyzed by a Shack-Hartman sensor [20].

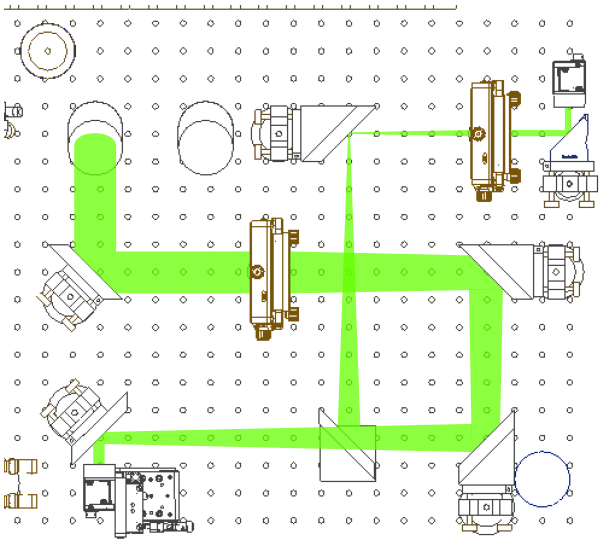

Figure 4.2: The setup used for analyzing the performance of the tweezer generation. Light picked up by an uncoated fused silica beam sampler on the horizontal breadboard is focused down on an analysis camera by a achromatic lens of 750 mm focal length. The beam is split once more after the lens by another uncoated fused silica beam sampler and is recollimated by a achromatic doublet lens of focal length 125 mm to be analyzed by a Shack-Hartmann sensor.

This setup with a second objective imaging the tweezer potentials has the advantage of analyz-

[18] Hamamatsu ORCA Quest qCMOS camera
[19] Basler acA3088-57um, cover glass removed.
[20] ImagineOptics HASO-4 broadband

ing the potentials after they have also passed through the glass cell compared to other setups where the light is picked off before being focused down by the first objective. In this way also aberrations caused by the objectives themselves are visible on the tweezers imaged onto the camera and serve as a reference to adjust both the objectives in relation to the glass cell and one another as well as for incoupling of the tweezer light into the first objective. The combination with a Shack-Hartman sensor also gives access to direct analysis of the wavefront and the sensor can later be used in conjugation with an adaptive optics element like a spatial light modulator to further reduce the effect of unwanted aberrations. In practice, the most important reference is the image of the array imaged onto the camera, which is enough to adjust all optics to near-diffraction limited performance.

4.3 AOD tweezers

For all characterization done in this work, the atoms are trapped in a 12 by 12 site tweezer array generated by a pair of acousto-optic deflectors [21] (AODs). In the final stage of the experiment, this setup will be used to sort into defect-free arrays, but as the operating wavelength of 532 nm is a near magic wavelength for the $^1S_0 - ^3P_1$ transition in ^{174}Yb, it also lends itself for trapping single atoms from a magneto-optical trap to study the performance of the machine.

Optical setup

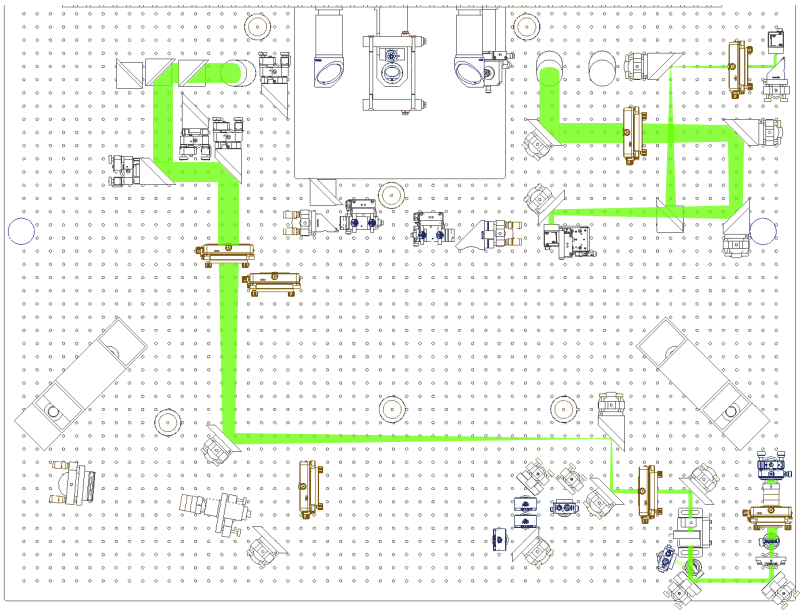

Figure 4.3: The setup used for generation of a tweezer array by the use of a pair of crossed acousto-optic deflectors (AOD) at 532 nm. For more detail see main text.

The setup for generation of optical tweezers by a pair of acouto-optic deflectors can be seen in figure 4.3. The light supplied from the laser system[22] by a high-power photonic crystal fiber is

[21] AA opto-electronic DTSXY-400-532
[22] For details see [94].

coupled out placing the fiber in a corresponding holder in a 5 axis mirror mount. After this the polarization is cleaned by a rotatable polarizing beam splitter cube and the light is collimated by a lens of focal length 75 mm. The beam size is clipped to about 4.5 mm by an iris aperture before entering the acousto-optic deflector. A half waveplate before the AOD is used to set the polarization for the AODs and a beam sampler is used to pickup a small amount of the light to a photodiode used for intensity stabilization. After passing through the AODs all but the correct diffraction order are blocked and the beam is expanded by a telescope consisting of a achromatic doublet of 160 mm focal length and a singlet lens of 1000 mm focal length in 4-f configuration to a beam size of 28 mm to fill the backfocal plane of the high-resolution objective. The beam passes through a dichroic mirror used to overlap tweezer potentials at 532 nm with those from the SLM at 759 nm and is lifted by a beamlift to the front horizontal breadboard entering the objective located there.

Radiofrequency optimization

Each of the acousto-optic deflectors is driven by a channel of a FPGA-based frequency source[23]. To generate not a single tweezer but a rectangular array, each of the AODs has to be driven by a multifrequency waveform. As the defelctors are placed behin each other in a right angle, each of the tones applied to the first AOD will be split into a line by the second AOD and as such the sites in an array are not independent. As driving with a multifrequency waveform will lead to unwanted interference between the tones and higher-harmonics from frequency mixing by non-linear elements, the applied waveform has to be correctly chosen. For a multifrequency waveform the most important factor is the crest factor

$$CF = 20 * log_{10}(\frac{\text{Peak amplitude}}{\text{rms value}}) \tag{4.1}$$

which expresses how high the peaks in the waveform compared to its rms value are. This is of importance for various reasons:

- High voltage peaks might damage the experimental equipment
- High voltage peaks might lay outside the supported range of the radio-frequency amplifiers used, meaning they will be operated outside their linear range leading to unwanted higher harmonics.
- The peak voltage might be outside the amplitude range the frequency source supports, leading to unwanted clipping and again the presence of unwanted frequency components.

For the setup used during this thesis the biggest concern is the clipping of the initial waveform as can be seen from figure 4.4. There are a number of algorithms to reduce the crest factor of a waveform, the one employed here is the choice of the phases of each of the frequency tones making up the waveform to be chosen according to the Kitayoshi algorithm [105]:

[23] Quantum Machines OPX+

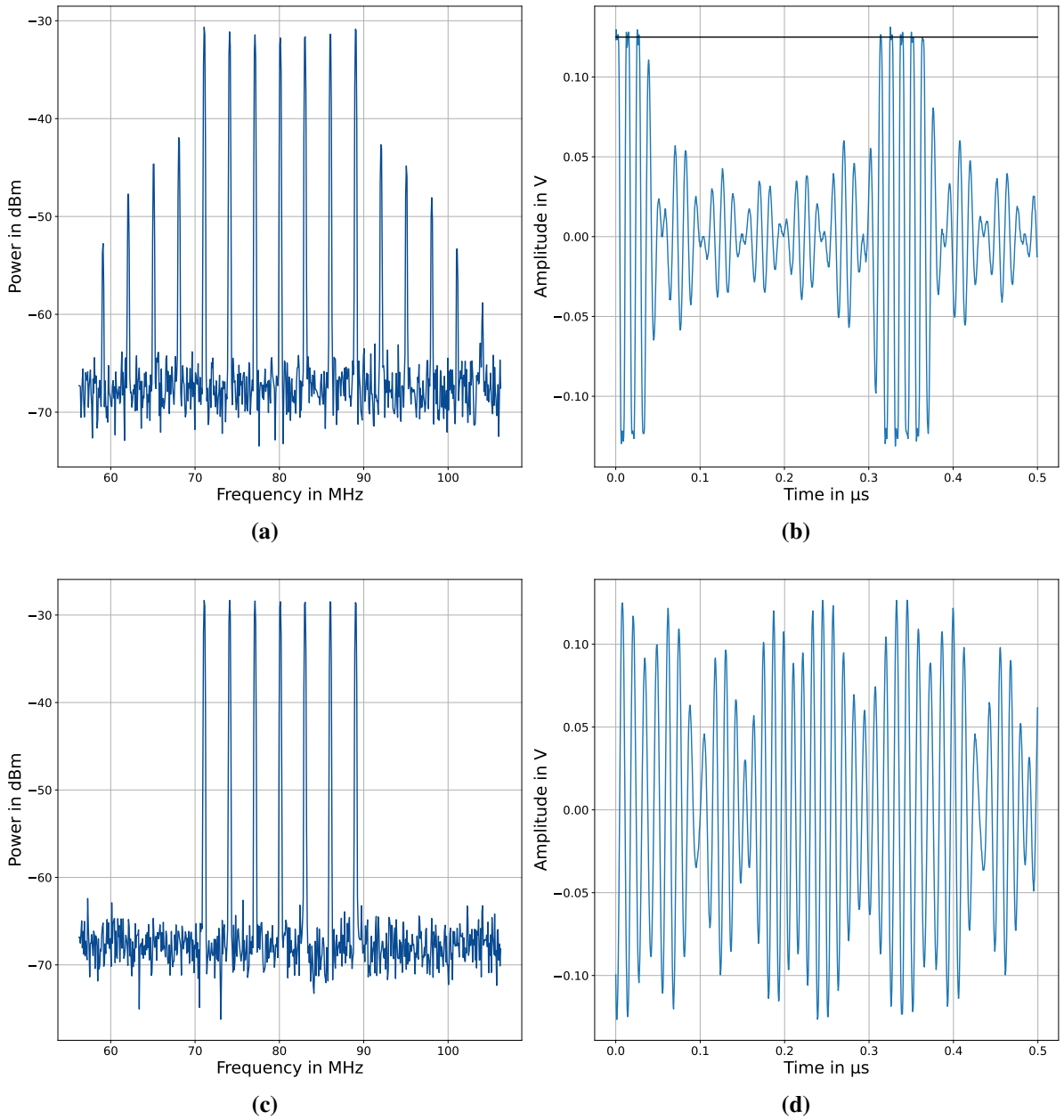

Figure 4.4: (a) spectrum and (b) waveform of the radiofrequency signal used to generated a 7-tone tweezer array when the phases of the frequency tones are all the same. Because of the unfavorable way the tones interfere, the signal has a high crest factor and the peak voltage of the signal exceeds the maximum the frequency source is capable of, leading to clipping at the black line of 0.125 V. Correspondingly the spectrum is distorted and shows unwanted frequency components. (c) spectrum and (d) waveform when the phases of the combined waveform are chosen according to the Kitayoshi algorithm. The interference of the tones is optimized to reduce the crest factor and the spectrum is clean of unwanted frequencies. The crest factor of (b) is 8.3, the crest factor of (d) is 5.3. Note that a single sine wave has a crest factor of 3.

$$\Theta_k = \frac{\pi}{N} * k * (k+1) \tag{4.2}$$

where N is the number of frequency tones and k is the index of the tone.
With this choice of phase, the crest factor and clipping of the waveform can be reduced to zero leading to a clean waveform free of unwanted frequency components to drive the AODs.

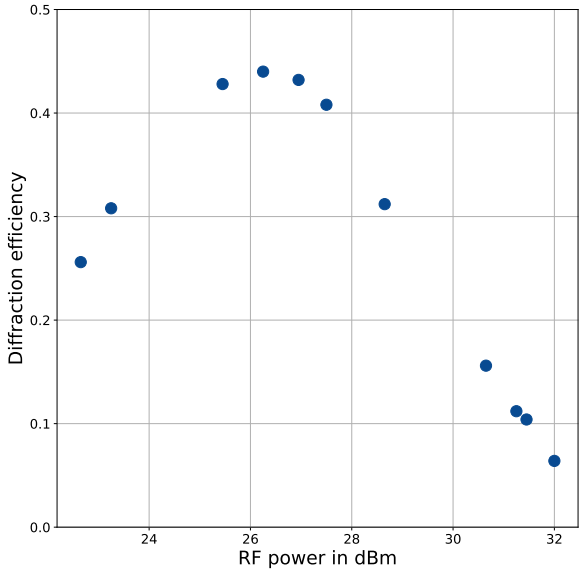

Figure 4.5: Diffraction efficiency of the AODs for varying power of the multifrequency waveform applied. The optimal diffraction efficiency is reached for about 26.5 dBm, the same power a single tone waveform would require.

With the overall waveform optimized, the last step is to optimize the overall power of the waveform as can be seen in figure 4.5. The maximum diffraction efficiency is reached for an input power of 26.5 dBm, about the same power that maximizes diffraction for a single frequency applied to the AODs.

Intensity homogenization

To homogenize the intensity of the tweezer traps, the image taken by the camera in the analysis branch of the experiments is analyzed. A simple linear feedback algorithm is used to correct the amplitude of each frequency component to homogenize the array. Let F_i be the waveform of iteration i consisting of k frequency components f_k with initial amplitude 1, then the waveform is

$$F_i = \sum \sigma_{i,k} * f_k \tag{4.3}$$

with the amplitude correction factor

$$\sigma_{i,k} = \sigma_{i-1,k} * \frac{\bar{I}_{\mathrm{2D-Array}}}{\bar{I}_k} \tag{4.4}$$

where $\bar{I}_{\mathrm{2D-Array}}$is the mean intensity of the whole array and $\bar{I}_k$ is the mean intensity of either the

row or the column corrected.
This correction algorithm is applied to both rows and columns simultaneously, as they naturally couple when using crossed AODs as discussed before.

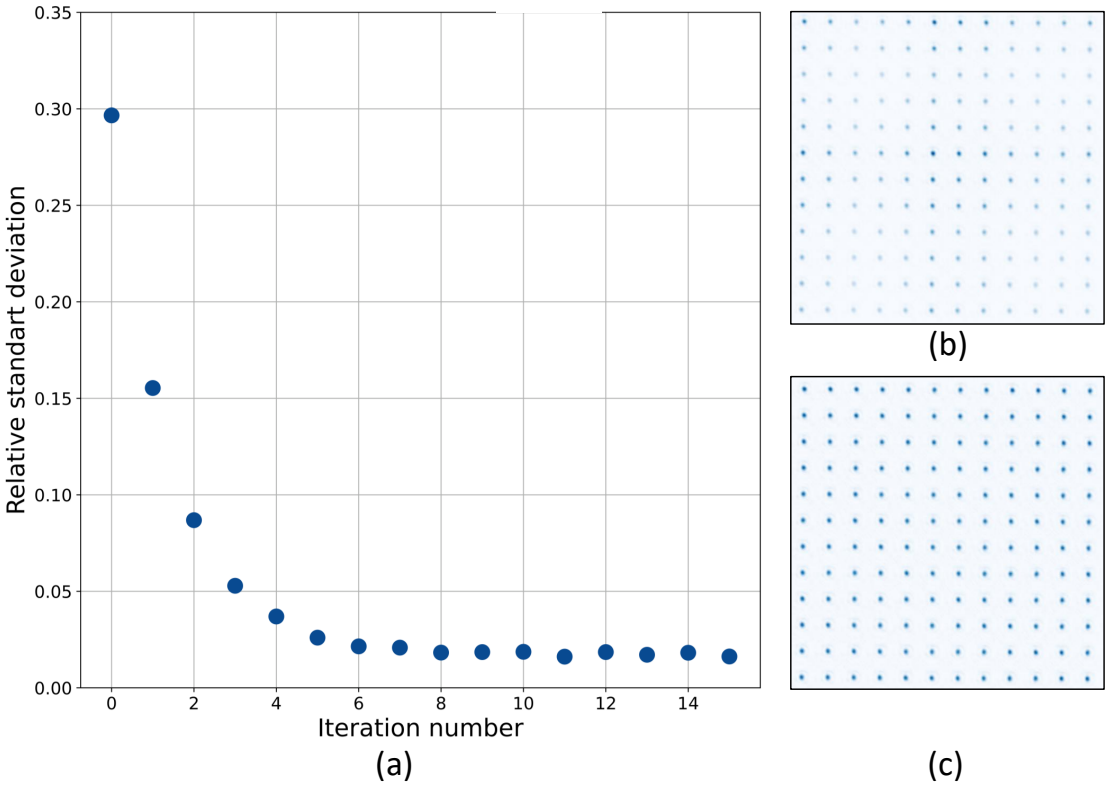

Figure 4.6: (a) Intensity homogenization run of the AOD tweezer array. Initially starting at about 30 %, the variation in intensity between the sites in an 12 by 12 tweezer array is reduced to about 2 % after 8 iterations. (b) The initial array at iteration 0 and (c) the final array at iteration 16.

The algorithm reduces the variation in intensity of the tweezers over the array from initially 30 % to about 2 % in a few iterations as can be seen in figure 4.6.
It is noteworthy that this might still not mean that all atoms experience the same potential, as only the intensity as seen on the camera is homogenized. A more sophisticated method using direct feedback from the atoms like the light shift per site or the precise frequency of the clock transition might be used in the future.

Optical shape of a tweezer

As discussed in section 3.5, the smallest spot that can be generated by an objective is the point spread function. This smallest spot will be achieved when the objectives back aperture is illuminated with a plane wave, an extreme limit that is never the case when working with gaussian laser beams to generate an optical tweezer array. Thus it is worthwhile to discuss the optical shape of a tweezer generated by illuminating an objective with a gaussian laser beam.

The general shape of the generated optical potential will depend on the so called fill factor

$$F = \frac{w_0}{r_{BA}} \tag{4.5}$$

the ratio between the waist w_0 of the gaussian beam and the radius of the back aperture of the objective r_{BA}.
In the case that the fill factor is a lot smaller than one, the shape of the generated optical potential will be gaussian, but as the back aperture is not illuminated to its full extent the waist of the tweezer will be larger than the minimal achievable spot size.
In the case that the fill factor is a lot larger than one, the generated optical potential will have the shape of a point spread function. Of cause in this limit a large part of the beam and thus the optical power available will be clipped.
The effect of the fill fraction on the minimal achievable waist can be seen in figure 4.7.

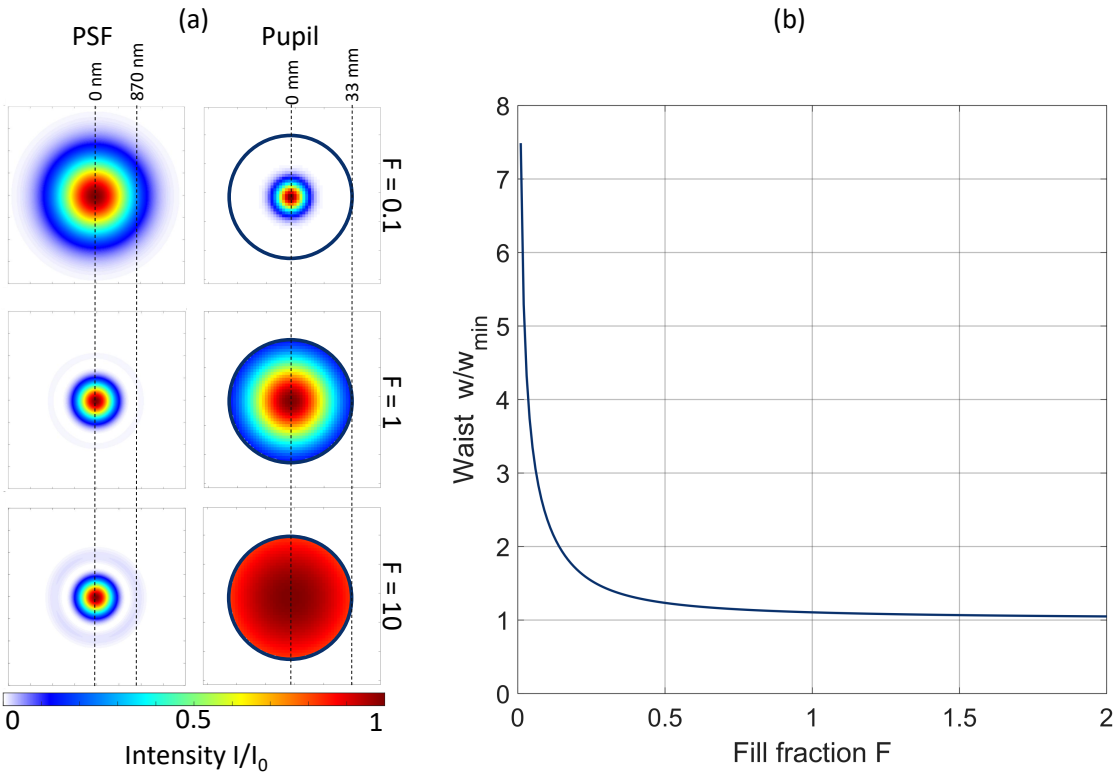

Figure 4.7: (a) The point spread function and pupil function for different fill fractions. The circle in the plots of the pupil has the radius of the objectives back aperture. When working with small fill fractions the objectives generates a gaussian beam with larger waist than minimally achievable. For large fill fractions, the optical potential has the shape of a point spread function. (b) The effect of the fill fraction on the waist of the generated tweezer in terms of the minimally achievable waist w_{min} that is achieved for $F \to \infty$.

In practice it is best to work with a fill factor close to one, rendering the generated optical potential a convolution between a point spread function and a gaussian beam. The power optimal value for the fill factor in terms of achievable trap depth is close to 0.9 as shown in [106].

When analyzing the tweezers, the biggest difference between a gauss and a point spread function is in the shape along the optical axis, as the power in a point spread function that is defocused is transferred into the ring structure but the waist along the axis does not vary as strong as one would expect from a gaussian laser beam. Thus the ratio between axial and radial waist and corresponding the expected ratio of the trap frequencies will be larger than for a gaussian laser beam. Contrary, the shape in the focal plane can still be well approximated by a gaussian. For a comparison of both shapes see figure 4.8.

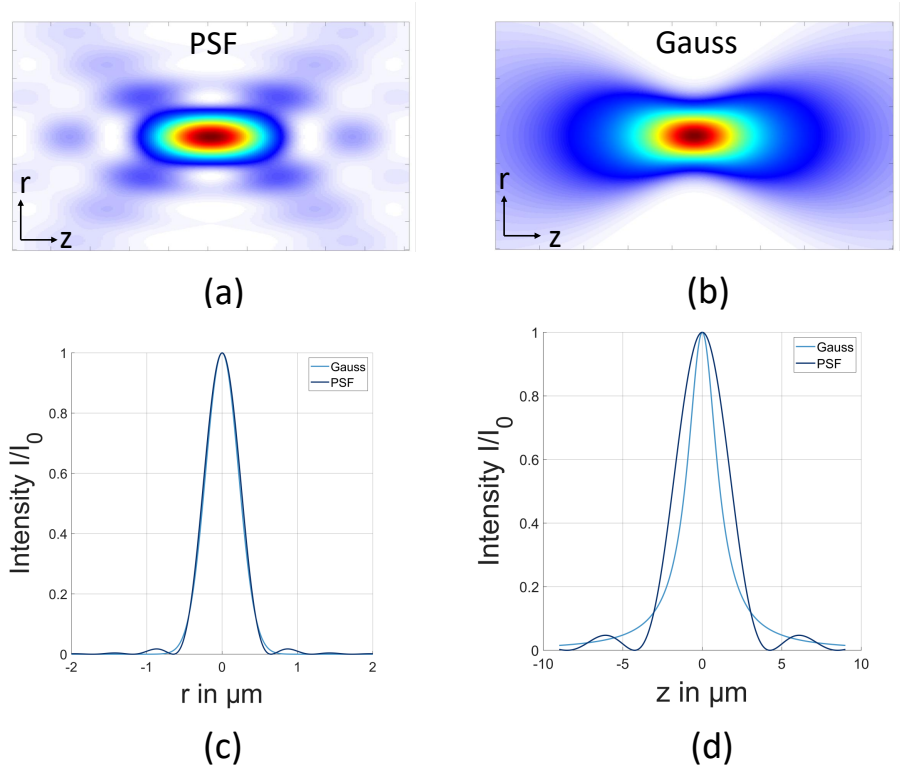

Figure 4.8: A plot of the intensity distribution in the radial-axial plane of (a) a point spread function and (b) a gaussian of 436 nm waist. The biggest difference is in the intensity distribution along the optical axis, the point spread function showing its typical ring structure while the gaussian beam just expands in a square-root behavior. (c) Cut along the radial direction of both a gaussian and a point spread function. Although the point spread function has its typical ring, the central peak that traps the atoms is well approximated by the gaussian. (d) A cut along the axial direction. The difference between the two functions is visible, the point spread function being considerably larger than the gaussian beam.

As an additional effect besides the fact that a real tweezer will be a convolution between a gaussian beam and a point spread function, it is also important to keep in mind the size to which the back aperture of the objective is illuminated. The before mentioned considerations all assume that the back aperture is filled to its full extent, but in a real experimental setup it might be necessary to clip the input beam to a size smaller than the whole aperture even though the fill fraction may be large or the the objective might even be illuminated with a plane wave.

This fact can be expressed in the illumination fraction

$$\mathrm{I} = \frac{r_{\mathrm{Beam}}}{r_{\mathrm{BA}}} \tag{4.6}$$

the ratio between the radius r_{Beam} at which the beam is clipped and the radius of the back aperture of the objective.
A possible reason for this is the fact that one might not want to illuminate the housing of the objective to avoid reflections or fluorescence from the housing.
When not illuminated to its full extent, the reduced radius of the beam on the back aperture will effectively reduce the numerical aperture of the objective as if the back aperture was as small as the clipped beam radius. The effect of this can be seen in figure 4.9.

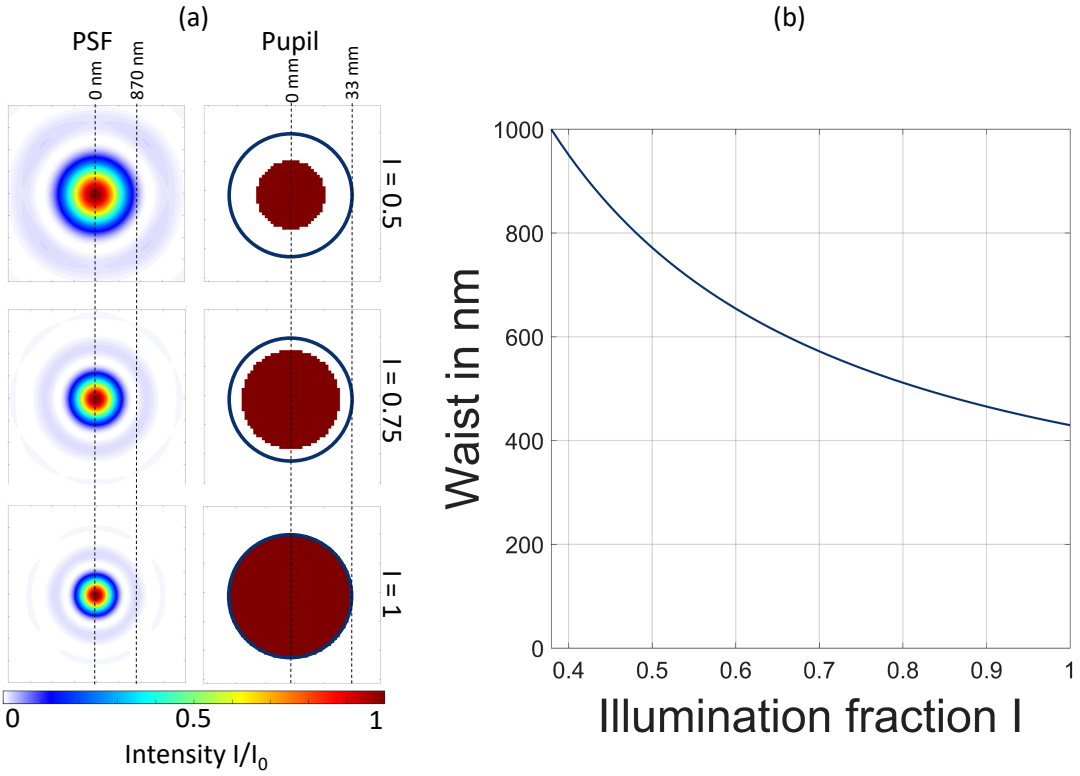

Figure 4.9: (a) Point spread functions and pupil functions for different illumination fractions. The circle in the pupil functions has the radius of the objective aperture. As the input is always a plane wave, the resulting optical potential has the shape of a point spread function but the size depends on the illumination fraction. (b) The effect of the illumination fraction on the waist of a tweezer generated by an objective of numerical aperture 0.5 and a input light of wavelength 532 nm.

Performance

To assess the performance of the optical setup, the radial and axial waist of the tweezers as measure for their confinement on the atoms are extracted from to measurements.

To find the radial waists, an image of the tweezer array in focus is taken and each tweezer is fitted with an elliptical gaussian with arbitrary angle Θ of the form

$$\sigma(x,y) = \sigma_0 * \exp(-2*(a*(x-x_0)^2 + 2*b*(x-x_0)*(y-y_0) + c*(y-y_0)^2)) \tag{4.7}$$

with the parameters

$$a = \frac{\cos(\Theta)^2}{\sigma_x^2} + \frac{\sin(\Theta)^2}{\sigma_y^2} \tag{4.8}$$

$$b = -\frac{\sin(2*\Theta)}{2*\sigma_x} + \frac{\sin(2*\Theta)}{2*\sigma_y} \tag{4.9}$$

$$c = \frac{\sin(\Theta)^2}{\sigma_x^2} + \frac{\cos(\Theta)^2}{\sigma_y^2} \tag{4.10}$$

An example fit and the mean waist can be seen in figure 4.10.

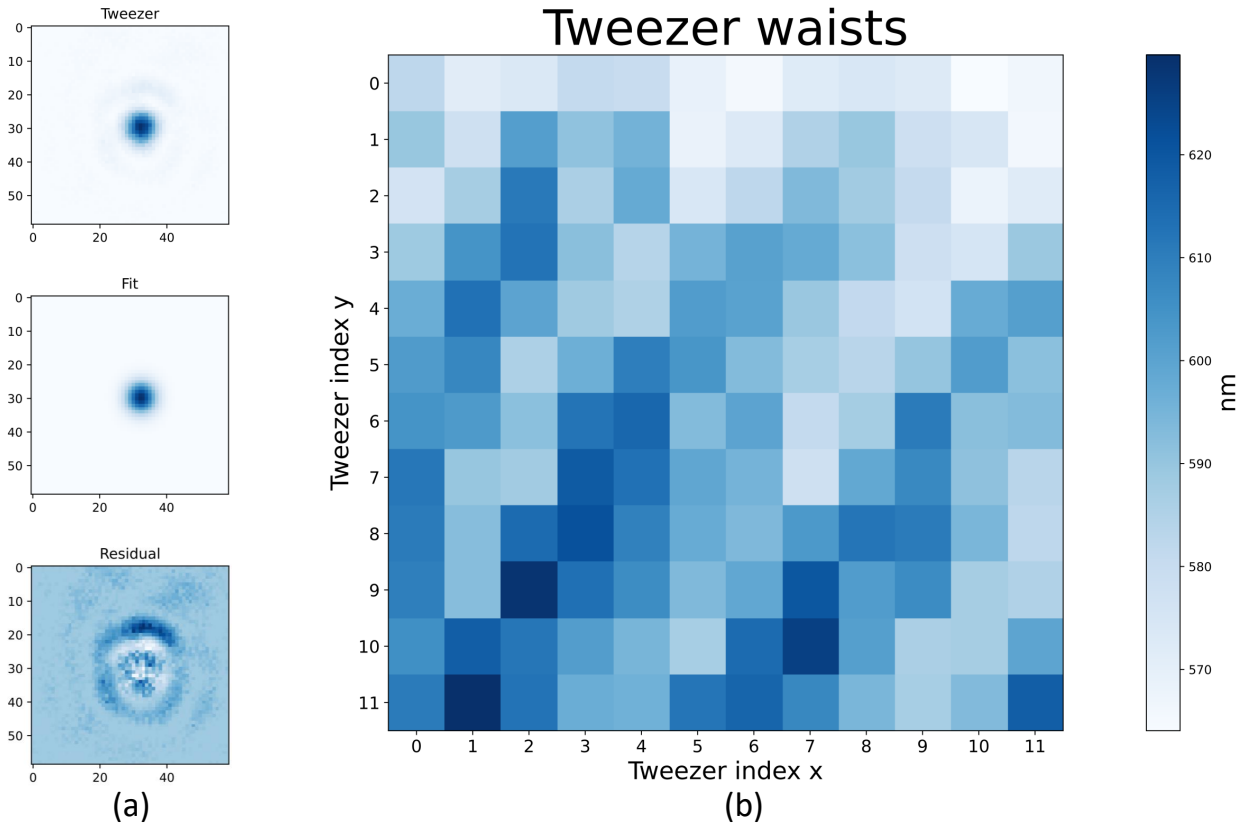

Figure 4.10: (a) Example fit of a tweezer potential with the corresponding fit with a gaussian and the residual of the fit showing the ring structure of a point spread function. (b) Mean tweezer waist for all sites in an 12 by 12 tweezer array. The mean over the whole array is $595 \pm 15\,nm$, the homogeneity of the waist over the array is 2.5 %.

The mean waist over the whole array is $595 \pm 15\,nm$ with a variation of about 2.5 % over the array.

To measure the axial extend of the tweezer δ_z, the position along the beam axis of the analysis camera is scanned and the resulting intensity in the middle of the tweezer is extracted and fit with a sinc function of the form

$$\sigma(z) = \sigma_0 * \mathrm{sinc}(\frac{\pi * (z - z_0)}{2 * \delta_z})^2 \tag{4.11}$$

A example scan and fit can be seen in figure 4.11 (a) and (b) and the performance over the whole array can be seen in 4.11 (c). The average extent of the tweezer along the axial direction is $5.3 \pm 0.2\,\mu m$ and the homogeneity over the array is 2.8 %, comparable to the variation in radial direction.

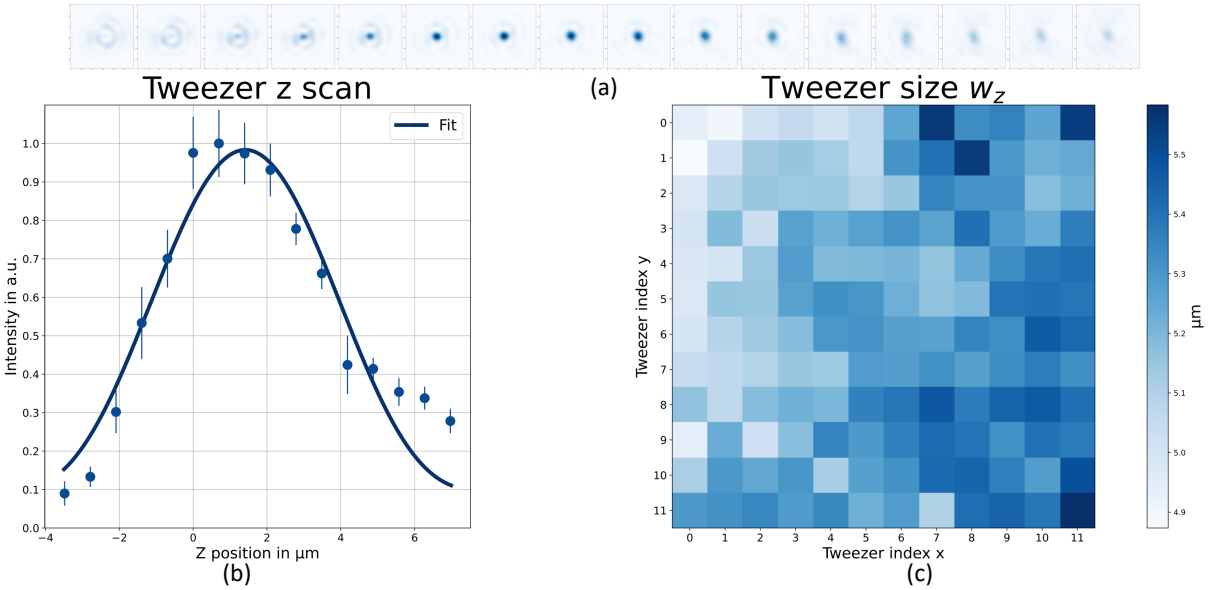

Figure 4.11: (a) Tweezer images for the z positions corresponding to the data points (b). All images are plotted with the maximum intensity set to the value of the tweezer in focus. (b) Example of the center intensity of the tweezer along the optical axis with a fit according to equation 4.11. The error on the data points is the standard deviation of averaging over the center 9 data points, averaging is done to reduce error from position fluctuations. (c) Waist along the optical axis of the tweezer for every site in an 12 by 12 tweezer array. The average waist is $5.3 \pm 0.2\,\mu m$ and the homogeneity over the array is 2.8 %.

The size of the tweezers is noticeably larger than one would expect from the theoretical point spread function[24] of an objective with numerical aperture of 0.5, namely

$$w_r^{\mathrm{psf,532\,nm}} = 0.41\frac{\lambda}{NA} \sim 436\,nm \tag{4.12}$$

and

$$w_z^{\mathrm{theo,532\,nm}} = 1.4\frac{\lambda}{NA^2} = 2.98\,\mu m \tag{4.13}$$

[24]Both prefactors give the point at which the intensity along radial and axial direction respectively has dropped to $1/e^2$ of its maximum value.

This has two main reasons, first the theoretical minimum value is only reached when the back aperture of the objective is illuminated with a homogeneous beam. For real experiments working with gaussian beams, the best compromise for creation of deep traps between the achievable waist and the waste of power because of clipping is to form the beam such that it is clipped at around 90% of its gaussian waist w_0. [106] As a second reason, in the experiments performed it was not possible to illuminate the objective back-aperture to its full extent, as the fluorescence of the objective housing material when illuminated with 532 nm light has significant spectral weight at 556 nm which is used for imaging. Because of this the objective is only illuminated to about 70 % of the usable diameter which well explains the larger waist as can be seen from the calculations presented in figure 4.9.
One additional reason might be aberrations on the beam, which can largely be neglected as visible in figure 4.12.

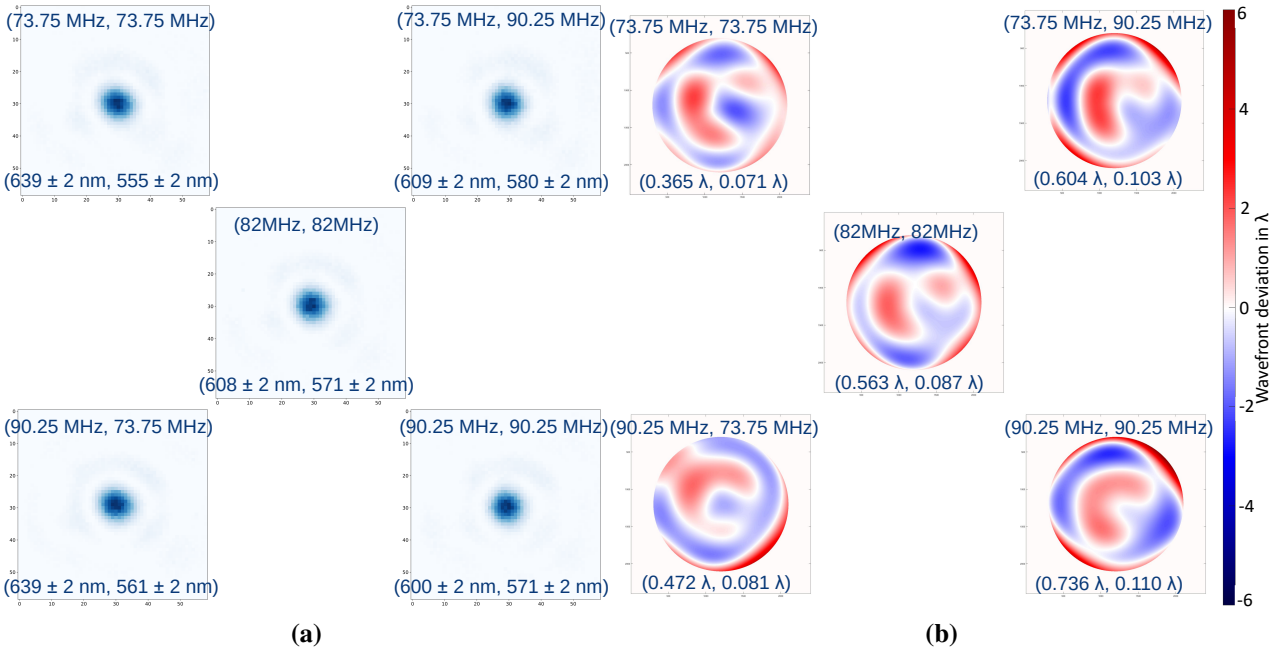

Figure 4.12: (a) Tweezer image and (b) wavefront for a tweezer in the middle and all edge points of the field of view of the objective. The insets in (a) are the major and minor waist of the tweezer and the insets in (b) are the peak-valley and rms wavefront error. The setup shows near diffraction limited performance over the whole field of view.

Overall the performance of the imaging objectives is as expected from the limited illumination of the back aperture necessary due to the fluorescence light from the housing. 6.1 In principle the illumination could be extended with the aid of additional spectral or spatial filtering of the fluorescence light from the atoms to reduce the amount of stray light on the camera. The smaller waist and more efficient utilization of power would make the tweezer generation system more efficient, making the generation of larger arrays possible. The achieved homogeneity in intensity and extent might be improved in the future with feedback directly from the atoms for example by measuring local light shifts. This method will lead to all atoms seeing the same trap depth as combined measure for the size and intensity of the tweezer.

Still, in the current configuration the system performs well at trapping and imaging single ^{174}Yb atoms 6. In the final stage of the experiment, the setup will be used for sorting single atoms in static tweezers generated by a spatial light modulator at 759 nm. For this task, the requirements in homogeneity and the amount of tweezers than can be generated at once will be eased, as no experiments will be performed in the tweezers and fewer tweezers than used during this thesis will be needed even for parallel sorting.

5 3D MOT performance

This chapter illustrates the setup and characterization of the 3D-MOT performance. After describing the laser system and electronic control system used for generation of the light for the magneto-optical trap and showing the optical layout of the beams, it gives a detailed characterization of the loading and compression of the 3D-MOT used for efficient loading of atoms into the optical tweezers. The laser system and broadening setup was build by Dr. A. Ilin, the laser system for imaging the MOT was build by Dr. K. Sponselee, the 2D-MOT setup was kept from the old experiment, for details see for example [107]. The MOT divider setup was build by N. Pintul, the 3D-MOT and imaging setup was build by N. Pintul and the author. The experimental control system was implemented by J. Deppe [108] and the live analysis scripts were writen by J. Rauchfuß and the author. The experimental data was taken and analyzed by the author with N. Pintul. All work was performed under the supervision of C. Becker and K. Sengstock.

5.1 Laser system

The laser light for magneto-optical trapping on the intercombination line is derived from an frequency doubled Toptica laser locked to an ULE cavity, a sketch of the laser system can be seen in figure 5.1.

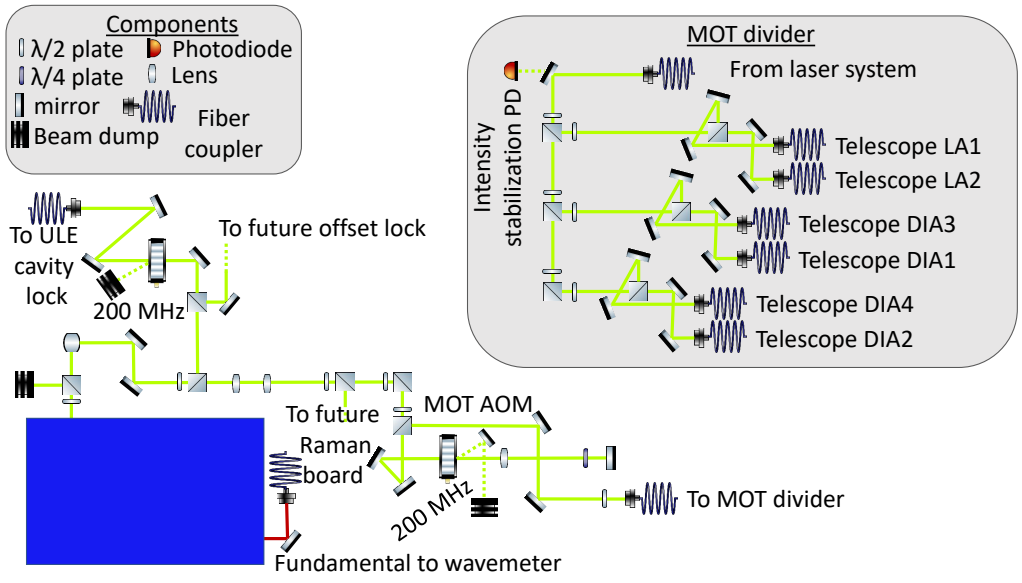

Figure 5.1: Sketch of the laser system used for the green MOT. The same setup is also used for loading and imaging single atoms.

A small amount of the laser power is picked off for locking on the ULE cavity. It is passed through a 200 MHz AOM used for intensity stabilization before the cavity and then coupled into a fiber.

The rest of the laser power not used for in the auxiliary locking branch, usually about 700 mW, is passed through an AOM in a double-pass configuration to fine-tune the frequency, intensity

and apply a broadening to the laser light.[25] The output of the double pass setup is coupled into a fiber and is sent to the MOT divider setup on the experiment table. The intensity in the MOT divider is actively stabilized and the usual maximum power is 350 mW. The divider splits the power into six branches, each of which is send via a fiber to one of the six MOT-telescopes of the 3D-MOT. The divider allows for precise balancing of all beams, the beams propagating along the symmetry axis of the magnetic field coils (LA beams) having half the power of the other four beams (DIA beams). The power in each diagonal beam is usually about 23 mW, in the LA beams about 11.5 mW. The fibers connecting the MOT divider setup with the telescopes are single-mode fibers, the polarization of the laser light is set to σ using a three-paddle in-line fiber polarizers (not shown) per fiber.

To directly load atoms into a green 3D-MOT from the beams of atoms generated by the 2D-MOT and subsequently compress and further cool the atoms, precise control over the frequency, intensity and frequency modulation of the employed laser light is needed. For initially capturing atoms, the spectrum of the laser light is artificially broadened during loading. To cool the atoms and compress the MOT, the broadening is reduced, the frequency tuned closer to resonance and the intensity ramped down. To be able to control all these parameters from the experiment control software, the electronic setup shown in figure 5.2 is used.

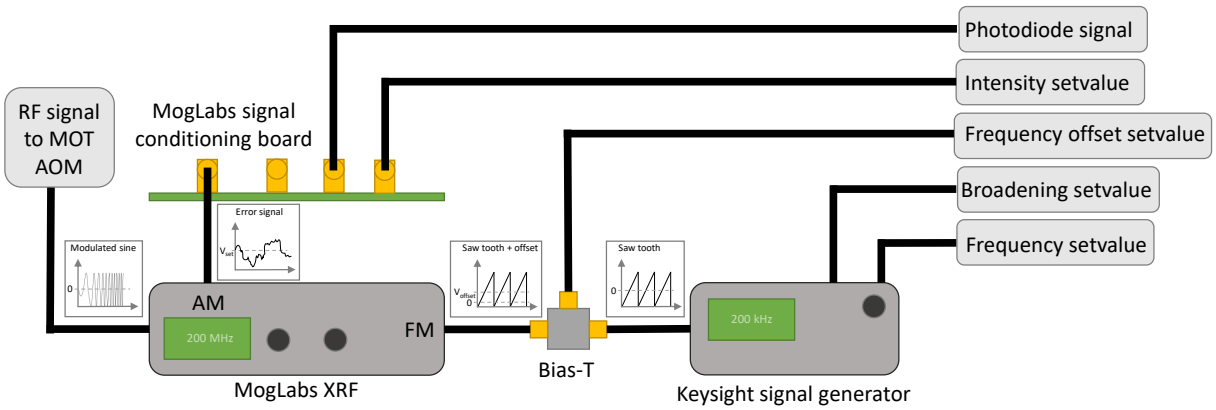

Figure 5.2: Electronic setup to control the frequency, intensity and broadening of the laser light used for the 3D-MOT.

The primary frequency source is a DDS-based MogLabs XRF running at about 200 MHz. Its amplitude modulation input (AM) is used for intensity stabilization together with a MogLabs

[25] The laser system is already under reconstruction during the time of writing this thesis to be able to also perform Raman sideband cooling. For example the cube with the reflection port labeled to future Raman board has been exchanged with a switch EOM to be able to supply the full laser power to the Raman laser system.

signal conditioning board, the corresponding photodiode is the one in the MOT divider setup shown in 5.1. The intensity set value is controlled via an analog signal from the experiment control software. The frequency modulation input (FM) of the MogLabs is used to control the frequency offset from the devices center frequency via an analog signal also sourced from the experiment control system and to apply the broadening necessary to catch atoms from the 2D MOT in the initial loading stage of the 3D MOT via a saw tooth modulation, both signals being combined via a bias-T. The saw tooth is sourced from a Keysight arbitrary waveform generator. Its frequency is set via TCPIP at the beginning of each experimental shot, its modulation input is used to control the amplitude of the saw tooth modulation thus controlling the strength of broadening applied to the laser light which is also controlled via an analog signal from the experiment control.

5.2 Optical setup

The 3D MOT is setup in a six beam configuration. Although in a retro-reflected configuration it would be possible to reach higher intensities for loading, the complex optical setups the beam has to pass through made this configuration unfeasible in practice as the polarization of the reflected beam can not be controlled precisely. To set the polarization correctly in practice, it is measured right in front of the glass cell without any further optical elements in the path. The setup for all six beams is illustrated in figure 5.3.
Atoms are expelled by a dispenser installed in the 2D MOT glass cell. The atoms are trapped by a 2D MOT formed by two retro-reflected beams shaped to a cylindrical shape with the aid of a cylindrical telescope. As the usual power in the 2D MOT is about 1000 mW and no fiber could be used, the beams is routed free space to the beamsplitter before the two branches. As the laser for the setup is located on a separate staging on the experiment table, the alignment of the 2D MOT beams is only stable over long periods of time when the beam path is actively stabilized using a TEM Aligna. The atom number in the 3D MOT crucially depends on precise 2D MOT alignment, as the atoms need to fall through a differential pumping stage to reach the area of the 3D MOT in the science glass cell. As the pumping stage is aligned with gravity, no extra pushing beam is employed. The angle of the diagonal beams deviate from the optimal angle of 90° because the high-resolution microscope objectives block that path. They have an angle of about 57° from the horizontal plane. The beam diameter of the six beams is about 12 mm clipped to size by apertures located on each telescope.
Co-propagating with the two MOT beams that propagate along the symmetry axis of the magnetic field coils is the pathway for imaging the 3D MOT through absorption imaging.

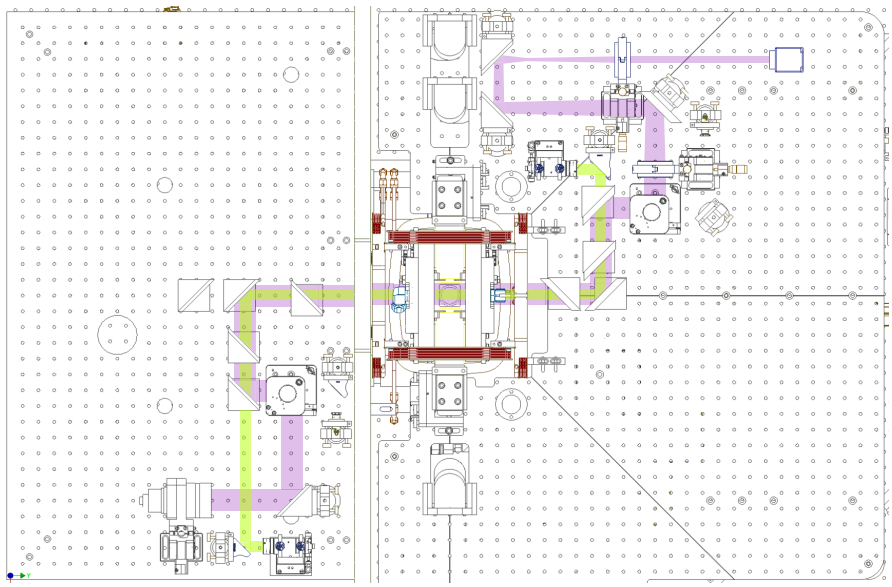

(a)

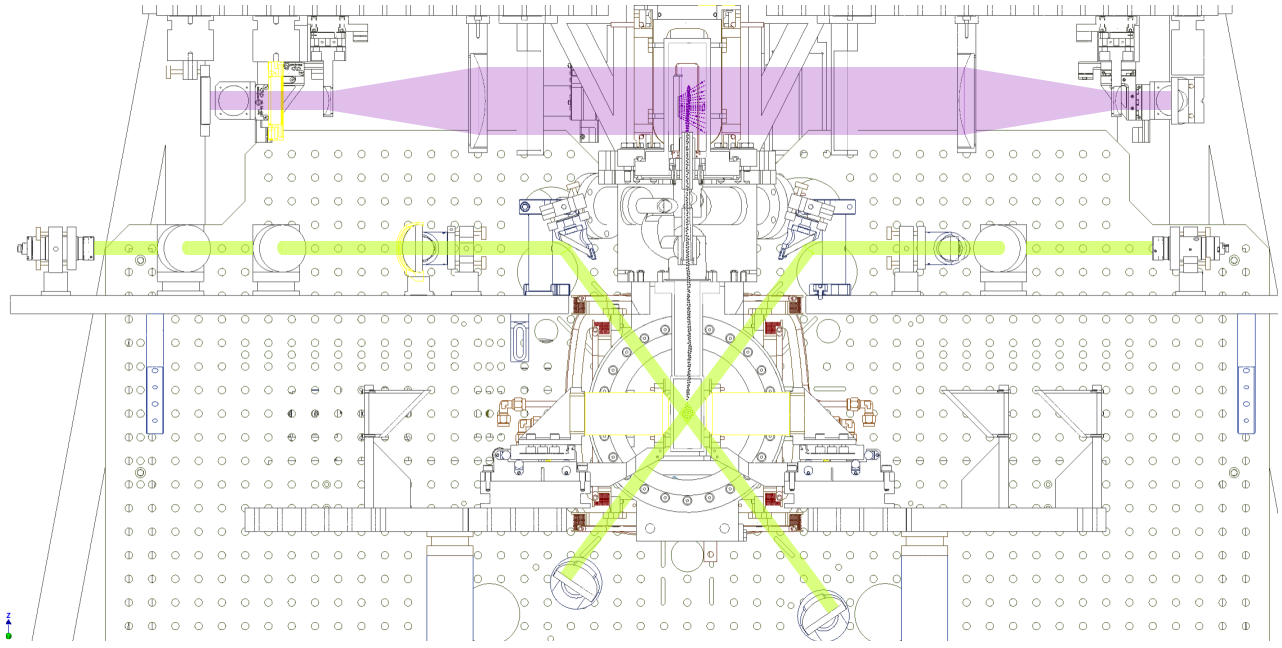

(b)

Figure 5.3: Optics layout for the six beam 3D MOT. (a) shows the two so called LA beams and the layout for the absorption imaging of the MOT, (b) shows the layout of the four DIA beams as well as the 2D MOT, not shown are the telescopes of the two DIA beams located on the experiment table, counter-propagating with the two beams coming from the upper horizontal breadboards.

5.3 Performance

Experiment sequence

The experimental sequence for characterization of the 3D MOT is shown in figure 5.4. It consists of an initial loading phase of 3 seconds followed by a two stage compression to increase the density of the MOT and reduce the temperature. With the normal settings the experiment typically loads about 6 million atoms in 3 seconds. For any further experiments the compression stage stays the same, only the loading time is reduced when loading atoms into tweezers.

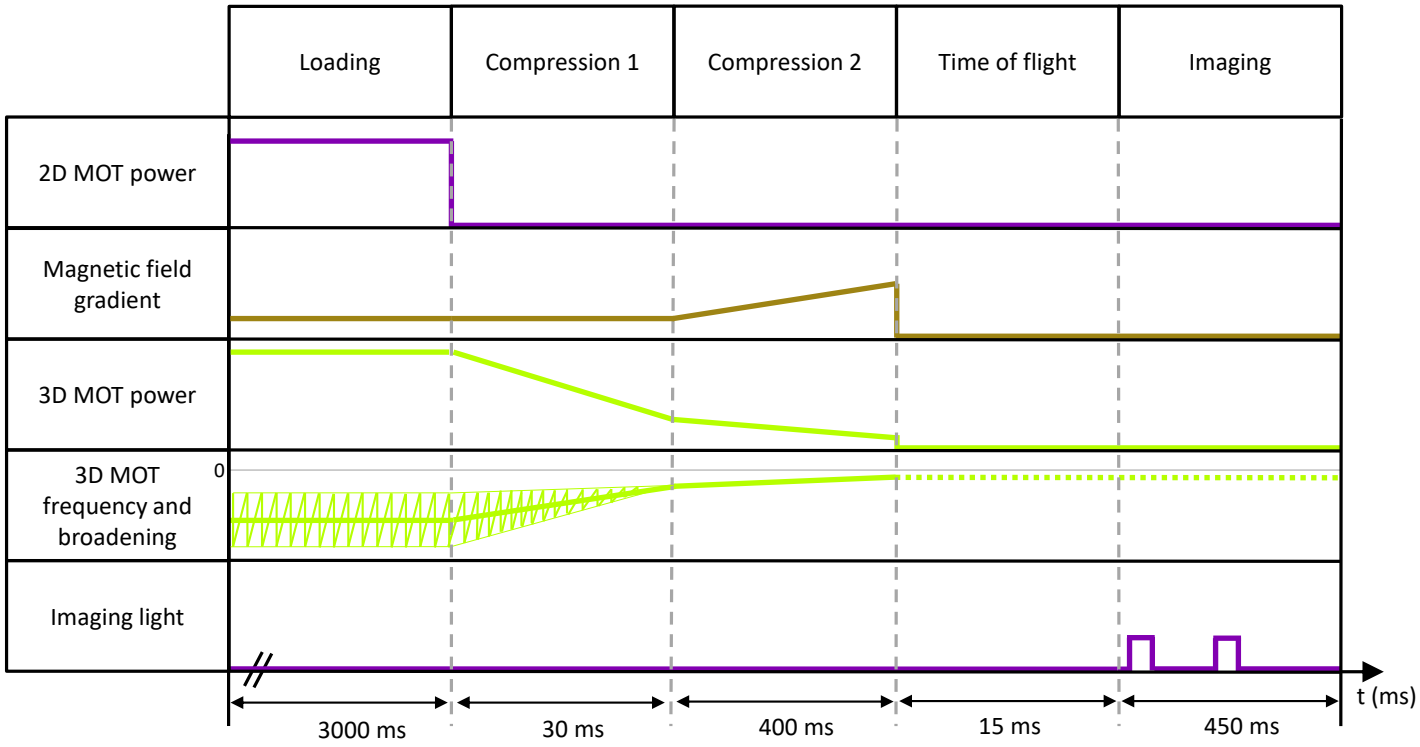

Figure 5.4: The experimental sequence used for the 3D MOT. The 2D MOT is on for an initial loading phase of 3000 ms. During this time the magnetic field gradient is 4.2 G/cm, the power of the 3D MOT beams is at its maximum of about 1100 I_{Sat} and the spectrum is broadened to a -20 dB width of 9 MHz by a saw tooth of frequency 250 kHz at a center frequency of -41 Γ_{556}. After this initial loading step, the 2D MOT is shut off and the broadening is reduced to zero while simultaneously sweeping the center frequency of the comb to -12.7 Γ_{556} and reducing the intensity to 15.3 I_{Sat} in 30 ms. After that the atoms are compressed further by increasing the magnetic field gradient to 5.25 G/cm, reducing the intensity to 0.6 I_{Sat} and sweeping the frequency to -1.3 Γ_{556} in 400 ms. With these settings we load about 6 million atoms in 3 seconds at a temperature of about 15 µK.

The experimental setup is stable on the order of several weeks if the experimental apparatus is not touched. The only significant drift is due to the residual drift of the ULE cavity, influencing the frequency of the laser compared to the transition. To prevent this effect, the center frequency of the AOM in the MOT laser system is scanned regularly and the frequency is optimized on

the temperature of the cloud. This effect can in future be mitigated by using an active drift compensation, but as the drift is only on the order of 50 kHz per week manual optimization every few days was enough for the experiments performed in this thesis.

Loading

Direct loading of a 3D MOT on the intercombination line using an artificially broadened laser has the advantage of not loosing atoms to the meta-table $^3P_0$ and $^3P_2$ states thus requiring no repumping of these states [109].
To optimize the parameters for loading, three combinations of loading parameters are scanned to find the optimum in atom number. The combinations are the comb width versus the center frequency, the intensity versus the modulation frequency and the center frequency versus the magnetic field gradient.
Figure 5.5 shows a scan of the width of the spectral broadening vs the center frequency of the comb.

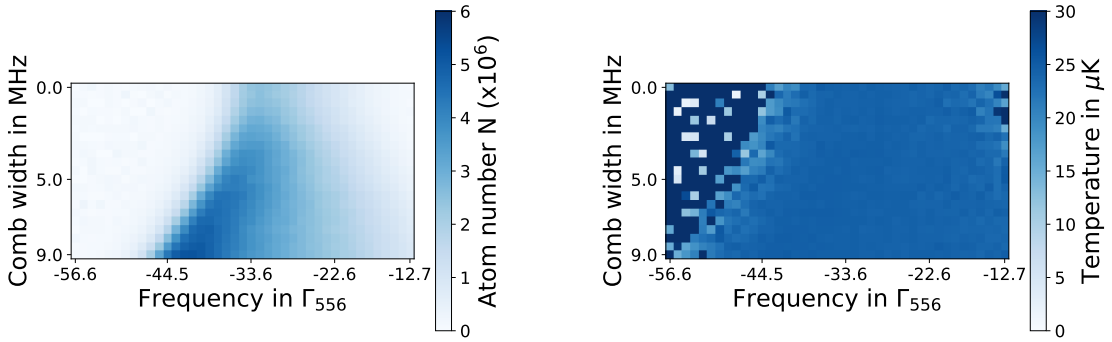

(a) **(b)**

Figure 5.5: (a) Atom number and (b) temperature of the 3D MOT for different broadening comb widths and center frequencies during loading. The atom number shows a clear peak when the width of the frequency comb reaches its maximum value and the center frequency is chosen correctly. As expected the temperature of the final MOT is not influenced by the loading step.

To directly load atoms from a 2D MOT into a 3D MOT on the narrow intercombination transition, it is necessary to broaden the spectrum of the applied laser to address a large set of velocity classes of atoms from the 2D MOT. Thus a larger broadening is able to address more atoms from the 2D MOT until most of the atoms are caught and the atom number in the 3D MOT saturates. To achieve this, the frequency center of the comb has to be carefully chosen to not lead to any spectral overlap into blue-detuned regions that would heat away the atoms. Although one can not change the line width of the employed transition, one can think of the broadened 3D MOT as if the atoms would have an effective line width given by the broadening. In this picture, when the effective line width is $\Gamma_{eff} = 9$ MHz, the optimal detuning from the transition is $0.83\,\Gamma_{\text{eff}}$, a reasonable detuning for a normal MOT.
Figure 5.6 shows a scan of the modulation frequency of the comb vs the intensity in the 3D MOT.

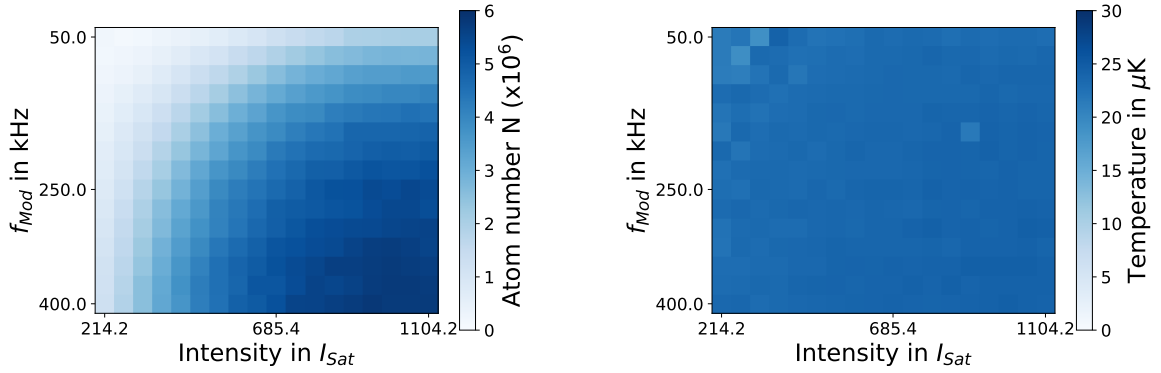

(a) **(b)**

Figure 5.6: (a) Atom number and (b) temperature of the 3D MOT for different modulation frequencies and intensities during loading. The atom number saturates for high intensities and large spacing indicating that all atoms from the 2D MOT are captured in the 3D MOT. As expected the temperature of the final MOT is not influenced by the loading step.

The purpose of this scan is to assess whether the above picture of artificially broadened line holds, as this picture is only true if the spectrum of the frequency comb of the laser light convoluted with the power broadened line width of each spectral component lead to a spectrum as seen by the atoms without any gaps. Thus the spacing of the frequency components in the comb, so the frequency of the saw tooth modulation, has to be chosen in combination with the available laser power to lead to a homogeneous broadening. Eventually the atom number will saturate when all atoms from the 2D MOT are caught, the measurement shows that this is the case for our setup.

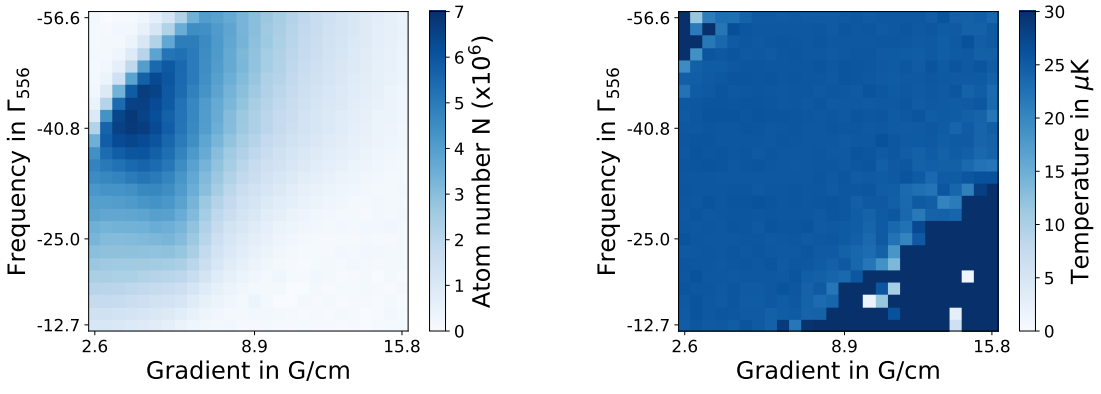

(a) **(b)**

Figure 5.7: (a) Atom number and (b) temperature of the 3D MOT for different magnetic field gradients and center frequencies during loading. The atom number shows a clear peak. As expected the temperature of the final MOT is not influenced by the loading step.

Figure 5.7 shows a scan of the parameter combination of center frequency and magnetic field gradient. As the last parameter optimized for loading, the magnetic field gradient employed needs to be large enough to have a sufficient capture velocity yet small enough to have a large trapping volume. For the optimal detuning of the laser, the magnetic field gradient shows a clear

optimum at 4.2 G/cm.
With the optimized set of loading parameters, the 3D-MOT typically has a loading rate of 1.6 million atoms per second 5.8.

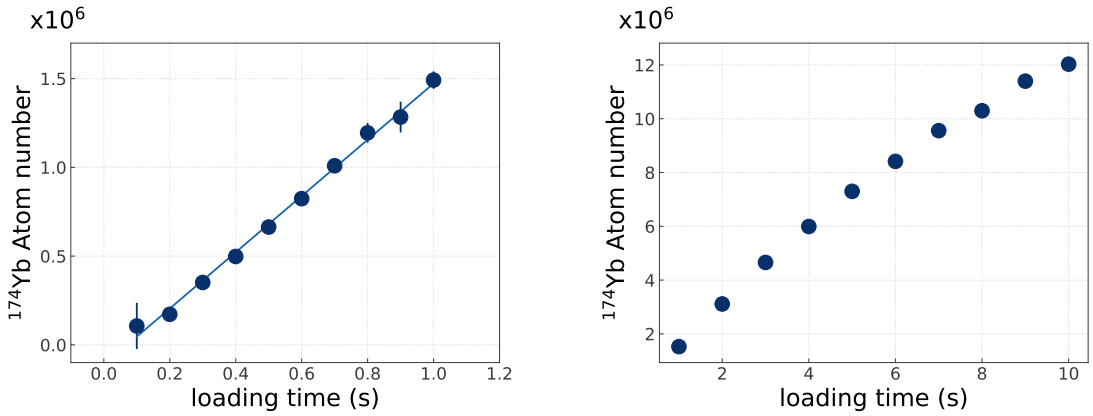

Figure 5.8: Atom number in the 3D MOT for (a) short and (b) long loading times. A linear fit to the atom numbers at short times gives loading rate of 1.6 million atoms per second.

Compression

After initial loading into the broadened 3D-MOT, the atomic cloud is still too hot and dilute for efficient loading into the optical tweezers, thus the density of the MOT needs to be increased and the temperature reduced. For this purpose the atoms are transferred into a single frequency MOT. This process should be optimized to loose as little of the loaded atoms as possible.
For this step, the broadening of the laser light is reduced to zero in a first compression step while simultaneously sweeping the frequency closer to resonance and reducing the intensity. After this initial step, the density is further increased and the temperature reduced by sweeping the frequency closer to resonance and further reducing the intensity.
A scan of final intensity and frequency of the compression can be seen in figure 5.9, the temperature reaching its optimum for an intensity of 0.6 I_{Sat} and a frequency of -1.3 Γ_{556}.
As discussed previously, the other important parameter is the magnetic field gradient. Figure 5.10 shows a scan of this parameter together with the detuning, showing an optimum at 5.25 G/cm.
With this optimized compression, the MOT reaches a final temperature of about 15 µK as extracted from a time of flight measurement in figure 5.11 with the fit of the form

$$\sigma_i(t) = \sqrt{\sigma_0^2 + \frac{k_B T}{m} * t^2} \tag{5.1}$$

The data points for small times are not well described by this formula, most likely due to the

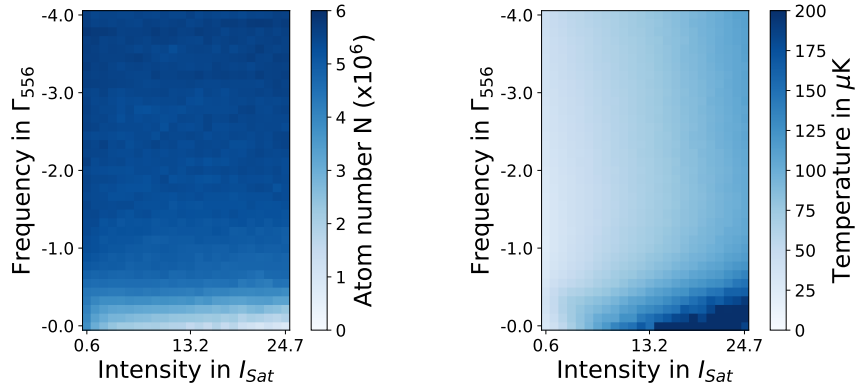

Figure 5.9: (a) Atom number and (b) temperature of the 3D MOT for different end detunings and end intensities.

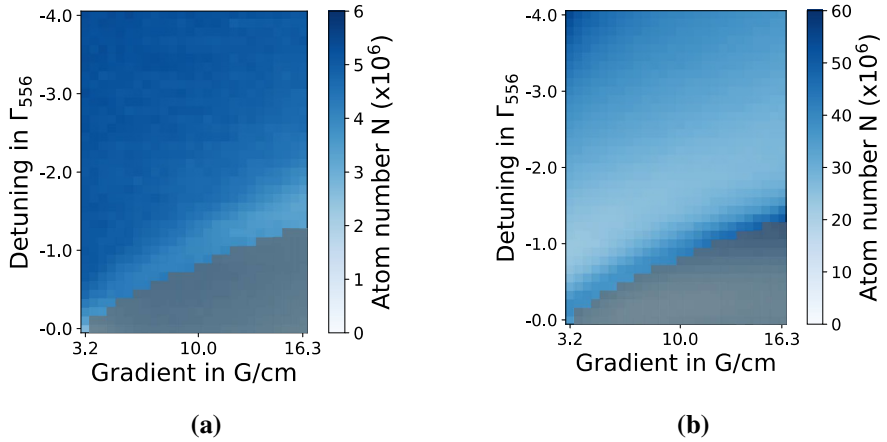

Figure 5.10: (a) Atom number and (b) temperature of the 3D MOT for different end detunings and gradients. The atom number at large gradients and small detunings (greyed out) is an artifact of the measurement, as from the absorption image it is clear that the atoms are not trapped in the 3D MOT anymore and are being heated away.

complex behavior of the compressed MOT because of its high density and the near-resonant light. One possible explanation could be photon rescattering in the dense cloud leading to an additional repulsive force.

The compressed 3D MOT has a life time of about 4 seconds, being limited by losses in the dense trap. One simple exponential decay might not capture the complex behavior and the data can be describes using the formula [110]

$$N = \frac{N_0 \gamma}{N_0 \beta (e^{\gamma t} - 1) + \gamma e^{\gamma t}} \tag{5.2}$$

where N_0 is the initial atom number, γ is the life time and β is the loss rate.

The loss can be explained by long-ranged dipole interactions scaling like r^{-3} between ground and excited state atoms that coexist in the MOT [111, 112]. These interactions can either lead to

state-changing collisions where two atoms gain enough kinetic energy to escape the MOT when they leave on a lower molecular potential or radiative escape where two atoms decay at small inter-nuclear distance and the energy gained from the dipole interaction potential is large enough to lead to loss. The fit leads to a life time of $4 \pm 0.2 s$ and a loss rate of $3.73 \pm 0.37\, 10^{-8} 1/s$.
A similar study of the 3D MOT in the same vacuum chamber was done in [113]. In this study the life time of the uncompressed MOT for ^{174}Yb was measured to be about 300 s. For the fit of the compressed MOT, the lifetime was kept fixed at this value and a loss rate was measured to be $10.0 \pm 0.3\, 10^{-8} 1/s$, about three times larger than the loss rate measured in this thesis. The author notes that for the data presented in this thesis, fixing the life time to 300 s for the fit leads to a loss rate of $10.7 \pm 0.4\, 10^{-8} 1/s$, agreeing with the measurement in [113], but the data is then not well described by the fit. As the leading cause for atom loss in the uncompressed MOT is collision with residual background gas and the vacuum chamber was not opened since the before mentioned measurements, it is safe to assume that the life time of the uncompressed MOT should be equal or greater than 300 s. A study of this is left for future work.
The author notes that after the density has been lowered by loss, the remaining atoms in the 3D MOT live for several minutes and can be observed on the florescence camera later also used for imaging single atoms and manipulated using the compensation coils.

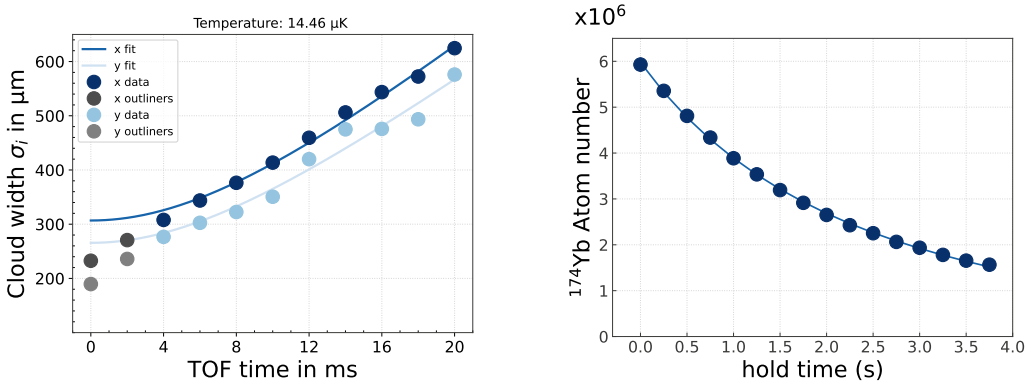

(a) **(b)**

Figure 5.11: (a) Time of flight measurement of the 3D MOT to extract the temperature. The fit is done with the function 5.1 to extract the temperature, the gray data points are excluded from the fit. The averaged temperature over both radial directions is about 15 µK. (b) Life time of the compressed MOT. The fit results in a life time of about 4 seconds.

6 Trapping single atoms

This chapter illustrates the analysis of the machine performance for trapping and imaging single bosonic ^{174}Yb atoms in 532 nm tweezers generated with an acousto-optic deflector as well as the experiments conducted to characterize the traps using single atoms. After giving an detailed explanation on the image processing needed for identification of a single atom with high-fidelity, it characterizes the imaging performance of the machine. With the capability to convert experimental images into an occupation matrix with high fidelity, it shows first experiments on performing optimized parity projection, determining the temperature of the atoms in the trap, analyses the life time of the atoms in the tweezers and shows the results of a trap modulation experiment to determine the trap frequencies. The experimental work described in this chapter was conducted together with N. Pintul, the data was analyzed by the author in close contact with N. Pintul. All work was performed under the supervision of C. Becker and K. Sengstock.

General experimental sequence

The general experimental sequence for all experiments presented in this chapter is illustrated in figure 6.1. After loading and compressing the 3D MOT as described in chapter 5, the gradient applied by the main coils is increased from 5.25 G/cm to 8.7 G/cm and the field of the compensation coils in all three directions are ramped to overlap the cMOT with the position of the tweezers, also performed in other groups [106]. The author notes that no adverse effects could be observed from this process except the time loss of 35 ms, nonetheless this step would be obsolete if the position of the tweezers and the 3D MOT would be overlapped physically [114]. This step was not conducted during this thesis as precise alignment of the objective poses quite a challenge and is time-consuming.

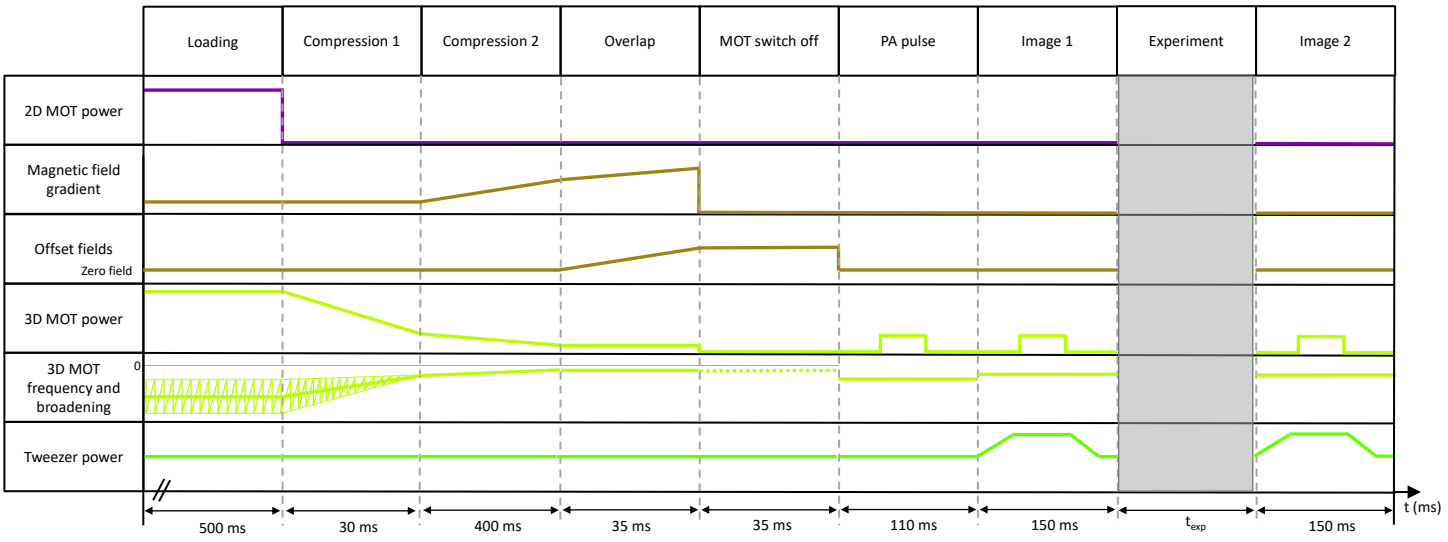

Figure 6.1: General experimental cycle used for all experiments. Time axis not to scale.

6.1 Imaging fidelity and loss probability

To gain any experimental information, the first step in every experimental shot after loading the tweezers with single atoms is taking a first image. The imaging parameters should be chosen in a way to maximize the fidelity of correctly identifying an occupied site while minimizing the loss of atoms during imaging.

The following analysis takes an in-depth look at the influence of the detuning and intensity of the imaging light on the two parameters, the tweezer depth during imaging is kept fix at 8.2 mW per tweezer leading to a trap depth of 0.73 mK[26] and the imaging duration is kept fixed at 100 ms. In the current setup, no extra imaging beams are employed and the same 6 beams used for the 3D MOT are used for imaging still red-detuned from the transition to employ Doppler-cooling while imaging. To analyze the imaging fidelity a series of 60 experimental shots at the same detuning and intensity are taken, each shot containing three images with atoms and one reference image. The goal of this analysis is to find the optimal imaging parameters, that need to trade off imaging fidelity and loss probability due to scattering of photons.

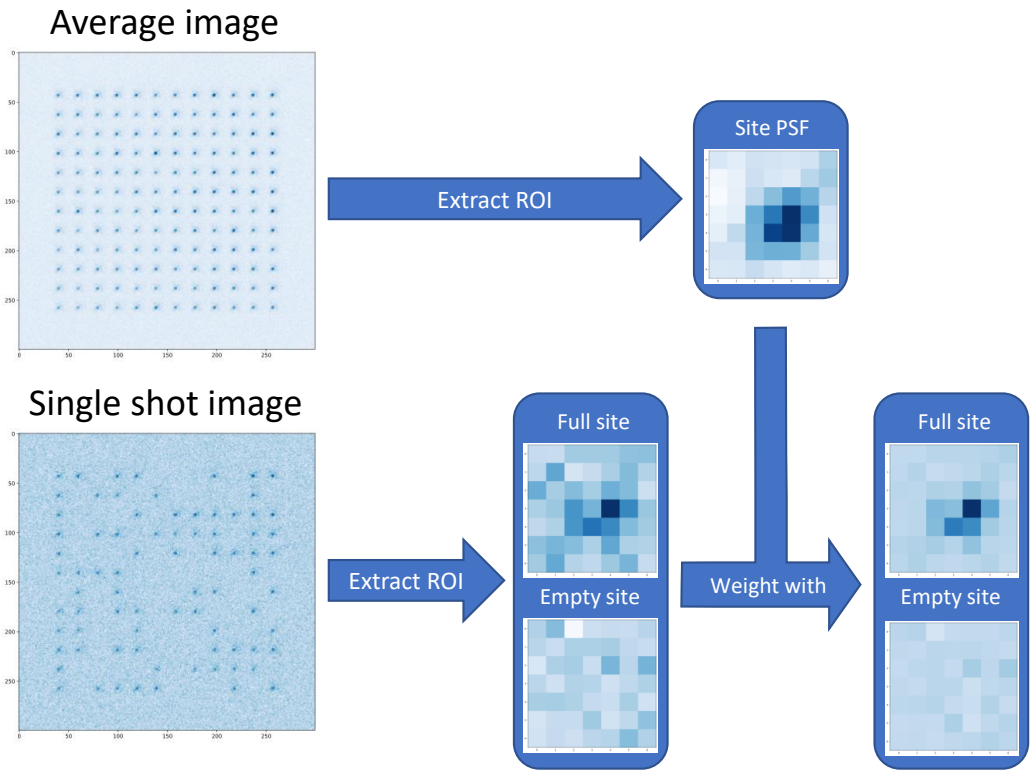

Figure 6.2: The steps of image processing to get to the number of counts per site. First the fluorescence images from all 60 experimental runs at the same imaging parameters are averaged. From the average image all positions of tweezer sites as well as a site specific point spread function (PSF) are extracted for weighting the single shot images to suppress noise outside of the region where scattered photons should occur on the camera. The counts in the selected region of interest around each possible tweezer position are summed up after weighting leading to a count per site. The spacing between the atoms is 5 µm.

[26]The trap depth is calculated from the power of 8.2 mW and the size of the tweezer in radial and axial direction as presented in section 4.3.

Image processing

To reduce the effects of the stray light form the effects described above, first the reference image is subtracted from the atom image. After determining the position of each tweezer site from an average image of 60 shots, a region of interest (ROI) is extracted around every site. This ROI is then weighted with the experimentally measured averaged point spread function of the corresponding site to suppress noise. After that, the counts in every site are summed up. The process is visualized in figure 6.2.

Model to determine the imaging infidelity

After the counts of photons per tweezer site are extracted from the image, the results is displayed into a histogram. To determine the imaging fidelity and the optimal threshold to distinguish an empty site from a filled site the histogram is fitted with a double gaussian distribution [58].

$$N(x) = N_0 * \exp((x-x_0)^2/2\sigma_0) + N_1 * \exp((x-x_1)^2/2\sigma_1) = \text{Gaussian}_0(x) + \text{Gaussian}_1(\text{x})$$

Although the process of recording photons from an atom should inherently be poissonian, the average number of photons collected per site differs, most likely because of incomplete homogenization of the array and thus varying light shifts and photon scattering rates per site as can be seen from the histogram of the intensity per site of the average image 6.3. As the histogram of all tweezer sites is now an overlap of several poisson distributions, it is best fit with a gaussian.
From the fit to both peaks of the histogram it is now possible to define the false positives as

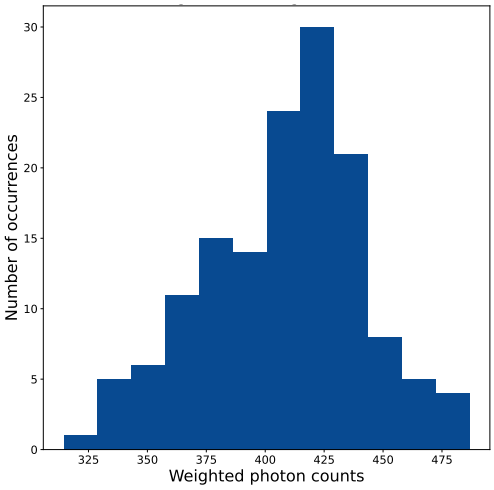

Figure 6.3: Average intensity per tweezer site. The wide distribution might be explained by residual light shifts and thus varying photon scattering rates per site.

$$P^{\text{FalsePositive}} = \int_{-\text{inf}}^{T} \text{Gausian}_0(x)\, dx$$

and the false negatives as

$$P^{\text{FalseNegative}} = \int_{T}^{+\text{inf}} \text{Gausian}_1(x)\, dx$$

with the classification threshold T. These integrals are shown in figure 6.4 for more clarity. The threshold is optimized to minimize the classification infidelity

$$\widetilde{F} = \frac{P^{\text{FalsePositive}} + P^{\text{FalseNegative}}}{\int N(x)\, dx}.$$

The imaging fidelity is then defined as

$$F = 1 - \widetilde{F}$$

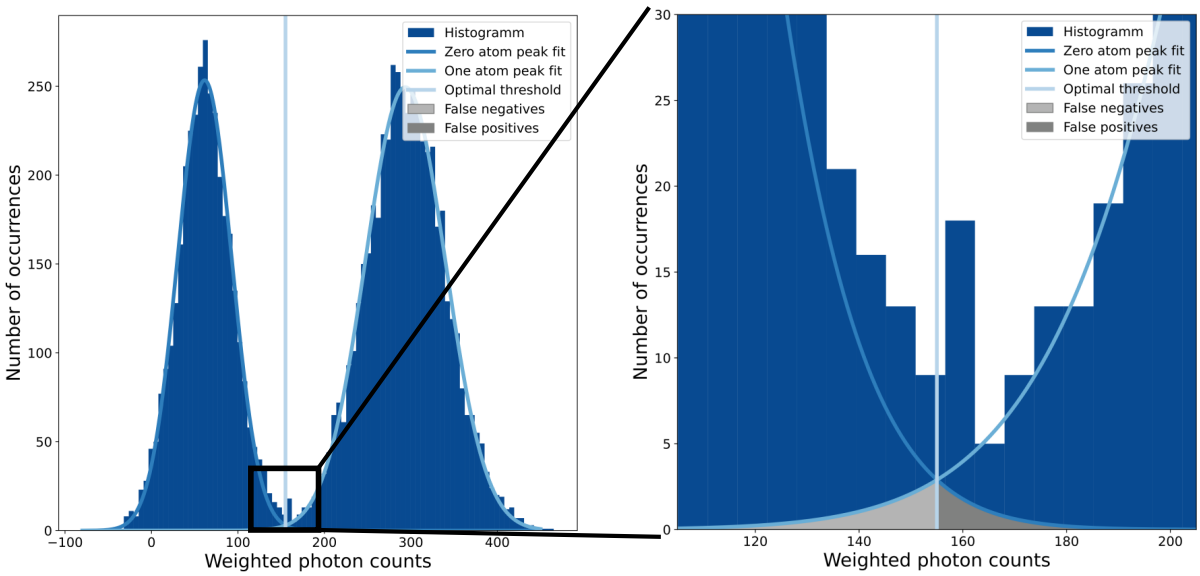

Figure 6.4: Histogram with fit of double gaussian function. From the fit to both peaks of the histogram and a chosen threshold it is possible to define the false positives and false negatives in classification of a site. The threshold is chosen to minimize both classification errors.

With the optimized threshold it is now possible to convert the image taken to an occupation matrix with high characterization fidelity 6.5. This occupation matrix is the basis for all further analysis.

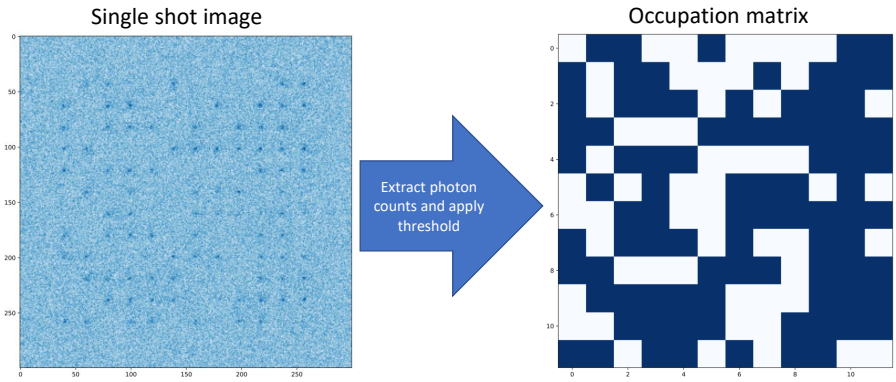

Figure 6.5: Conversion process of a single shot fluorescence image to an occupation matrix. If the counts are above the chosen threshold, the site is classified as filled, otherwise it is classified as empty.

Calculation of imaging loss

With the threshold it is now possible to reliably classify the occupation of a given site and it is straight forward to calculate the loss while imaging as the difference between two successively taken images as seen in figure 6.6. The images are separated by a 100 ms wait time for camera readout.

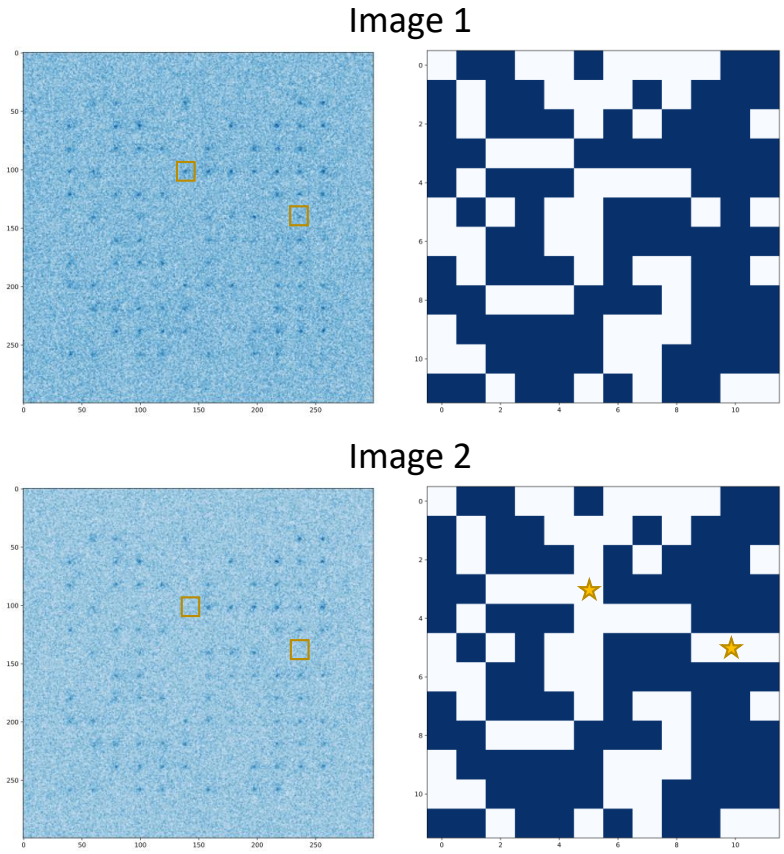

Figure 6.6: Loss between two successively taken images. The fluorescence images as well as the occupation matrices are shown. The yellow squares indicate the sites where an initially loaded atom got lost during imaging. The lost atoms are indicated by a star in the occupation matrix of the second image.

Optimal parameters

The analysis procedure described above is repeated for wide range of intensities and detunings to analyze the imaging performance and find the optimal parameters. The results of this analysis can be seen in figure 6.7. There is a wide range of combinations of intensities and detunings that lead to a low loss imaging on the order of about 1 % with reasonable detection infidelities in the range of 0.1 % to 0.001 %. From the analysis it is clear that a higher detection fidelity also leads to higher loss because of the larger photon scattering rate. Depending on the experiments performed, a lower detection infidelity might be traded for a higher loss rate and vise versa.

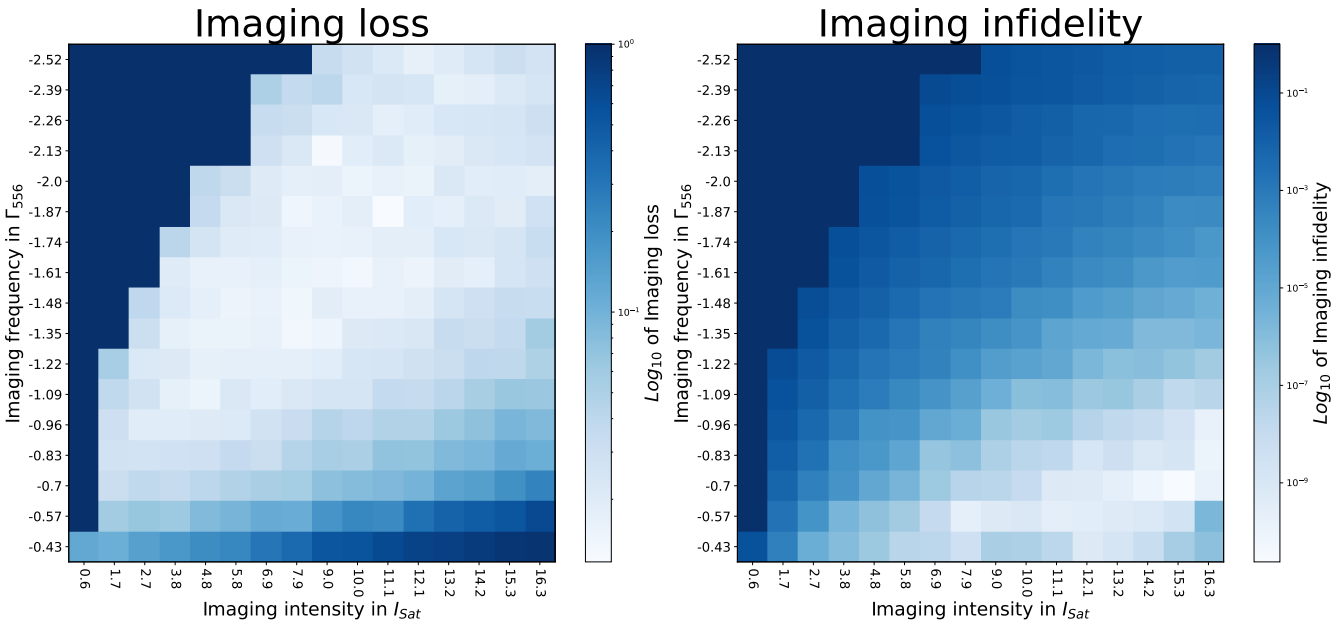

Figure 6.7: Imaging loss and imaging fidelity for different intensities and detuning plotted as log_{10} of the corresponding quantities. In the dark blue area with an imaging infidelity of 100 % no discrimination of an occupied from an unoccupied site is possible because of the low photon scattering rate at low intensity and large detunings leading to a histogram with no double peak structure. At moderate detunings and intensities a large area of low-loss imaging parameters can be found. At high intensities and small detunings the loss inceases because of large scattering and thus heating rates. The imaging infidelity increases in this area as the lost atoms scatter photons for only a part of the imaging time and their signal accumulates between the zero and one atom peak in the histogram.

As an loss-optimal working point for imaging, the combination of an imaging intensity of 11.1 I_{Sat} and a detuning of -1.87 Γ_{556} is identified under the current experimental conditions[27]. This parameter set leads to an imaging fidelity of 99.862 % and a loss of $1.2^{+1.6}_{-1.2}$ %. It is noteworthy that the low loss can only be achieved when the beam balance and polarization of the 6 employed MOT beams is ideal and that experimental imperfections might lead to a loss as high as 10 % at the same detuning and intensity.

Comparison of image processing methods

The above analysis works with a constant region of interest size of 7 pixels and subtraction of the reference image and weighting with the point spread function. For completeness the influence of these methods on the imaging fidelity is shown in figure 6.8.

Error on imaging fidelity

The author notes that with this analysis method, it is hard to give an error on the imaging fidelities presented above. The easiest method would be the error on the integrals used to define

[27] The experimental conditions are a tweezer depth of 0.73 mK and a Lamb-Dicke parameter of 0.2 in radial and 0.7 in axial direction.

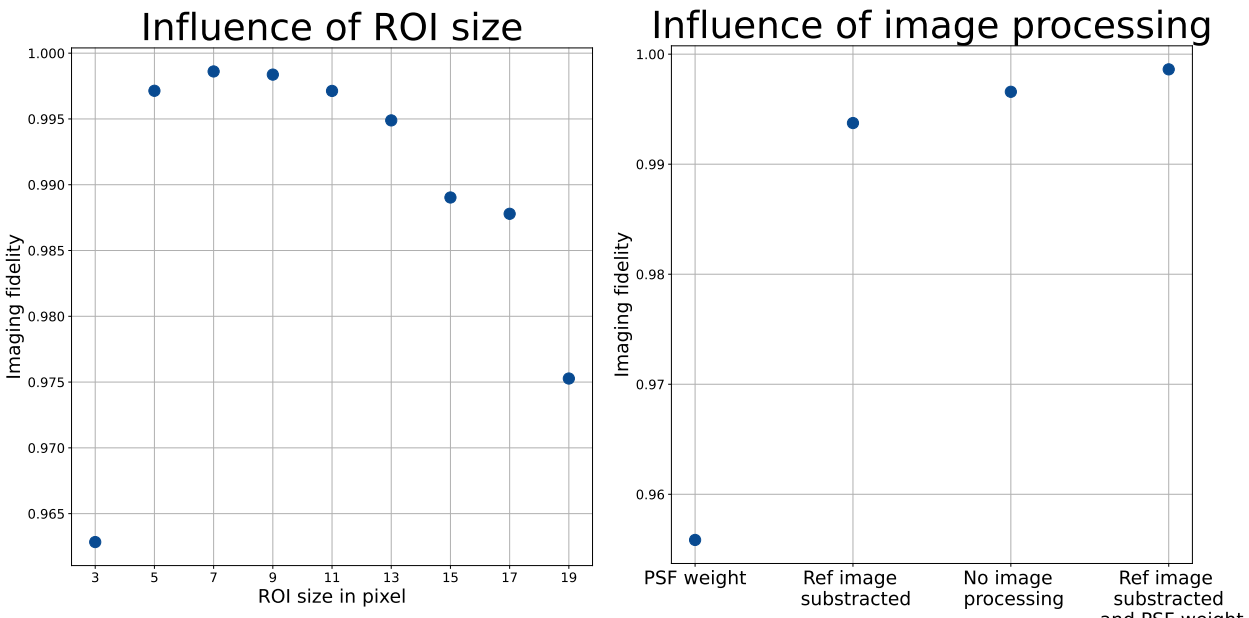

Figure 6.8: (a) Influence of ROI size on imaging fidelity at 11.1 I_{sat} and a detuning of -1.87 Γ_{556}. The fidelity shows a clear peak when it is large enough to catch the whole point spread function of the atom trapped in a tweezer. As soon as this point is reached at an edge length of 7 pixels, the imaging fidelity decreases because the region of interest accompanies pixels without an atomic signal but added noise. (b) Comparison of different image processing methods at 11.1 I_{sat} and a detuning of -1.87 Γ_{556}. Only weighting with the point spread function gives the worst performance, as the point spread function calculated without subtraction of the reference image includes added noise. It is noteworthy that the image processing steps only lead to an increase from 99.658 to 99.862 % under these imaging conditions.

the false positive and false negative rates from the uncertainties on the fit parameters of the two gaussian functions used to fit the histogram. In practice this error is smaller than the machine precision for calculations.

Another possibility would be the event of events where a site previously identified as unoccupied appears as occupied in the following image, which is shown in figure 6.9. In the current setup this rate is limited by off-resonant Raman scattering to dark states involving a combination of trap and imaging photons, most probably to the states $^3P_0$ or $^3P_2$, as these states do not get repumped currently [67]. For the data set at optimized imaging parameters of 11.1 I_{Sat} and a detuning of -1.87 Γ_{556}, this rate is about 0.17 % of all events, agreeing to the imaging fidelity of 99.862 %.

Alternate methods

The previous analysis assumes that both the probability distributions of both the zero and one atom peak are well described by a gaussian distribution. Other approaches to determine the imaging fidelity use either different probability distributions, for example distributions that include a term for losses during imaging [115, 53], or try to asses the imaging fidelity without as-

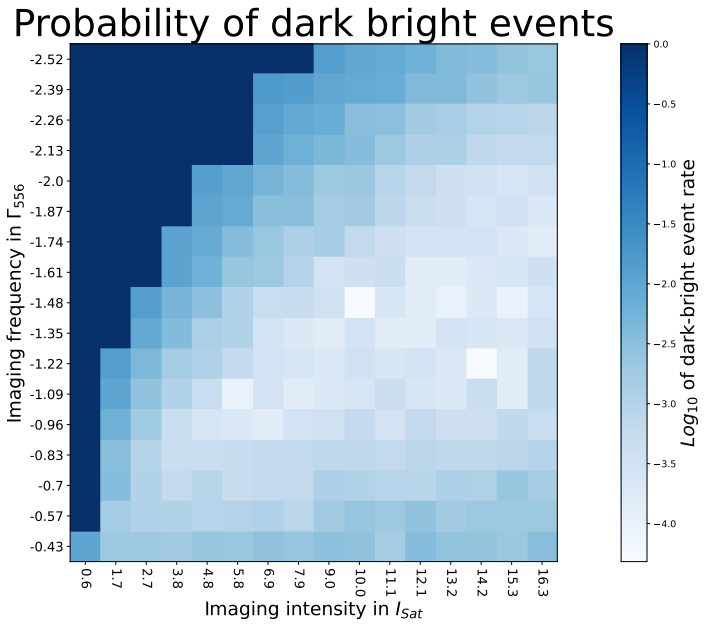

Figure 6.9: Probability of events where a dark site appears bright in the next image. The probability is a combination of classification errors as well as events where an atom spontaneously becomes bright after decaying from a dark state. If the later is ruled out with repumping of the metastable states, the rate might be used as an approximation of the classification error.

sumptions to the probability distribution by optimizing the parameters loss and fidelity through the occurrence of events, that being a site being classified as bright or dark [53].
These methods require a larger data set to be evaluated successfully, as a detailed analysis requires to gain an insight to the probability of seldomly occurring occurring events.
The analysis above is time efficient to scan a large parameter regime to quickly find a good working point for imaging, the other methods might be used in conjunction after this point has been found. A larger dataset would also allow to asses loss and fidelity per site and might be used to further optimize the tweezer potentials. All this is left for future work.

Possible improvements

Although high-fidelity imaging, low-loss imaging is possible with the current setup, there are a number of possible improvements. The first set of improvements assesses the background stray light leading to a narrower zero atom peak in the imaging histograms leading to a reduced need in scattering photons from the atoms for high fidelity classification that could further reduce losses at the same or even improved fidelity. The most obvious is the implementation of a set of extra imaging beams [66, 54] from an angle that reduces scattering of light from surfaces into the objective. The most promising improvement is to reduce the fluorescence[28] from the objective housing material when exposed to 532 nm light, for this either painting the inside of the objective black as done by other groups [98] or including a narrower band pass filter for

[28]The light emitted by the objective is not just scattered 532 nm light, but the housing material starts to fluoresce with a broad spectrum that has overlap with the light emitted by the atoms. As this light does not originate in the focus of the objective, a stray light filter with spatial filtering in a focal point could also be used.

filtering out the fluorescence.
The second set of improvements assesses the atoms themselves. Currently the imaging fidelity might be limited by off-resonant scattering to the metastable $^3P_0$ or $^3P_2$ as indicated by figure 6.9, which should be repumped in the future. Also as shown in figure 6.3, a homogenization of the array with feedback from the atoms [58] should lead to a more even photon scattering rate over different sites in the array which in turn should narrow the one atom peak in the histogram and lead to a lower over all photons required to lead to a good separation of peaks in the histogram.

6.2 Loading and photoassociation pulse

The ultimate goal of the first step of the experiment is to trap single atoms. After overlapping the green 3D MOT with the tweezer array, initially several atoms are loaded per tweezer depending on the final density of the MOT. Thus, after initial loading a further step is required to get rid of the extra atoms. This process involves photo-associating (PA) two atoms to a highly excited molecular state, the decay of which leaves both atoms with enough kinetic energy to leave the trap. As this process leads to a pairwise loss of atoms from the traps, this process is often referred to as parity projection as it leaves a trap initially filled with an uneven number of atoms with one single atom left and a trap initially filled with an even number of atoms empty. Because of the statistical nature of the distribution of the number of initial atoms, this process leaves about half of the traps empty.6.10

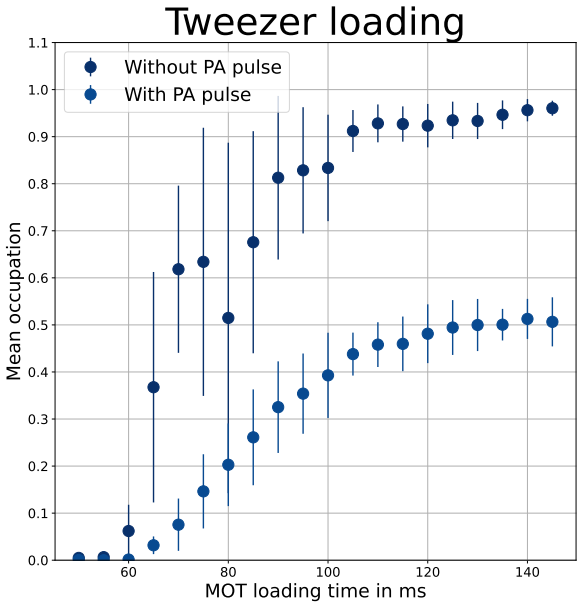

Figure 6.10: Mean occupation of a tweezer array after overlapping it with the green compressed MOT. Without a PA pulse, all sites load at least one but most of the time multiple atoms.

A more careful engineering of the molecular dynamics might lead to the possibility to fine tune the kinetic energy transferred to the atoms leading to a case where the energy is small enough to let only one atom escape leading to enhanced loading. This process involves the excitation of

repulsive molecular potentials with blue detuned light and the complex dynamics ar influenced by the detuning and intensity of the excitation light as well as the trap depth [42, 116, 117, 58]. Also a magnetic field might be employed to imprint a further Zeeman splitting on the states used.

Photoassociation in ^{174}Yb

This chapter presents the results on photoassociation pulses for bosonic ^{174}Yb. The analysis is kept to a fine tuning of frequency, intensity and time of the photoassociation pulse. The author notes that although some time was spend trying to find an area of enhanced loading, no parameters could be found and further study of possible enhanced loading in ^{174}Yb is left for future work.

The success of the photoassociation pulse can directly be observed as the difference in occupation between the first and the second image taken in each experimental shot, when a PA pulse is always on before the first image. In case the PA pulse was only partially successful, the first image will serve as a further photoassociation pulse and remove any remaining doubly occupied sites. The optimal photoassociation pulse parameters can thus be found when the difference in occupation between both images is small and only involves the losses due to imaging.

The normal working point for the photoassociation pulse is a time of 100 ms, an intensity of 6.9 I_{Sat} and a detuning of -4.83 Γ_{556} as indicated by stars in figure 6.11 and 6.12. With this parameter set a loading probability of about 60 % is achieved. Reference [54] reports a loading probability of 49 %, reference [118] reports a loading probability of 61 %.

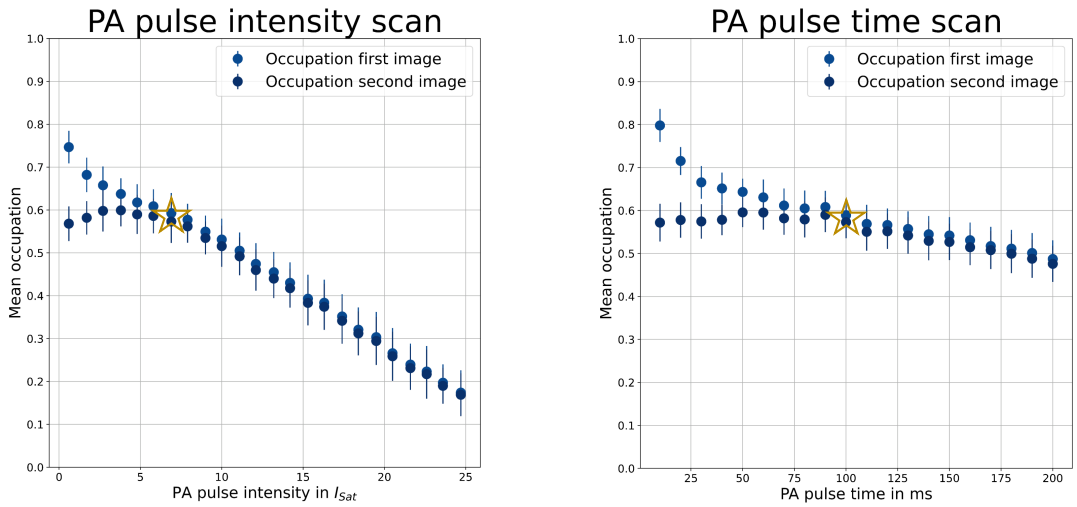

(a) **(b)**

Figure 6.11: Intensity (a) and time (b) scan of the photoassociation pulse at a detuning of -4.83 Γ_{556}. The stars indicate the working point of 100 ms duration and an intensity of 6.9 I_{Sat} where the occupation of two consecutively taken images converges. Longer times and higher intensities lead to a reduction in overall loading probability.

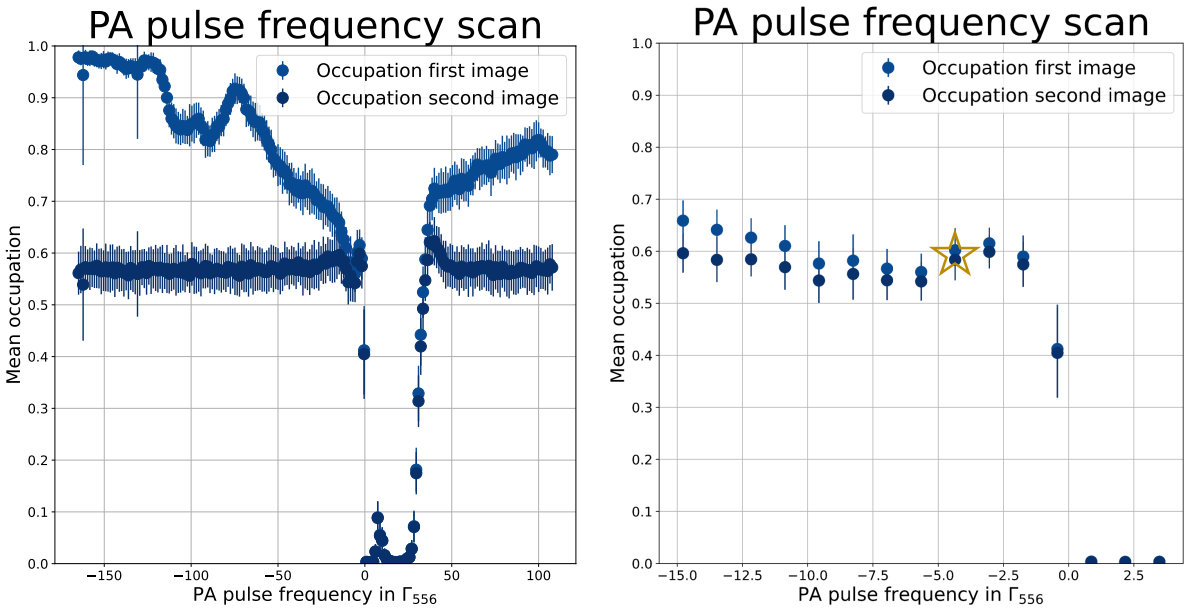

(a) **(b)**

Figure 6.12: (a) Wide frequency scan of the photoassociation pulse, the occupation in the first image shows a complex behavior over the whole range, but loading of single atoms is only possible in the vicinity of the resonance as indicated by the reduced occupation of the second image. (b) Close up of the frequency range around the resonance. For small red detunings the occupation of both images converge indicating that the photoassociation pulse is working. The normal working condition of -4.83 Γ_{556} is indicated by the star. Other parameters of the photoassociation pulse are a time of 100 ms and an intensity of 6.9 I_{Sat}.

6.3 Temperature

To measure the temperature of the atoms in the tweezer, a standard release-recapture experiment is performed [119]. After taking an initial image of the filled array, the tweezers are turned off for a variable time t. After turning the traps back on, a second image is taken from which the recapture probability can be extracted.

Although one might not think of a single atom having a temperature, the atoms in the tweezers have an energy corresponding to the energy level in the tweezer they are populating. For many atoms this energy follows a Maxwell-Boltzmann distribution to which one can assign a temperature. For a single atom, one can think about it in a classical picture as oscillating in the tweezer, having a potential and kinetic energy. When the trap is turned off it will have a velocity associated to it and leave the region of the trap. When the trap is turned back on, an atom might only be recaptured when its kinetic energy is smaller than the potential depth of the trap at the point it has reached during the time the trap was switched off. If this process is repeated many times, one can determine the probability to recapture the atom and from this the temperature of the atoms. To assign a temperature to the experimental data, a Monte-Carlo simulation of this process is performed for different temperatures and the one best fitted to the data is determined. The data presented in figure 6.13 are averaged over all atoms in a 144 site array and 15 experimental shots. The recapture probability from the simulation is normalized to the experimental

imaging loss of about 15 %, probably due to an unbalance and polarization misalignment in the beams used for imaging 6.1 and a smaller detuning of -0.9 Γ_{556} used for imaging in this data set.

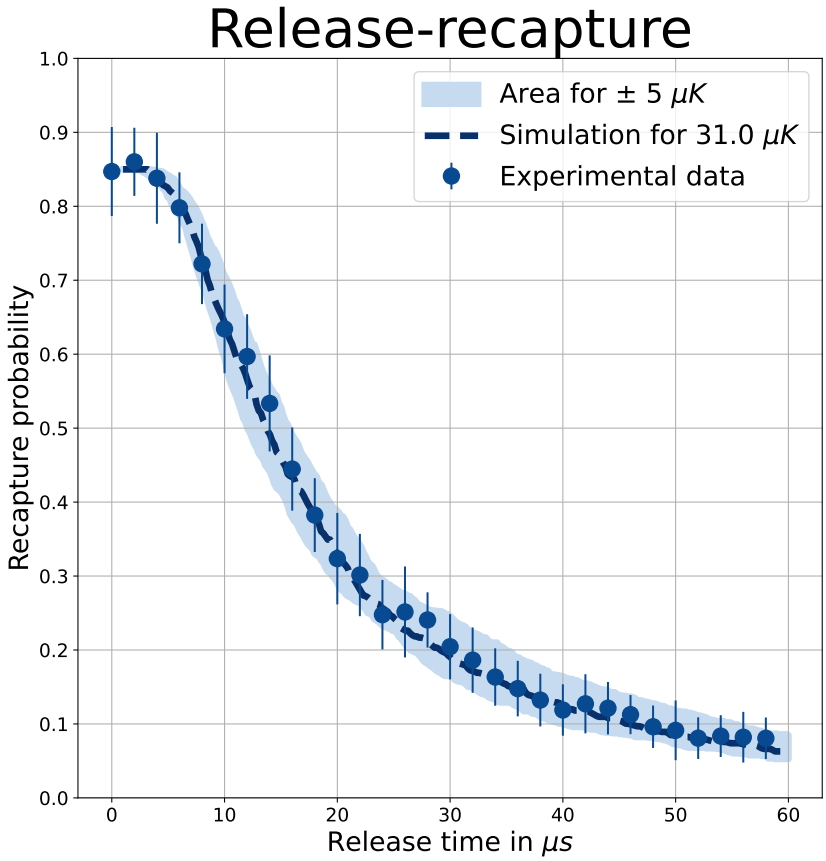

Figure 6.13: Release-recapture experiment to determine the atomic temperature. The recapture probability is normalized to the imaging loss of about 15 %, the high loss and high temperature resulting from a detuning during imaging of -0.9 Γ_{556} with an intensity of 11 I_{Sat}.

The best fitting simulation results in a temperature of $31 \pm 5\,\mu K$, most likely due to the experimental imperfections mentioned before and the small detuning for imaging. At larger detunings, lower temperatures were observed by other groups, reference [54] reports 6.4 µK and reference [118] reports 19.5 µK.
To further reduce the temperature, the experiment will employ Raman sideband cooling in the future [58].

6.4 Life time

A crucial quantity for all future experiments is the life time of the atoms in the traps.
The life time of the atoms in the tweezers is assessed under two different conditions. First, the life time while just holding the atoms with all beams but the traps turned off and second, the life time while keeping the imaging beams on during holding. Both cases are studied for different powers per tweezer.

Dark life time

For analysis of the dark life time, all beams except the tweezers are turned off after the initial image to identify filled sites. After that, the tweezer power is ramped to its holding value in 50 ms and the atoms are held for a variable time t.

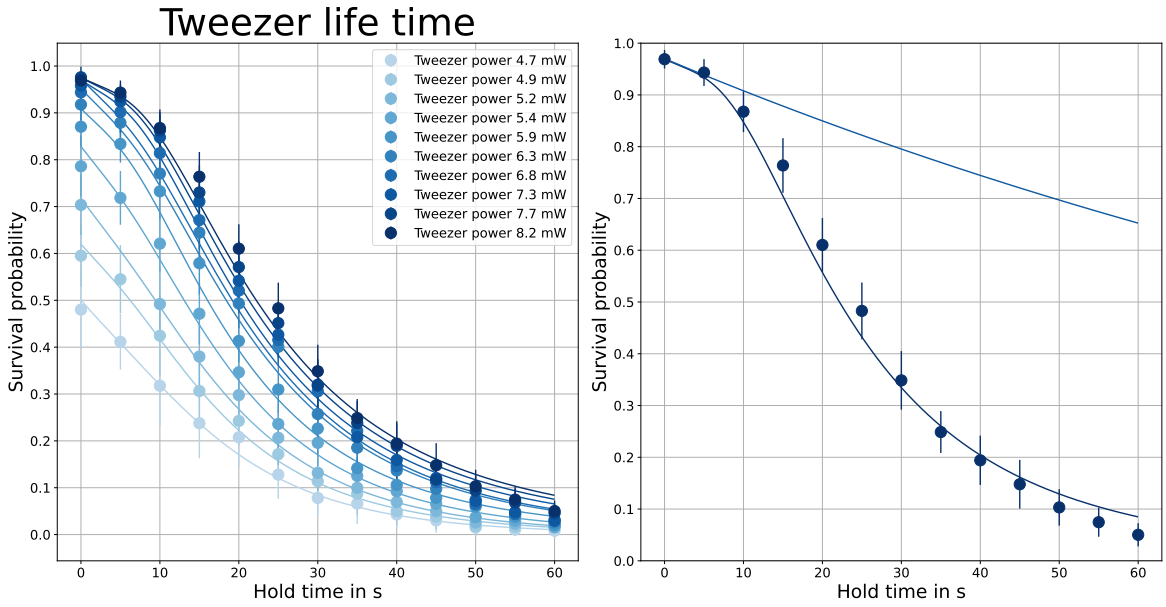

(a) **(b)**

Figure 6.14: (a) Survival probability of the atoms in tweezers for different tweezer power while holding the atoms. The lines are a fit with 6.3. (b) Life time of the atoms in the deepest tweezers. The dark blue curve is the fit with function 6.3 to the data points, the lighter blue curve is a plot for clarity of the collisional part of the life time following equation 6.1 with a τ of 134 s.

To analyze the data, the model presented in [120] is employed. The model is a combination of collisions with residual background atoms in the vacuum chamber with decay time τ

$$P_{\text{coll}}(t) = e^{-\frac{t}{\tau}} \tag{6.1}$$

and a heating term that is governed by a linear increase of temperature in time

$$P_{\text{heat}}(t) = 1 - \exp\left(-\frac{U_0}{k_B(T_0+\alpha t)}\right)\left(1+\frac{U_0}{k_B(T_0+\alpha t)}+\frac{U_0^2}{2k_B^2(T_0+\alpha t)^2}\right) \tag{6.2}$$

where U_0 is the trap depth, T_0 is the initial temperature of the atom and α is the heating rate. To capture the experimental losses even at zero hold time, a initial loss P_0 is introduced as an extra term..
The total probability for an atom to survive a time t is then

$$P(t) = P_0 * P_{\text{coll}}(t) * P_{\text{heat}}(t). \tag{6.3}$$

For the fit of the data with this model 6.14 as seen in figure 6.14 (a), the temperature is fixed to the temperature measured in 6.3 and the trap depth to the value calculated from the power and the tweezer waist.
The life time extracted from this fit is a measure for how well the vacuum inside the science glass cell is and the heating rate gives insight to technical limitations of the experimental setup. As can be seen in figure 6.15 both the life time and the heating rate increase with increasing tweezer power. For the highest tweezer power of 8.2 mW, the life time of an atom in the tweezer is $134 \pm 108\,s$ and a heating rate of $9.2 \pm 1.4\,\mu K/s$. To illustrate the meaning of the life time in the above plots, figure 6.14 (b) shows the collisional life time part of equation 6.3 as well as the whole function for the deepest tweezers. It is visible that the long lifetimes are due to the slow decline in population in the beginning before the heating term takes over. This part of the function is only represented by the first two data points, an explanation for the large fit error.

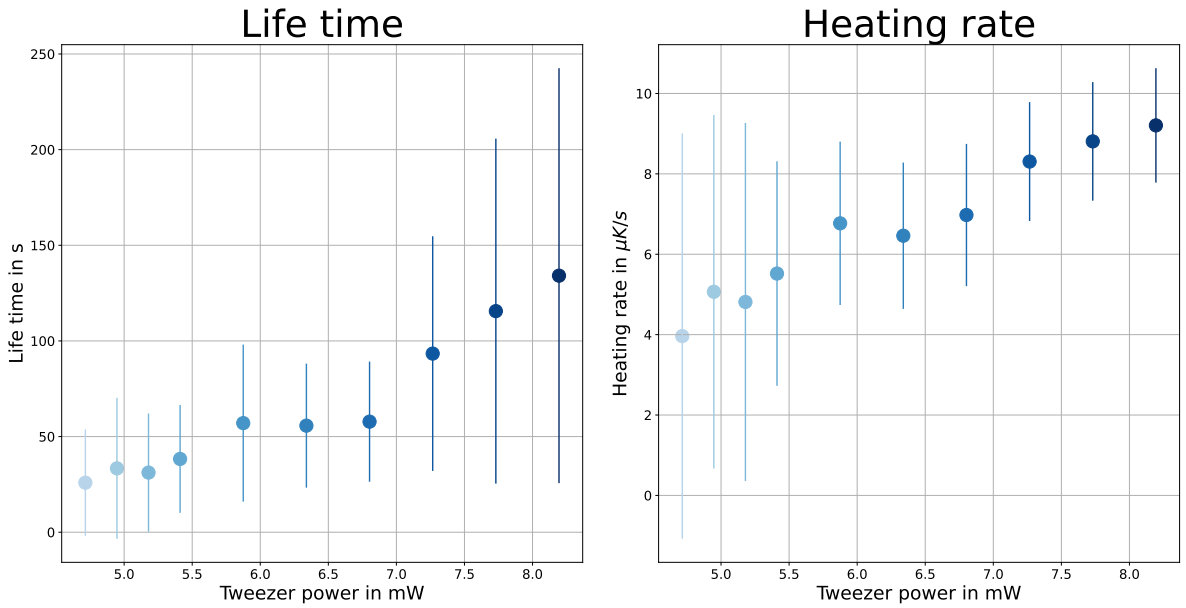

(a) **(b)**

Figure 6.15: Life time (a) and heating rate (b) extracted from the fit to the data points in 6.14. Both show an increase with increasing tweezer power. The data points are plotted in the same color code as the experimental data in figure 6.14

As an assumption free measure of the life time, the time where the population has dropped to 50 % of its initial value might be used. The corresponding values extracted from the data in

figure 6.14 are shown in figure 6.16. The life time in the deepest tweezers defined in this way is 22.8 s.

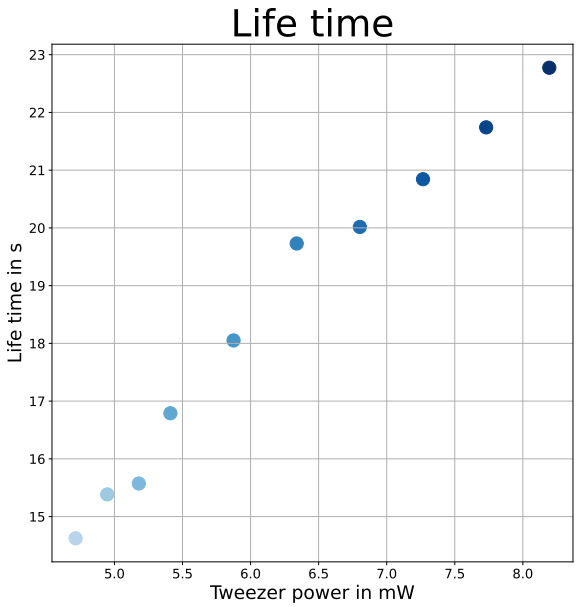

Figure 6.16: Life time as defined by a drop of population to 50 % of its initial value. The color code is the same as in figure 6.14.

For an array of 100 atoms, this would mean that the whole array has a life time of about 228 ms, after which there is a 50 % probability to have lost one atom from the array.
The heating rate can be explained by two possible processes:

- Scattering of trap photons by the atoms
- Technical heating due to position and intensity fluctuations.

The effect of the first process can be calculated from the scattering rate Γ_{SC} of photons at the trap wavelength of 532 nm by the atoms

$$\Gamma_{SC} = \frac{3\pi c^2 I}{2\hbar\omega_{at}^3}\left(\frac{\omega_L}{\omega_{at}}\right)^3\left(\frac{\Gamma}{\omega_{at}-\omega_L}+\frac{\Gamma}{\omega_{at}+\omega_L}\right)^2 \tag{6.4}$$

where ω_{at} is the transition frequency of the atom of 556 nm, Γ is the linewidth of the transition of 184 kHz, ω_{L} is the frequency of the laser and I is the intensity of the tweezer [121, 122]. The heating rate can than be calculated as $\alpha = T_{\mathrm{rec}}/(3 * \Gamma_{\mathrm{SC}})$. The heating rates calculated in this way are on the order of $0.01\,\mu K/s$ and can not explain the measured heating rates.
To assess the technical heating from intensity fluctuations from the trap, one has to measure the power spectral density of the noise at twice the trap frequency [123]. The heating rate can then be expressed in terms of the e-fold time of the temperature as

$$\Gamma_{\mathrm{Noise,i}} = \frac{1}{T_{\mathrm{e-fold}}} = \pi^2 \nu_{\mathrm{i}}^2 S_k(2\nu_{\mathrm{i}}) \tag{6.5}$$

with the trap frequency in direction i ν_i and the power spectral density of the noise $S_k(2\nu_i)$. The total rate constant for three dimensions of a radially symmetric tweezer is then $\Gamma_{\text{Noise,tot}} = (2 * \Gamma_r + \Gamma_a)$ with r standing for the radial and a for the axial direction.
To compare this measure to the measured heating rates, these need to be converted to an e-fold time together with the known temperature as $(31\,\mu K * e)/\alpha$. The corresponding spectrum of the intensity stabilization and the comparison between the measured and modeled e-fold times can be seen in figure 6.17.

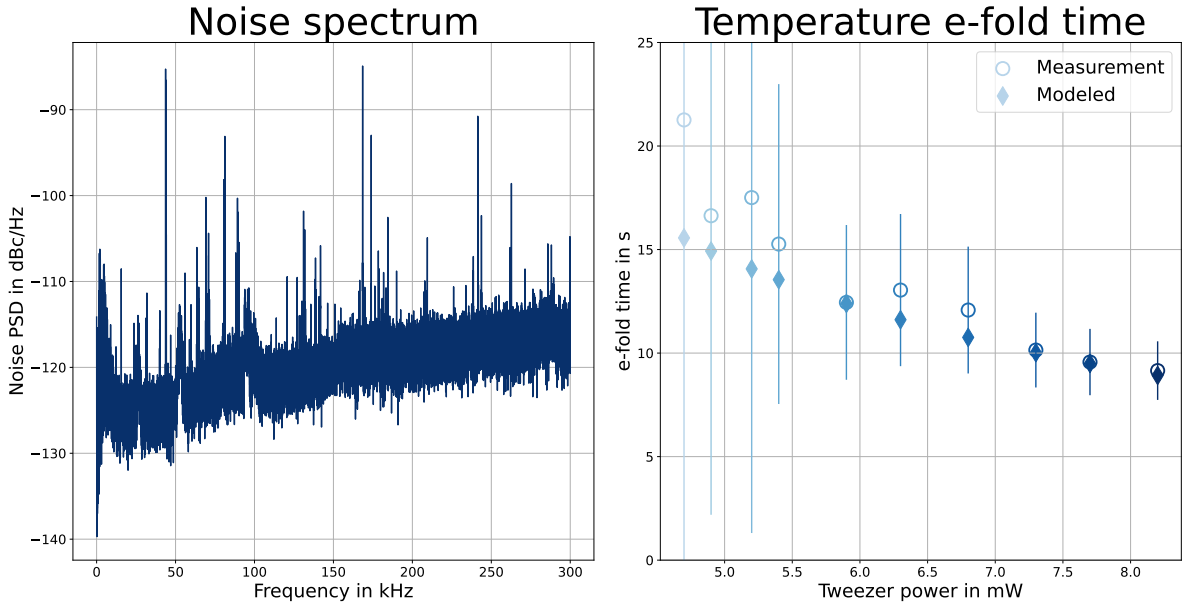

(a) **(b)**

Figure 6.17: (a) Noise spectrum of the intensity stabilization used for the tweezer light. (b) Measured and modeled e-fold time of the temperature. The qualitative behavior as well as the magnitude of the heating is well explained by the modeled heating rates from the intensity noise. Note that the error bars on the first data points are larger than the y-axis, which has been chosen to show the difference between modeled and measured rates. The calculated radial trap frequencies are [93.1(1), 95.0(1), 97.9(1), 99.8(1), 104.3(1), 107.8(1), 111.9(1), 116.0(1), 119.1(1), 122.9(1)] kHz and the axial trap frequencies are [8.94(2), 9.13(2), 9.41(2), 9.59(2), 10.02(2), 10.36(2), 10.76(2), 11.15(2), 11.45(2), 11.82(2)] kHz for the measured intensities.

As can be seen from the comparison of the modeled and measured heating rates presented in figure 6.17 (b), the qualitative behavior as well as the magnitude of the heating is well explained by the heating from the intensity fluctuations. To mitigate this effect in the future, interleaved slots of optimized cooling need to be employed in future experiments. This strategy is also used in other experiments with life times on the order of several minutes [124] and might push the life time in the experiment closer to the observed 134 s limited by collisions with residual background gas atoms.

Bright life time

For the second life time characterization, the measurement procedure as described above is repeated, but now during holding the imaging beams are turned on at their loss-optimal settings of 11.1 I_{sat} and a detuning of -1.87 Γ_{556}6.1.
The experimental data points shown in 6.18 (a) are described well by a simple exponential decay

$$P_{\text{imaging}}(t) = e^{-\frac{t}{\tau}} \tag{6.6}$$

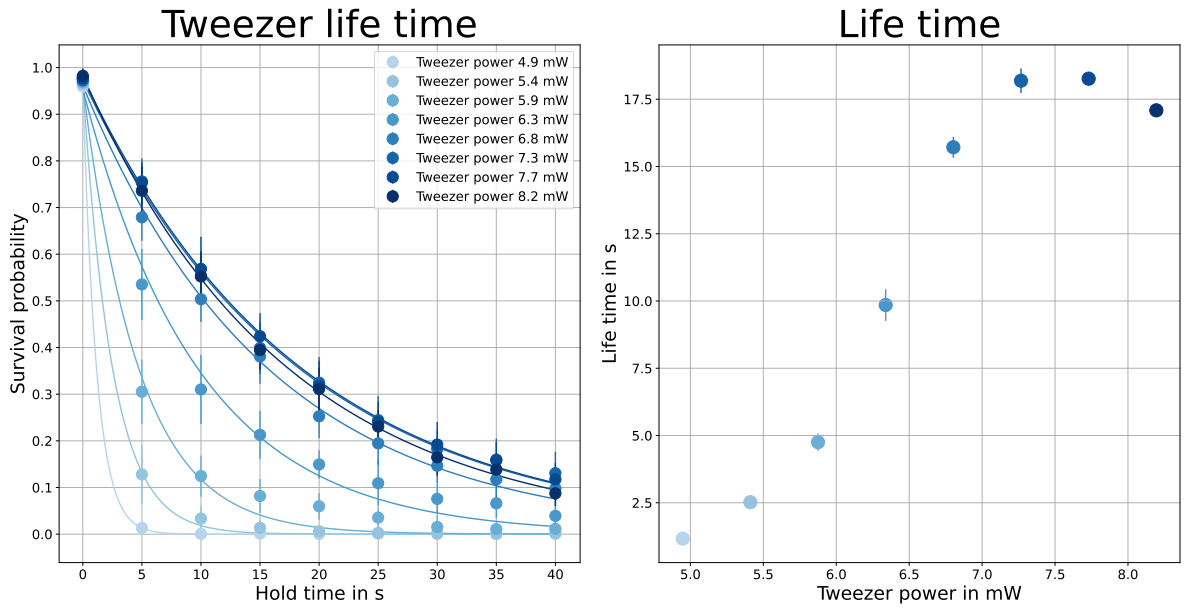

(a) **(b)**

Figure 6.18: (a) Survival probability of atoms in tweezers with the imaging beams on during holding for different tweezer power. The lines are a fit with equation 6.6. (b) Life times extracted from the fits, data points plotted in the same color code as the data in the before mentioned figure. The life time increases with increasing tweezer power until it saturates at $18.25 \pm 0.26\,s$ for a tweezer power of 7.7 mW. The drop in life time for even higher tweezer powers might be due to three photon processes.

The life times extracted from the fit presented in figure 6.18 (b) show an increasing life time with increasing tweezer power, the largest life time of $18.25 \pm 0.26\,s$ being achieved at a tweezer power of 7.7 mW. This behavior is followed by a decrease in life time for higher tweezer powers indicated by the last data point.
The behavior at small tweezer powers can be explained by heating from the momentum diffusion process due to photon scattering and can in principle be simulated by the dynamics of a classical particle in a 3D gaussian potential subject to damping and diffusion caused by the Doppler cooling and photon scattering [125].
The decrease in life time might be explained by three photon processes involving one imaging photon at 556 nm and two trap photons of 532 nm and either off resonant scattering to one of

the metastable states or ionization might be possible, the later because the energy of all three photons is higher than the ionization threshold. The same process was speculated on in [125] for ^{171}Yb in 486 nm tweezers, for more detailed analysis measurements of the life time at even higher tweezer powers should be performed. This study is left for future work.

6.5 Trap frequencies

To measure the trap frequencies of the optical tweezer, the power of the tweezer is modulated with a sine function of frequency f_{mod} and a modulation depth of 10 % for different tweezer powers. The effect of this parametric heating experiment is atom loss from the trap when the modulation frequency is $f_{mod} = 2 * f_{Trap}$.
The trap frequencies of an optical potential in the harmonic approximation can be written as

$$2\pi * \omega_{radial} = \sqrt{\frac{4 * U_0}{m_{Yb} * w_0^2}} \tag{6.7}$$

$$2\pi * \omega_{axial} = \sqrt{\frac{2 * U_0}{m_{Yb} * z_R^2}} \tag{6.8}$$

for the axial and radial direction for an optical potential with potential depth U_0 and waist w_0 and z extent z_R.

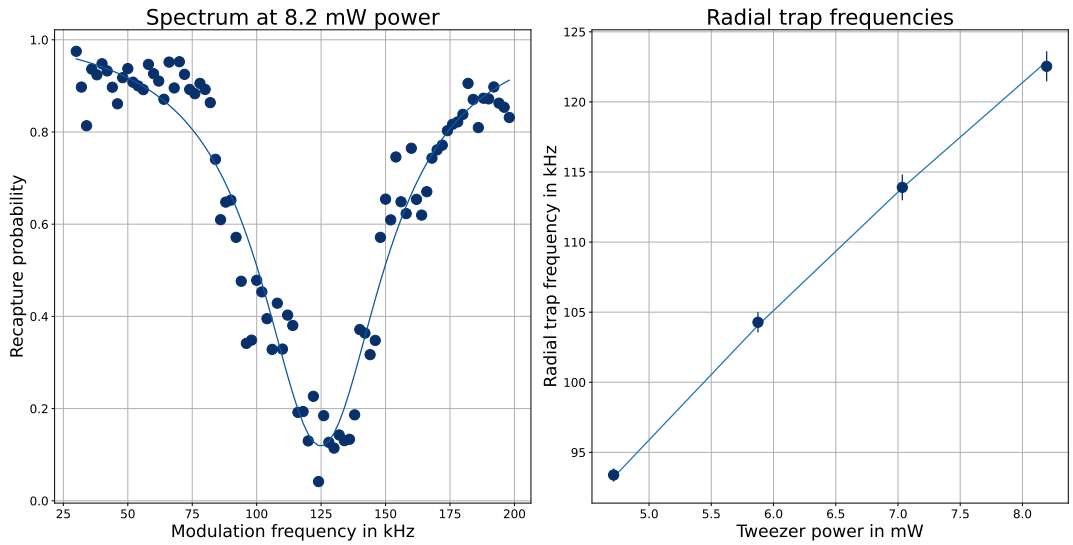

(a) **(b)**

Figure 6.19: (a) Example spectrum for the parametric heating experiment. (b) Extracted resonance peaks for different optical powers. The line is a fit with equation 6.11. The fit leads to a calbibration factor of $\omega_r(P) = 42.93 \pm 0.05 \frac{\text{kHz}}{\sqrt{\text{mW}}} * \sqrt{P}$.

When using the relation for the potential depth

$$U_0 = \frac{1}{2 * \varepsilon_0 * c} * \alpha_{Yb,532nm} * I_0 \tag{6.9}$$

where ε_0 is the electric field constant, c is the speed of light and $\alpha_{\mathrm{Yb},532nm}$ is the polarizability of Ytterbium at 532 nm[29] and the relation for the intensity

$$I_0 = \frac{2 * P}{\pi * w_0^2} \tag{6.10}$$

with the power of the tweezer P, one can derive the relation for the trap frequencies in relation to the optical power of the tweezer:

$$2\pi * \omega_{\mathrm{radial}} = \sqrt{\frac{4 * \alpha_{\mathrm{Yb,532nm}}}{\pi * \varepsilon_0 * c * m_{\mathrm{Yb}} * w_0^4}} * \sqrt{P} \tag{6.11}$$

$$2\pi * \omega_{\mathrm{axial}} = \sqrt{\frac{2 * \alpha_{\mathrm{Yb,532nm}}}{\pi * \varepsilon_0 * c * m_{\mathrm{Yb}} * w_0^2 * z_{\mathrm{R}}^2}} * \sqrt{P} \tag{6.12}$$

Figure 6.19 shows an example spectrum and the measured frequencies for the radial direction and figure 6.20 for the axial direction.

The author notes that this measurement is still inconclusive and both scans show the frequency f_{mod} as the trap frequency of the tweezer, not $f_{\mathrm{mod}}/2$, as this would not fit at all to the measured sizes and power. This might be explained by a modulation of the intensity so strong that the signal at the trap frequency was measured. The author notes that besides this assumption, a wider scan of the modulation frequency did not reveal any further resonances. A more careful measurement of the trap frequencies and also a independent measurement of the trap depth should be performed in the future.

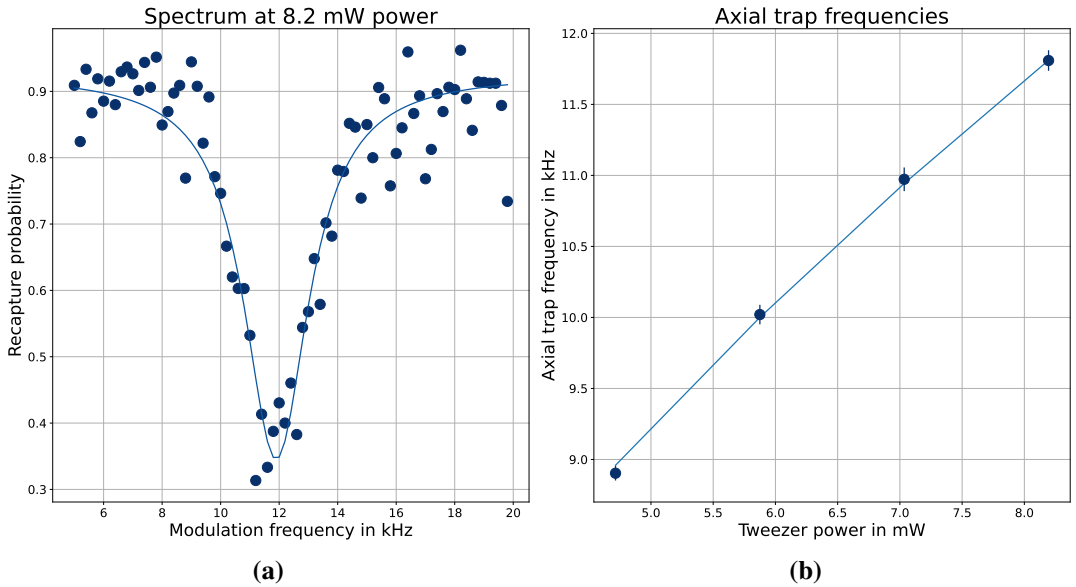

Figure 6.20: (a) Example spectrum for the parametric heating experiment. (b) Extracted resonance peaks for different optical powers. The line is a fit with equation 6.12. The fit leads to a calbibration factor of $\omega_{\mathrm{r}}(P) = 4.126 \pm 0.008 \frac{\mathrm{kHz}}{\sqrt{\mathrm{mW}}} * \sqrt{P}$.

[29]The value assumed here is 226 atomic units according to [126].

Non the less, it is possible to calculate the waist and Rayleigh range of the tweezer from the fit parameters of the fits to the trap frequencies against the power shown in figure 6.19 and 6.20. The waist of the tweezer extracted from this value is 540 ± 3 nm and the z-extent 3974 ± 10 nm, this is smaller compared to the size measured in chapter 4.3. One explanation for this might be an error in the magnification of the analysis branch, as a 10 % larger magnification would explain the smaller size. The author suggests checking the magnification of the analysis branch in an independent way.

7 Experimental setups for atom manipulation

This chapter describes the optical setups planned for addressing the transitions needed to implement Qubit-operations. It presents the planned setups for both π-polarization and σ-polarization to drive Raman transitions in the hyperfine manifold of the $^3P_0$ clock state, which in future will serve as the computational qubit in the omg-architecture. The beams will enable the driving of high-fidelity singe qubit gate operations in the future. As of writing this thesis, these setups still have to be implemented into the experiment. The calculations for the beam shaping were done by N. Pintul, see [94] for details, the setup was designed by the author and tested by T. Schacht. All work was performed under the supervision of C. Becker and K. Sengstock.

7.1 Optical design

After trapping and imaging single atoms, one of the next steps of the experiment will be exciting the atoms from the ground state to the metastable $^3P_0$ clock state and drive Raman transitions in its hyperfine manifold. For this, setups to adress the atoms with 578 nm and 649 nm light are required at the experiment.
As the transitions will be used to drive single qubit gates as proposed in the omg-architecture, it is important to carefully design the optical setups to achieve a homogeneous excitation probability over the whole array. Here, a careful balance between beam size and available laser power is required, dictating the array size the experiment can work with.
The optimal beam shape for the following setups was calculated by N. Pintul and is optimized for an area of 50 µm x 50 µm, this option being the first to be implemented at the experiment with options for lines or the whole field of view of the objectives of the size 200 µm x 200 µm preplanned.
The following two setups are shown for the 649 nm laser light used to drive Raman transitions in the $^3P_0$ state. Equivalent setups are planned for the 578 nm light required to drive the narrow clock transition.
As the beams will be used to drive single qubit gates, it is important that the setups allow for fast modulation of amplitude and phase on the timescale of the Rabi frequency without changing the pointing of the beam on the array. As such, a small waist AOM in doubeplass configuration is used in the 649 nm setup to allow for modulation on the order of 10 MHz. This will be important in the future to implement optimized qubit protocols.
As the achievable Rabi frequency on the narrow clock transition is much smaller on the order of 100 kHz, the two setups for addressing the atoms with 578 nm light are planned in single pass configuration at the moment.[30]

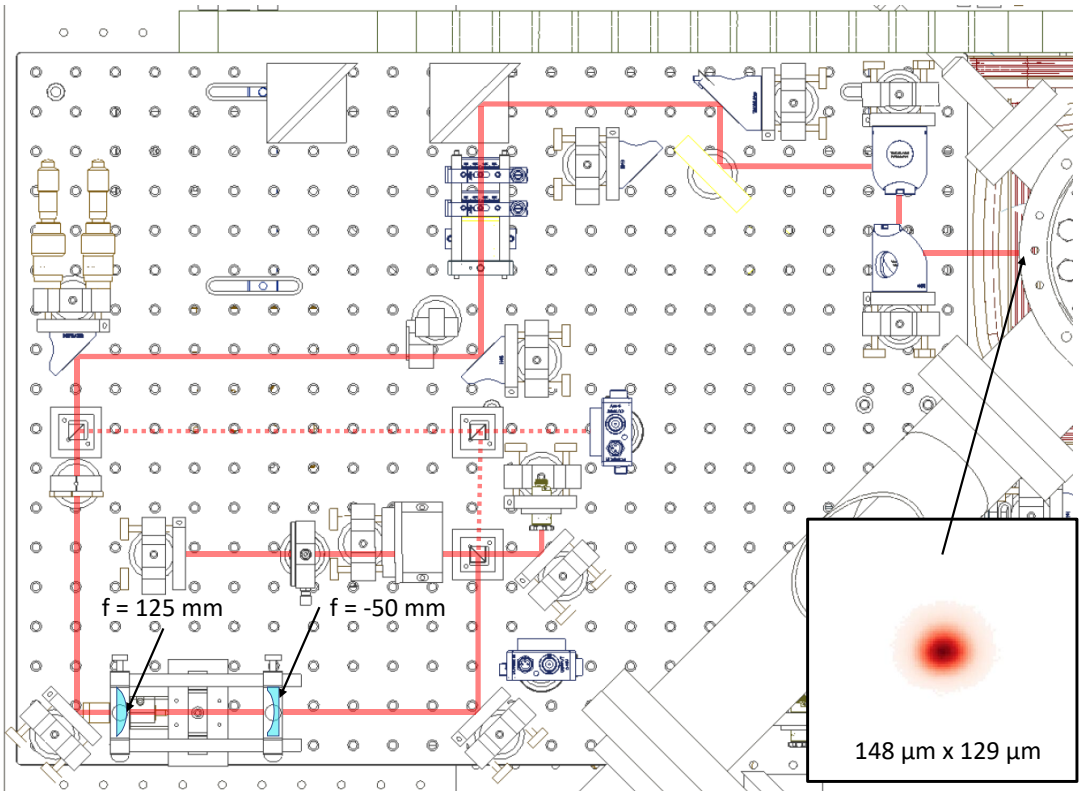

Figure 7.1: The setup to supply 649 nm light with π-polarization to the atoms located in the future on the left upper horizontal breadboard. The inset shows the beam at the positions of the atoms.

Setup for the diagonal beams

Figure 7.1 shows the setup for addressing the atoms in the array with 649 nm light on the diagonal axis of the experiment. This light propagates perpendicular to the quantization axis and can be set to π-polarization or tilted linear polarization.

The setup starts by focusing light from a polarization maintaining single-mode fiber into a small-waist acousto-optic modulator[31] in doublepass configuration. The beam diameter inside the AOM is 100 µm and leads to a rise time of 20 ns and a bandwidth of 31 MHz, as required on the order of the achievable Rabi frequency. After the double pass AOM, the beam is recollimated and focused on the atoms by a two lens telescope to a beam size of 148 µm by 129 µm.

Part of the light from before and after the AOM is picked off and overlapped on a beamsplitter and the signal monitored by a photodiode. This heterodyne detection setup allows for measuring of not only the amplitude but also the phase of the addressing beam [127].

As this beam can be used in tilted polarization, it can drive Raman transitions in the high Rabi frequency regime on its own [58]. It might also be used in conjunction with the beam propagating along the LA axis of the experiment to drive the Raman transition when configured in π-polarization.

[30] As the setups are not finished as of writing this thesis, the author points the reader to the future master thesis of T. Schacht for more details.

[31] Crystal Technology AOM-3200-121

Setup for the LA beams

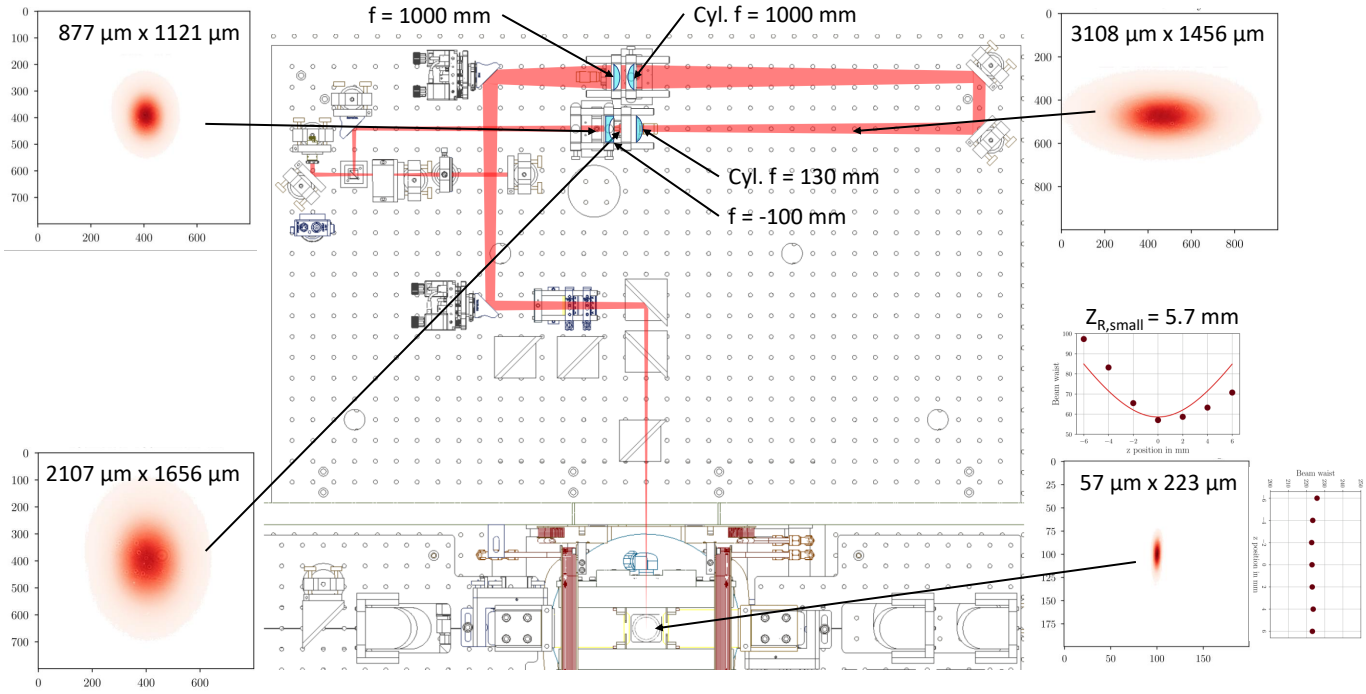

Figure 7.2: The setup to supply 649 nm light with σ-polarization to the atoms located in the future on the back horizontal breadboard. The insets show the beam and its diameter at different positions in the cylindrical telescope.

Figure 7.2 shows the setup for the LA beams for addressing the atoms with σ-polarization. The start of the setup is the same as for the diagonal beams with a small waist AOM in doublepass configuration. The setup for the LA beam does not include heterodyne detection, as only the phase of the diagonal beam will have to be modulated when using the beam as a pair to drive Raman transitions.
After the doublepass, the beam is recollimated and after that a cylindrical telescope consisting of four lenses forms the beam into a light sheet of dimension 57 µm by 223 µm with a Rayleigh range in the small direction of 5.7 mm for addressing of the array.

7.2 Performance

The two most crucial figures to assess the performance of the addressing system is the pointing stability and beam shape, as these two will effect the homogeneity of the excitation over the array. All measurements were done in the focus of the telescope at the point where the atoms would sit in the experiment.
Figure 7.3 (a) shows the stability of the addressing beam over a frequency tune range of 30 MHz. The stability in x-direction has a standard deviation of 2 µm and the y-direction a stability of 7.2 µm, the largest contribution in the y direction coming from the low frequency range from 190 MHz to 200 MHz. If the used frequency range is kept from 200 MHz to 220 MHz, the

stability in y-direction is reduced to 3 µm.

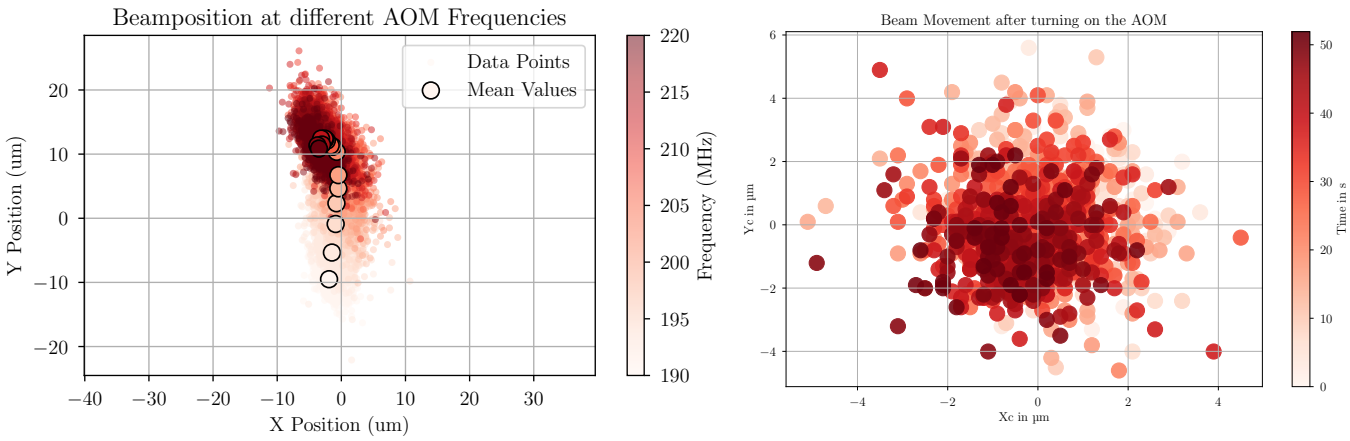

(a) (b)

Figure 7.3: (a) The frequency stability of the addressing setup over the frequency range from 190 MHz to 220 MHz measured in the focus of the telescope at the future position of the atoms. (b) The stability over time of the setup.

The stability when turning on the setup can be seen in figure 7.3 (b). The setups shows no effects of thermalization over the period of 50 s and the overall stability over time is 1.2 µm in x-direction and 1.5 µm in y-direction.
Figure 7.4 (a) shows the ellipticity of the beam over the whole frequency range. The beam shape is quenched in the y-direction for higher frequencies. Restricting the frequency range to 200 MHz to 220 MHz will also restrict this effect.

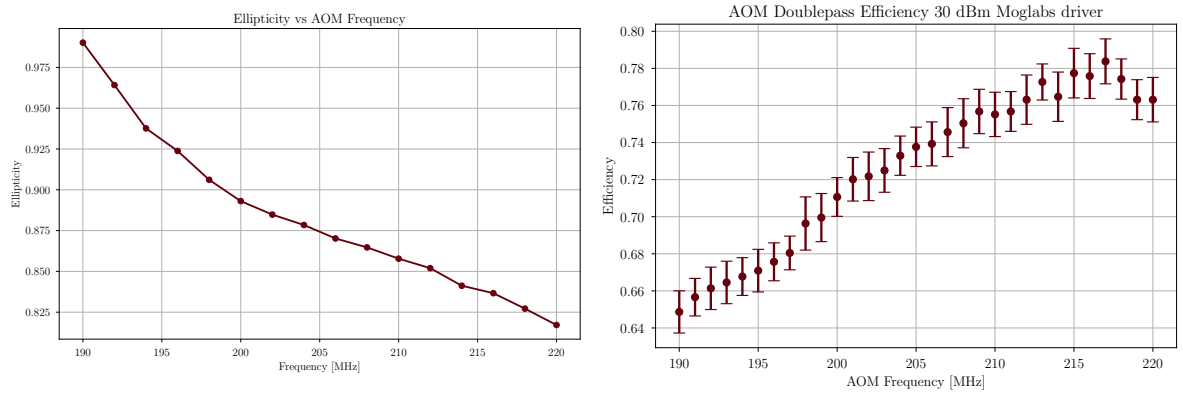

(a) (b)

Figure 7.4: (a) The ellipticity of the beam over the frequency range from 190 MHz to 220 MHz. (b) The efficiency of the doublepass setup over the frequency range from 190 MHz to 220 MHz.

Figure 7.4 (b) shows the efficiency of the double pass setup. Although a high efficiency is desirable to utilize the available laser power to the best, any change in efficiency over the frequency range will be corrected for in the pulse forms from the monitoring setup.
The stability reached is promising for achieving high-fidelity excitation over a 50 µm by 50 µm array in the near future.

8 Conclusion and outlook

In conclusion, this thesis presents a new experimental setup for trapping, imaging and manipulating of single Ytterbium atoms. Besides showcasing the experimental setups required for controlling the magnetic and electric field background, a setup for diffraction limited generation of optical tweezers at a wavelength of 532 nm with the aid of a pair of crossed acousto-optic deflectors was shown. Atoms trapped from a 3D magneto-optical trap in these light potentials were successfully imaged with a fidelity of 99.862 % while losing 1.2 % of atoms per image. The life time in the tweezers was shown to be on the order of 30 s and the temperature of the atoms in the tweezers was shown to be 31 µK.
The next experiment steps will be:

- Sorting of single atoms using the described setup with movable tweezers generated by acouto-optic deflectors to achieve defect-free arrays.
- Implementation of Raman sideband cooling to further reduce the atomic temperature.
- Implementation of the setup presented for atom manipulation at the experiment for clock excitation and Raman driving of the meta-stable clock qubit.
- Spectroscopy of the Rydberg state manifold for two-qubit gate implementation, for more details on the Rydberg laser system see [94].

As an outlook, figure 8.1 shows some of the first fermionic ^{171}Yb atoms trapped in arbitrary array geometries generated by a spatial light modulator at the clock magic wavelength of 759 nm. For more details on first experiments with ^{171}Yb atoms in magic tweezers see [94]. Two geometries are shown, an array of dimers that could be used for the study of optimized gate protocols between two atoms [128] and an edge Kagome lattice that in future could be used in the study of spin liquids [129, 130].

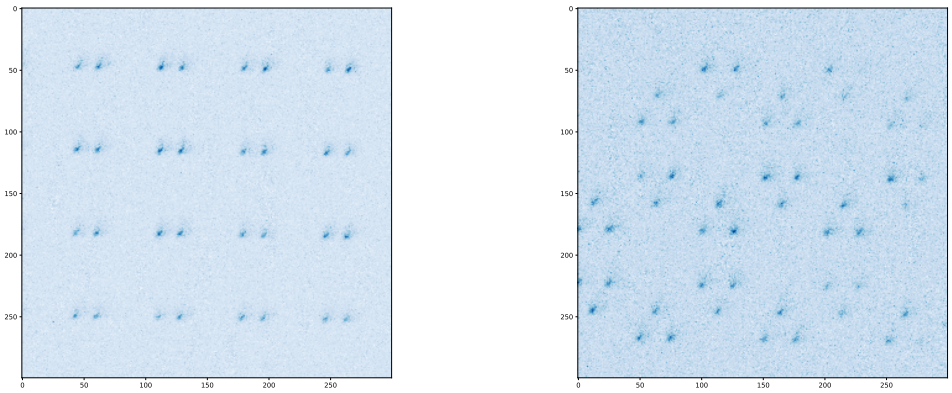

(a) **(b)**

Figure 8.1: Images averaged 60 times of ^{171}Yb atoms in magic tweezers generated by a SLM in (a) an array of dimers and (b) an edge Kagome lattice.

References

[1] R P Poplavskiĭ. Thermodynamic models of information processes. *Soviet Physics Uspekhi*, 18(3):222–241, March 1975.

[2] Paul Benioff. The computer as a physical system: A microscopic quantum mechanical hamiltonian model of computers as represented by turing machines. *Journal of Statistical Physics*, 22(5):563–591, May 1980.

[3] Paul Benioff. Quantum mechanical hamiltonian models of turing machines. *Journal of Statistical Physics*, 29(3):515–546, November 1982.

[4] David Deutsch. Quantum theory, the church-turing principle and the universal quantum computer. *Proceedings of the Royal Society A*, 1985.

[5] David Deutschand Richard Jozsa. Rapid solution of problems by quantum computation. *Proceedings of the Royal Society A*, 1992.

[6] Peter W. Shor. Polynomial-time algorithms for prime factorization and discrete logarithms on a quantum computer. *SIAM Journal on Computing*, 26(5):1484–1509, October 1997.

[7] Lov K. Grover. Quantum mechanics helps in searching for a needle in a haystack. *Physical Review Letters*, 79(2):325–328, July 1997.

[8] David P. DiVincenzo. Topics in quantum computers. December 1996.

[9] V. Bouchiat, D. Vion, P. Joyez, D. Esteve, and M. H. Devoret. Quantum coherence with a single cooper pair. *Physica Scripta*, T76(1):165, 1998.

[10] J. E. Mooij, T. P. Orlando, L. Levitov, Lin Tian, Caspar H. van der Wal, and Seth Lloyd. Josephson persistent-current qubit. *Science*, 285(5430):1036–1039, August 1999.

[11] Y. Nakamura, Yu. A. Pashkin, and J. S. Tsai. Coherent control of macroscopic quantum states in a single-cooper-pair box. *Nature*, 398(6730):786–788, April 1999.

[12] William M. Kaminsky, Seth Lloyd, and Terry P. Orlando. Scalable superconducting architecture for adiabatic quantum computation, 2004.

[13] John Clarke and Frank K. Wilhelm. Superconducting quantum bits. *Nature*, 453(7198):1031–1042, June 2008.

[14] Jens Koch, Terri M. Yu, Jay Gambetta, A. A. Houck, D. I. Schuster, J. Majer, Alexandre Blais, M. H. Devoret, S. M. Girvin, and R. J. Schoelkopf. Charge-insensitive qubit design derived from the cooper pair box. *Physical Review A*, 76(4):042319, October 2007.

[15] Vladimir E. Manucharyan, Jens Koch, Leonid I. Glazman, and Michel H. Devoret. Fluxonium: Single cooper-pair circuit free of charge offsets. *Science*, 326(5949):113–116, October 2009.

[16] John M. Martinis. Superconducting phase qubits. *Quantum Information Processing*, 8(2–3):81–103, February 2009.

[17] J. I. Cirac and P. Zoller. Quantum computations with cold trapped ions. *Physical Review Letters*, 74(20):4091–4094, May 1995.

[18] B. B. Blinov, D. Leibfried, C. Monroe, and D. J. Wineland. Quantum computing with trapped ion hyperfine qubits. *Quantum Information Processing*, 3(1–5):45–59, October 2004.

[19] Martin Ringbauer, Michael Meth, Lukas Postler, Roman Stricker, Rainer Blatt, Philipp Schindler, and Thomas Monz. A universal qudit quantum processor with trapped ions. *Nature Physics*, 18(9):1053–1057, July 2022.

[20] C. Adami and N. J. Cerf. *Quantum Computation with Linear Optics*, pages 391–401. Springer Berlin Heidelberg, 1999.

[21] E. Knill, R. Laflamme, and G. J. Milburn. A scheme for efficient quantum computation with linear optics. *Nature*, 409(6816):46–52, January 2001.

[22] Pieter Kok, W. J. Munro, Kae Nemoto, T. C. Ralph, Jonathan P. Dowling, and G. J. Milburn. Linear optical quantum computing with photonic qubits. *Reviews of Modern Physics*, 79(1):135–174, January 2007.

[23] A. P. Nizovtsev. A quantum computer based on nv centers in diamond: Optically detected nutations of single electron and nuclear spins. *Optics and Spectroscopy*, 99(2):233, 2005.

[24] M. V. Gurudev Dutt, L. Childress, L. Jiang, E. Togan, J. Maze, F. Jelezko, A. S. Zibrov, P. R. Hemmer, and M. D. Lukin. Quantum register based on individual electronic and nuclear spin qubits in diamond. *Science*, 316(5829):1312–1316, June 2007.

[25] P. Neumann, N. Mizuochi, F. Rempp, P. Hemmer, H. Watanabe, S. Yamasaki, V. Jacques, T. Gaebel, F. Jelezko, and J. Wrachtrup. Multipartite entanglement among single spins in diamond. *Science*, 320(5881):1326–1329, June 2008.

[26] Loïc Henriet, Lucas Beguin, Adrien Signoles, Thierry Lahaye, Antoine Browaeys, Georges-Olivier Reymond, and Christophe Jurczak. Quantum computing with neutral atoms. *Quantum*, 4:327, September 2020.

[27] Florian Schäfer, Takeshi Fukuhara, Seiji Sugawa, Yosuke Takasu, and Yoshiro Takahashi. Tools for quantum simulation with ultracold atoms in optical lattices. *Nature Reviews Physics*, 2(8):411–425, July 2020.

[28] T. Calarco, H. J. Briegel, D. Jaksch, J. I. Cirac, and P. Zoller. Entangling neutral atoms for quantum information processing. *Journal of Modern Optics*, 47(12):2137–2149, October 2000.

[29] D. Jaksch, H.-J. Briegel, J. I. Cirac, C. W. Gardiner, and P. Zoller. Entanglement of atoms via cold controlled collisions. *Physical Review Letters*, 82(9):1975–1978, March 1999.

[30] Gavin K. Brennen, Carlton M. Caves, Poul S. Jessen, and Ivan H. Deutsch. Quantum logic gates in optical lattices. *Physical Review Letters*, 82(5):1060–1063, February 1999.

[31] D. Jaksch, J. I. Cirac, P. Zoller, S. L. Rolston, R. Côté, and M. D. Lukin. Fast quantum gates for neutral atoms. *Physical Review Letters*, 85(10):2208–2211, September 2000.

[32] I. E. Protsenko, G. Reymond, N. Schlosser, and P. Grangier. Operation of a quantum phase gate using neutral atoms in microscopic dipole traps. *Physical Review A*, 65(5):052301, April 2002.

[33] Nicolas Schlosser, Georges Reymond, Igor Protsenko, and Philippe Grangier. Sub-poissonian loading of single atoms in a microscopic dipole trap. *Nature*, 411(6841):1024–1027, June 2001.

[34] R. Dumke, M. Volk, T. Müther, F. B. J. Buchkremer, G. Birkl, and W. Ertmer. Micro-optical realization of arrays of selectively addressable dipole traps: A scalable configuration for quantum computation with atomic qubits. *Physical Review Letters*, 89(9):097903, August 2002.

[35] T. A. Johnson, E. Urban, T. Henage, L. Isenhower, D. D. Yavuz, T. G. Walker, and M. Saffman. Rabi oscillations between ground and rydberg states with dipole-dipole atomic interactions. *Physical Review Letters*, 100(11):113003, March 2008.

[36] L. Isenhower, E. Urban, X. L. Zhang, A. T. Gill, T. Henage, T. A. Johnson, T. G. Walker, and M. Saffman. Demonstration of a neutral atom controlled-not quantum gate. *Physical Review Letters*, 104(1):010503, January 2010.

[37] T. Wilk, A. Gaëtan, C. Evellin, J. Wolters, Y. Miroshnychenko, P. Grangier, and A. Browaeys. Entanglement of two individual neutral atoms using rydberg blockade. *Physical Review Letters*, 104(1):010502, January 2010.

[38] Silvia Bergamini, Benoît Darquié, Matthew Jones, Lionel Jacubowiez, Antoine Browaeys, and Philippe Grangier. Holographic generation of microtrap arrays for single atoms by use of a programmable phase modulator. *Journal of the Optical Society of America B*, 21(11):1889, November 2004.

[39] F. Nogrette, H. Labuhn, S. Ravets, D. Barredo, L. Béguin, A. Vernier, T. Lahaye, and A. Browaeys. Single-atom trapping in holographic 2d arrays of microtraps with arbitrary geometries. *Physical Review X*, 4(2):021034, May 2014.

[40] Marshall T. DePue, Colin McCormick, S. Lukman Winoto, Steven Oliver, and David S. Weiss. Unity occupation of sites in a 3d optical lattice. *Physical Review Letters*, 82(11):2262–2265, March 1999.

[41] Karl D. Nelson, Xiao Li, and David S. Weiss. Imaging single atoms in a three-dimensional array. *Nature Physics*, 3(8):556–560, June 2007.

[42] T. Gruenzweig, A. Hilliard, M. McGovern, and M. F. Andersen. Near-deterministic preparation of a single atom in an optical microtrap. *Nature Physics*, 6(12):951–954, September 2010.

[43] Jérôme Beugnon, Charles Tuchendler, Harold Marion, Alpha Gaëtan, Yevhen Miroshnychenko, Yvan R. P. Sortais, Andrew M. Lance, Matthew P. A. Jones, Gaétan Messin, Antoine Browaeys, and Philippe Grangier. Two-dimensional transport and transfer of a single atomic qubit in optical tweezers. *Nature Physics*, 3(10):696–699, August 2007.

[44] Daniel Barredo, Sylvain de Léséleuc, Vincent Lienhard, Thierry Lahaye, and Antoine Browaeys. An atom-by-atom assembler of defect-free arbitrary two-dimensional atomic arrays. *Science*, 354(6315):1021–1023, November 2016.

[45] Manuel Endres, Hannes Bernien, Alexander Keesling, Harry Levine, Eric R. Anschuetz, Alexandre Krajenbrink, Crystal Senko, Vladan Vuletic, Markus Greiner, and Mikhail D. Lukin. Atom-by-atom assembly of defect-free one-dimensional cold atom arrays. *Science*, 354(6315):1024–1027, November 2016.

[46] Aishwarya Kumar, Tsung-Yao Wu, Felipe Giraldo, and David S. Weiss. Sorting ultracold atoms in a three-dimensional optical lattice in a realization of maxwells demon. *Nature*, 561(7721):83–87, September 2018.

[47] H. C. Naegerl, D. Leibfried, H. Rohde, G. Thalhammer, J. Eschner, F. Schmidt-Kaler, and R. Blatt. Laser addressing of individual ions in a linear ion trap. *Physical Review A*, 60(1):145–148, July 1999.

[48] Sangtaek Kim, Robert R. Mcleod, M. Saffman, and Kelvin H. Wagner. Doppler-free, multiwavelength acousto-optic deflector for two-photon addressing arrays of rb atoms in a quantum information processor. *Applied Optics*, 47(11):1816, April 2008.

[49] J. D. Thompson, T. G. Tiecke, A. S. Zibrov, V. Vuletic, and M. D. Lukin. Coherence and raman sideband cooling of a single atom in an optical tweezer. *Physical Review Letters*, 110(13):133001, March 2013.

[50] A. M. Kaufman, B. J. Lester, and C. A. Regal. Cooling a single atom in an optical tweezer to its quantum ground state. *Physical Review X*, 2(4):041014, November 2012.

[51] M. Saffman, T. G. Walker, and K. Mølmer. Quantum information with rydberg atoms. *Reviews of Modern Physics*, 82(3):2313–2363, August 2010.

[52] Alexandre Cooper, Jacob P. Covey, Ivaylo S. Madjarov, Sergey G. Porsev, Marianna S. Safronova, and Manuel Endres. Alkaline-earth atoms in optical tweezers. *Physical Review X*, 8(4):041055, December 2018.

[53] M. A. Norcia, A. W. Young, and A. M. Kaufman. Microscopic control and detection of ultracold strontium in optical-tweezer arrays. *Physical Review X*, 8(4):041054, December 2018.

[54] S. Saskin, J. T. Wilson, B. Grinkemeyer, and J. D. Thompson. Narrow-line cooling and imaging of ytterbium atoms in an optical tweezer array. *Physical Review Letters*, 122(14):143002, April 2019.

[55] Adam M. Kaufman and Kang-Kuen Ni. Quantum science with optical tweezer arrays of ultracold atoms and molecules. *Nature Physics*, 17(12):1324–1333, November 2021.

[56] Antoine Browaeys and Thierry Lahaye. Many-body physics with individually controlled rydberg atoms. *Nature Physics*, 16(2):132–142, January 2020.

[57] Hannah J. Manetsch, Gyohei Nomura, Elie Bataille, Kon H. Leung, Xudong Lv, and Manuel Endres. A tweezer array with 6100 highly coherent atomic qubits, 2024.

[58] Alec Jenkins, Joanna W. Lis, Aruku Senoo, William F. McGrew, and Adam M. Kaufman. Ytterbium nuclear-spin qubits in an optical tweezer array. *Physical Review X*, 12(2):021027, May 2022.

[59] Yue Wu, Shimon Kolkowitz, Shruti Puri, and Jeff D. Thompson. Erasure conversion for fault-tolerant quantum computing in alkaline earth rydberg atom arrays. *Nature Communications*, 13(1), August 2022.

[60] Shuo Ma, Alex P. Burgers, Genyue Liu, Jack Wilson, Bichen Zhang, and Jeff D. Thompson. Universal gate operations on nuclear spin qubits in an optical tweezer array of yb171 atoms. *Physical Review X*, 12(2):021028, May 2022.

[61] Tobias Bothwell, Wesley Brand, Robert Fasano, Thomas Akin, Joseph Whalen, Tanner Grogan, Yun-Jhih Chen, Marco Pomponio, Takuma Nakamura, Benjamin Rauf, Ignacio Baldoni, Michele Giunta, Ronald Holzwarth, Craig Nelson, Archita Hati, Franklyn Quinlan, Richard Fox, Steven Peil, and Andrew Ludlow. Deployment of a transportable yb optical lattice clock. *Opt. Lett. 50, 646-649*, 2025.

[62] Neville Chen, Lintao Li, William Huie, Mingkun Zhao, Ian Vetter, Chris H. Greene, and Jacob P. Covey. Analyzing the rydberg-based optical-metastable-ground architecture for yb171 nuclear spins. *Physical Review A*, 105(5):052438, May 2022.

[63] J. A. Muniz, M. Stone, D. T. Stack, M. Jaffe, J. M. Kindem, L. Wadleigh, E. Zalys-Geller, X. Zhang, C. A. Chen, M. A. Norcia, J. Epstein, E. Halperin, F. Hummel, T. Wilkason, M. Li, K. Barnes, P. Battaglino, T. C. Bohdanowicz, G. Booth, A. Brown, M. O. Brown, W. B. Cairncross, K. Cassella, R. Coxe, D. Crow, M. Feldkamp, C. Griger, A. Heinz, A. M. W. Jones, H. Kim, J. King, K. Kotru, J. Lauigan, J. Marjanovic, E. Megidish, M. Meredith, M. McDonald, R. Morshead, S. Narayanaswami, C. Nishiguchi, T. Paule, K. A. Pawlak, K. L. Pudenz, D. Rodríguez Pérez, A. Ryou, J. Simon, A. Smull, M. Urbanek, R. J. M. van de Veerdonk, Z. Vendeiro, T. Y. Wu, X. Xie, and B. J. Bloom. High-fidelity universal gates in the ^{171}yb ground state nuclear spin qubit, 2024.

[64] Michael Peper, Yiyi Li, Daniel Y. Knapp, Mila Bileska, Shuo Ma, Genyue Liu, Pai Peng, Bichen Zhang, Sebastian P. Horvath, Alex P. Burgers, and Jeff D. Thompson. Spectroscopy and Modeling of Yb-171 Rydberg States for High-Fidelity Two-Qubit Gates. *Physical Review X*, 15(1):011009, January 2025.

[65] M. A. Norcia, W. B. Cairncross, K. Barnes, P. Battaglino, A. Brown, M. O. Brown, K. Cassella, C.-A. Chen, R. Coxe, D. Crow, J. Epstein, C. Griger, A. M. W. Jones, H. Kim, J. M. Kindem, J. King, S. S. Kondov, K. Kotru, J. Lauigan, M. Li, M. Lu, E. Megidish, J. Marjanovic, M. McDonald, T. Mittiga, J. A. Muniz, S. Narayanaswami, C. Nishiguchi, R. Notermans, T. Paule, K. A. Pawlak, L. S. Peng, A. Ryou, A. Smull, D. Stack, M. Stone, A. Sucich, M. Urbanek, R. J. M. van de Veerdonk, Z. Vendeiro, T. Wilkason, T.-Y. Wu, X. Xie, X. Zhang, and B. J. Bloom. Midcircuit qubit measurement and rearrangement in a yb171 atomic array. *Physical Review X*, 13(4):041034, November 2023.

[66] Joanna W. Lis, Aruku Senoo, William F. McGrew, Felix Rönchen, Alec Jenkins, and Adam M. Kaufman. Midcircuit operations using the omg architecture in neutral atom arrays. *Physical Review X*, 13(4):041035, November 2023.

[67] William Huie, Lintao Li, Neville Chen, Xiye Hu, Zhubing Jia, Won Kyu Calvin Sun, and Jacob P. Covey. Repetitive readout and real-time control of nuclear spin qubits in 171yb atoms. *PRX Quantum*, 4(3):030337, September 2023.

[68] Shuo Ma, Genyue Liu, Pai Peng, Bichen Zhang, Sven Jandura, Jahan Claes, Alex P. Burgers, Guido Pupillo, Shruti Puri, and Jeff D. Thompson. High-fidelity gates and mid-circuit erasure conversion in an atomic qubit. *Nature*, 622(7982):279–284, October 2023.

[69] Ben W. Reichardt, Adam Paetznick, David Aasen, Ivan Basov, Juan M. Bello-Rivas, Parsa Bonderson, Rui Chao, Wim van Dam, Matthew B. Hastings, Andres Paz, Marcus P. da Silva, Aarthi Sundaram, Krysta M. Svore, Alexander Vaschillo, Zhenghan Wang, Matt Zanner, William B. Cairncross, Cheng-An Chen, Daniel Crow, Hyosub Kim, Jonathan M. Kindem, Jonathan King, Michael McDonald, Matthew A. Norcia,

Albert Ryou, Mark Stone, Laura Wadleigh, Katrina Barnes, Peter Battaglino, Thomas C. Bohdanowicz, Graham Booth, Andrew Brown, Mark O. Brown, Kayleigh Cassella, Robin Coxe, Jeffrey M. Epstein, Max Feldkamp, Christopher Griger, Eli Halperin, Andre Heinz, Frederic Hummel, Matthew Jaffe, Antonia M. W. Jones, Eliot Kapit, Krish Kotru, Joseph Lauigan, Ming Li, Jan Marjanovic, Eli Megidish, Matthew Meredith, Ryan Morshead, Juan A. Muniz, Sandeep Narayanaswami, Ciro Nishiguchi, Timothy Paule, Kelly A. Pawlak, Kristen L. Pudenz, David Rodríguez Pérez, Jon Simon, Aaron Smull, Daniel Stack, Miroslav Urbanek, Re. Logical computation demonstrated with a neutral atom quantum processor, 2024.

[70] Bichen Zhang, Pai Peng, Aditya Paul, and Jeff D. Thompson. Scaled local gate controller for optically addressed qubits. *Optica*, 11(2):227, February 2024.

[71] Francesco Scazza. *Probing SU(N)-symmetric orbital interactions with ytterbium Fermi gases in optical lattices*. PhD thesis, 2015.

[72] Ivaylo S. Madjarov, Jacob P. Covey, Adam L. Shaw, Joonhee Choi, Anant Kale, Alexandre Cooper, Hannes Pichler, Vladimir Schkolnik, Jason R. Williams, and Manuel Endres. High-fidelity entanglement and detection of alkaline-earth Rydberg atoms. *Nature Physics*, 16(8):857–861, May 2020.

[73] Alex P. Burgers, Shuo Ma, Sam Saskin, Jack Wilson, Miguel A. Alarcon, Chris H. Greene, and Jeff D. Thompson. Controlling Rydberg Excitations Using Ion-Core Transitions in Alkaline-Earth Atom-Tweezer Arrays. *PRX Quantum*, 3(2):020326, May 2022.

[74] W. E. Cooke, T. F. Gallagher, S. A. Edelstein, and R. M. Hill. Doubly excited autoionizing rydberg states of sr. *Physical Review Letters*, 40(3):178–181, January 1978.

[75] K. Honda, Y. Takahashi, T. Kuwamoto, M. Fujimoto, K. Toyoda, K. Ishikawa, and T. Yabuzaki. Magneto-optical trapping of yb atoms and a limit on the branching ratio of the1p1state. *Physical Review A*, 59(2):R934–R937, February 1999.

[76] Sören Dörscher, Alexander Thobe, Bastian Hundt, André Kochanke, Rodolphe Le Targat, Patrick Windpassinger, Christoph Becker, and Klaus Sengstock. Creation of quantum-degenerate gases of ytterbium in a compact 2d-/3d-magneto-optical trap setup. *Review of Scientific Instruments*, 84(4), April 2013.

[77] T. Kuwamoto, K. Honda, Y. Takahashi, and T. Yabuzaki. Magneto-optical trapping of yb atoms using an intercombination transition. *Physical Review A*, 60(2):R745–R748, August 1999.

[78] Lintao Li, Xiye Hu, Zhubing Jia, William Huie, Won Kyu Calvin Sun, Aakash, Yuhao Dong, Narisak Hiri-O-Tuppa, and Jacob P. Covey. Parallelized telecom quantum networking with a ytterbium-171 atom array. February 2025.

[79] Sergey G. Porsev, Andrei Derevianko, and E. N. Fortson. Possibility of an optical clock using the 1S0 –> 3P0 transition in 171,173Yb atoms held in an optical lattice. *Physical Review A*, 69(2):021403, February 2004.

[80] Z. Barber, C. Hoyt, C. Oates, L. Hollberg, A. Taichenachev, and V. Yudin. Direct excitation of the forbidden clock transition in neutralyb174atoms confined to an optical lattice. *Physical Review Letters*, 96(8):083002, March 2006.

[81] Iris Reichenbach and Ivan H. Deutsch. Sideband cooling while preserving coherences in the nuclear spin state in group-ii-like atoms. *Physical Review Letters*, 99(12):123001, September 2007.

[82] X. Zhang, K. Beloy, Y. S. Hassan, W. F. McGrew, C.-C. Chen, J. L. Siegel, T. Grogan, and A. D. Ludlow. Subrecoil clock-transition laser cooling enabling shallow optical lattice clocks. *Physical Review Letters*, 129(11):113202, September 2022.

[83] Guido Pagano, Francesco Scazza, and Michael Foss-Feig. Fast and scalable quantum information processing with two-electron atoms in optical tweezer arrays. *Advanced Quantum Technologies*, 2(3-4), January 2019.

[84] Jacob P. Covey, Alp Sipahigil, Szilard Szoke, Neil Sinclair, Manuel Endres, and Oskar Painter. Telecom-band quantum optics with ytterbium atoms and silicon nanophotonics. *Physical Review Applied*, 11(3):034044, March 2019.

[85] Yiyi Li and Jeff D. Thompson. High-rate and high-fidelity modular interconnects between neutral atom quantum processors. *PRX Quantum*, 5(2):020363, June 2024.

[86] Tim O. Hoehn, Etienne Staub, Guillaume Brochier, Nelson Darkwah Oppong, and Monika Aidelsburger. State-dependent potentials for the 1S0 and 3P0 clock states of neutral ytterbium atoms. *Physical Review A*, 108(5):053325, November 2023.

[87] Katrina Barnes, Peter Battaglino, Benjamin J. Bloom, Kayleigh Cassella, Robin Coxe, Nicole Crisosto, Jonathan P. King, Stanimir S. Kondov, Krish Kotru, Stuart C. Larsen, Joseph Lauigan, Brian J. Lester, Mickey McDonald, Eli Megidish, Sandeep Narayanaswami, Ciro Nishiguchi, Remy Notermans, Lucas S. Peng, Albert Ryou, Tsung-Yao Wu, and Michael Yarwood. Assembly and coherent control of a register of nuclear spin qubits. *Nature Communications*, 13(1), May 2022.

[88] M. Saffman and T. G. Walker. Analysis of a quantum logic device based on dipole-dipole interactions of optically trapped rydberg atoms. *Physical Review A*, 72(2):022347, August 2005.

[89] J. T. Wilson, S. Saskin, Y. Meng, S. Ma, R. Dilip, A. P. Burgers, and J. D. Thompson. Trapping alkaline earth rydberg atoms optical tweezer arrays. *Physical Review Letters*, 128(3):033201, January 2022.

[90] T Topcu and A Derevianko. Possibility of triple magic trapping of clock and rydberg states of divalent atoms in optical lattices. *Journal of Physics B: Atomic, Molecular and Optical Physics*, 49(14):144004, June 2016.

[91] D. T. C. Allcock, W. C. Campbell, J. Chiaverini, I. L. Chuang, E. R. Hudson, I. D. Moore, A. Ransford, C. Roman, J. M. Sage, and D. J. Wineland. omg blueprint for trapped ion quantum computing with metastable states. *Applied Physics Letters*, 119(21), November 2021.

[92] Zhubing Jia, William Huie, Lintao Li, Won Kyu Calvin Sun, Xiye Hu, Aakash, Healey Kogan, Abhishek Karve, Jong Yeon Lee, and Jacob P. Covey. An architecture for two-qubit encoding in neutral ytterbium-171 atoms. *npj Quantum Information*, 10(1), November 2024.

[93] Thomas F. Gallagher. *Rydberg Atoms*. Cambridge University Press, September 1994.

[94] Nejira Pintul. *TBD*. PhD thesis, PhD Thesis, Universität Hamburg, 2025.

[95] Soeren Erik Doerscher. *Creation of ytterbium quantum gases with a compact 2D -/3D-MOT setup*. PhD thesis, 2013.

[96] Alexander Thobe. Ultracold yb gases with control over spin and orbital degrees of freedom. *PhD Thesis, Universität Hamburg*, 2014.

[97] Jan Philip Deppe. Charakterisierung eines hochauflösenden Objektivs zur Erzeugung von Anordnungen optischer Mikrofallen, 2022.

[98] Jack Wilson. New tools for quantum science in yb rydberg atom arrays. *PhD thesis*, 2022.

[99] Harry Levine, Alexander Keesling, Ahmed Omran, Hannes Bernien, Sylvain Schwartz, Alexander S. Zibrov, Manuel Endres, Markus Greiner, Vladan Vuletic, and Mikhail D. Lukin. High-fidelity control and entanglement of rydberg-atom qubits. *Physical Review Letters*, 121(12):123603, September 2018.

[100] Tobias Petersen. Charakterisierung eines hochauflösenden Abbildungssystems, 2018.

[101] Min Gu. *Advanced Optical Imaging Theory*. Springer Berlin Heidelberg, 2000.

[102] Eugene Hecht. *Optik*. De Gruyter, April 2018.

[103] Jonas Kasimir Rauchfuß. Generation of arbitrary, homogeneous dipole trap geometries using a spatial light modulator. *Master Thesis, Universität Hamburg*, 2024.

[104] Oscar William Murzewitz. Generating optical tweezers with acousto-optic deflectors for an ytterbium rydberg quantum computer. *Master Thesis, Universität Hamburg*, 2023.

[105] Yukiko Shibasaki, Koji Asami, Riho Aoki, Akemi Hatta, Anna Kuwana, and Haruo Kobayashi. Analysis and design of multi-tone signal generation algorithms for reducing crest factor. In *2020 IEEE 29th Asian Test Symposium (ATS)*, pages 1–6. IEEE, November 2020.

[106] Ivaylo Sashkov Madjarov. Entangling , controlling , and detecting individual strontium atoms in optical tweezer arrays. *PhD Thesis*, 2021.

[107] Koen Cornelis Sponselee. Lattice clock experiments with interacting fermionic quantum gases. *PhD Thesis, Universität Hamburg*, 2021.

[108] Jan Philip Deppe. Implementing a new python-based controlsoftware for cold atom experiments. *Master Thesis, Universität Hamburg*, 2024.

[109] Jun Woo Cho, Han-gyeol Lee, Sangkyung Lee, Jaewook Ahn, Won-Kyu Lee, Dai-Hyuk Yu, Sun Kyung Lee, and Chang Yong Park. Optical repumping of triplet-pstates enhances magneto-optical trapping of ytterbium atoms. *Physical Review A*, 85(3):035401, March 2012.

[110] D. Sesko, T. Walker, C. Monroe, A. Gallagher, and C. Wieman. Collisional losses from a light-force atom trap. *Physical Review Letters*, 63(9):961–964, August 1989.

[111] L. Marcassa, V. Bagnato, Y. Wang, C. Tsao, J. Weiner, O. Dulieu, Y. B. Band, and P. S. Julienne. Collisional loss rate in a magneto-optical trap for sodium atoms: Light-intensity dependence. *Physical Review A*, 47(6):R4563–R4566, June 1993.

[112] Timothy P. Dinneen, Kurt R. Vogel, Ennio Arimondo, John L. Hall, and Alan Gallagher. Cold collisions of sr*-sr in a magneto-optical trap. *Physical Review A*, 59(2):1216–1222, February 1999.

[113] Andre Kochanke. *Towards Quantum Simulationof the Kondo-Lattice-Model*. PhD thesis, 2017.

[114] David Groeters. Diffraction-limited imaging and trapping of ultracold ytterbium atoms in optical tweezer arrays. 2023.

[115] Damien Bloch, Britton Hofer, Sam R. Cohen, Antoine Browaeys, and Igor Ferrier-Barbut. Trapping and imaging single dysprosium atoms in optical tweezer arrays. *Physical Review Letters*, 131(20):203401, November 2023.

[116] Brian J. Lester, Niclas Luick, Adam M. Kaufman, Collin M. Reynolds, and Cindy A. Regal. Rapid production of uniformly filled arrays of neutral atoms. *Physical Review Letters*, 115(7):073003, August 2015.

[117] M. O. Brown, T. Thiele, C. Kiehl, T.-W. Hsu, and C. A. Regal. Gray-molasses optical-tweezer loading: Controlling collisions for scaling atom-array assembly. *Physical Review X*, 9(1):011057, March 2019.

[118] Daichi Okuno, Yuma Nakamura, Toshi Kusano, Yosuke Takasu, Nobuyuki Takei, Hideki Konishi, and Yoshiro Takahashi. High-resolution spectroscopy and single-photon rydberg excitation of reconfigurable ytterbium atom tweezer arrays utilizing a metastable state. *Journal of the Physical Society of Japan*, 91(8), August 2022.

[119] C. Tuchendler, A. M. Lance, A. Browaeys, Y. R. P. Sortais, and P. Grangier. Energy distribution and cooling of a single atom in an optical tweezer. *Physical Review A*, 78(3):033425, September 2008.

[120] Lucas Beguin. Measurement of the van der waals interaction between two rydberg atoms. *PhD thesis*, 2014.

[121] Rudolf Grimm, Matthias Weidemüller, and Yurii B. Ovchinnikov. *Optical Dipole Traps for Neutral Atoms*, pages 95–170. Elsevier, 2000.

[122] Luciano S. Cruz, Milena Sereno, and Flavio C. Cruz. Deep optical trap for cold alkaline-earth atoms. *Optics Express*, 16(5):2909, 2008.

[123] M. E. Gehm, K. M. OHara, T. A. Savard, and J. E. Thomas. Dynamics of noise-induced heating in atom traps. *Physical Review A*, 58(5):3914–3921, November 1998.

[124] Kai-Niklas Schymik, Sara Pancaldi, Florence Nogrette, Daniel Barredo, Julien Paris, Antoine Browaeys, and Thierry Lahaye. Single atoms with 6000-second trapping lifetimes in optical-tweezer arrays at cryogenic temperatures. *Physical Review Applied*, 16(3):034013, September 2021.

[125] Shuo Ma. Quantum computing with neutral yb atom arrays. *PhD thesis*, 2024.

[126] V A Dzuba and A Derevianko. Dynamic polarizabilities and related properties of clock states of the ytterbium atom. *Journal of Physics B: Atomic, Molecular and Optical Physics*, 43(7):074011, March 2010.

[127] Shuzhe Yang, Guido Masella, Vase Moeini, Amar Bellahsene, Chang Li, Tom Bienaimé, and Shannon Whitlock. Compact optical waveform generator with digital feedback, 2024.

[128] Nicolas Heimann, Lukas Broers, Nejira Pintul, Tobias Petersen, Koen Sponselee, Alexander Ilin, Christoph Becker, and Ludwig Mathey. Quantum gate optimization for rydberg architectures in the weak-coupling limit, 2023.

[129] G. Semeghini, H. Levine, A. Keesling, S. Ebadi, T. T. Wang, D. Bluvstein, R. Verresen, H. Pichler, M. Kalinowski, R. Samajdar, A. Omran, S. Sachdev, A. Vishwanath, M. Greiner, V. Vuletić, and M. D. Lukin. Probing topological spin liquids on a programmable quantum simulator. *Science*, 374(6572):1242–1247, December 2021.

[130] Dániel Vörös, Péter Kránitz, and Karlo Penc. Algebraic spin liquid in the su(6) heisenberg model on the kagome lattice. *Physical Review B*, 110(14):144437, October 2024.

Danksagung

An dieser Stelle möchte ich mich bei allen bedanken, die diese Arbeit möglich gemacht haben.
Zu aller erst bei meinem Doktorvater Klaus Sengstock für die Möglichkeit und das Vertrauen meine Doktorarbeit in seiner Forschungsgruppe zu absolvieren.
Bei Christoph Becker möchte ich mich für die viele tägliche Unterstützung bedanken.
Meinen längjährigen PostDocs Alexander Ilin und Koen Sponselee sei für die viele Unterstützung im Labor und die Übernahme zahlreicher Aufgaben gedankt, die gerade nicht mehr auf die To-Do-Liste eines Doktoranden passten.
Mein größter Dank gilt meiner Mitdoktorandin Nejira Pintul. Es war mir stets eine Freude nicht nur unser Experiment mit dir zu Planen, Bauen und zu Betreiben, sondern auch die eine oder andere wohlverdiente Pause mit dir zu verbringen.
Bei Marcel Diem möchte ich mich für die gemeinsame Zeit im Labor bedanken.
Jonas Rauchfuß sei gedankt für seine tatkräftige Hilfe.
In meiner Zeit haben zahlreiche Studenten am Projekt in der ein oder anderen Form erfolgreich mitgewirkt, bei allen möchte ich mich für ihre Beitrag bedanken, namentlich Jan Philip Deppe, Anton Bölian, Henning Mollenhauer, Ben Michaelis, Carina Hansen, Oscar Murzewitz, Philipp Herbig, Frederik Mrozek, Gerrit Gercke, Till Schacht, Ira Schneider und Leonie Aschenbrenner.
Besonders danken möchte ich Jan für die hervoragende Experimentsteuerung ohne die vermutlich kein Datenpunkt in dieser Arbeit wäre und Till für das stets verlässliche und gründiche Paar extra Hände.
Den neuen Doktoranden am Experiment Jonas Rauchfuß und Clara Schellong wünsche ich viel Erfolg mit dem Experiment.
Ortwin Hellmig sei gedankt für jeden wertvollen Trick und jede Spezialanfertigung.
Weiterhin möchte ich mich bei der gesamten Forschungsgruppe für das stets freundliche und hilfsbereite Arbeitsumfeld bedanken.
Ebenso sei dem technischen und administrativen Personal des Instituts gedankt, besonders Ellen Gloy, Anja Cordes, Kirstin Behnke, Loreen Tornier, Reinhardt Mielck und Finn Gloyer.
Besonders bedanken möchte ich mich auch bei Dieter Barlösius für die vielen Stunden beim Entwickeln und Wickeln der Magnetfeldspulen und auch für die Einführung in die Kunst des Glasbläserns.
Der Standortwerkstatt Bahrenfeld sei gedankt für die Anfertigung vieler komplexer Teile für unseren Experimentaufbau, besonders Stephan Fleig, Frank und Natalie Jonas, Gernot Mahler und Phillip Schlottau.
Diese Arbeit wäre niemals gelungen ohne die hervoragende und umfassende Ausbildung, welche ich als HiWi, Bachelor und Master von meinem ersten Team am Lithium-Experiment erhalten habe. Dafür und auch nochmals für die gemeinsame Zeit sei gedankt Christof Weitenberg, Benno Rem, Andreas Kerkman, Michael Hagemann, Mathis Fischer, Justus Brüggenjürgen und Niklas Käming.
Meinen Studienkollegen David Krüger und Bojan Hansen sei ebenso gedankt für die Zeit des

gemeisamen Lernens und Rechnens während des Studiums.
Meiner Familie und meinen Freunden sei für die fortwährende Unterstützung gedankt, nicht nur während meiner Doktorarbeit.
Besonders gedankt sei meinem Vater Birck, weil Du mir schon früh Dein wissenschaftliches und technisches Wissen vermittelt hast und so mein Interesse wecktest, und meiner Mutter Heidi, dafür das ich mich schon immer auf Dich verlassen kann und Du mich egal bei was mit all Deiner Kraft unterstützt.

Eidesstattliche Versicherung

Hiermit versichere ich an Eides statt, die vorliegende Dissertationsschrift selbst verfasst und keine anderen als die angegebenen Hilfsmittel und Quellen benutzt zu haben.
Sofern im Zuge der Erstellung der vorliegenden Dissertationsschrift generative Künstliche Intelligenz (gKI) basierte elektronische Hilfsmittel verwendet wurden, versichere ich, dass meine eigene Leistung im Vordergrund stand und dass eine vollständige Dokumentation aller verwendeten Hilfsmittel gemäß der Guten wissenschaftlichen Praxis vorliegt. Ich trage die Verantwortung für eventuell durch die gKI generierte fehlerhafte oder verzerrte Inhalte, fehlerhafte Referenzen, Verstöße gegen das Datenschutz- und Urheberrecht oder Plagiate.

09.05.2025

Datum

Unterschrift der Doktorandin / des Doktoranden